A DOCTORAL DISSERTATION
PERFORMED IN THE NATIONAL LABORATORY IN FRASCATI, ITALY
AND
IN THE INSTITUTE OF PHYSICS OF THE JAGIELLONIAN UNIVERSITY

SUBMITTED TO THE FACULTY OF PHYSICS, ASTRONOMY
AND APPLIED COMPUTER SCIENCE OF THE JAGIELLONIAN
UNIVERSITY

STUDY OF THE $\phi \to \eta\ e^+e^-$ DALITZ DECAY USING KLOE DETECTOR

Jarosław Zdebik

Thesis advisor:
Prof. Dr hab. Paweł Moskal

Cracow 2013

Wydział Fizyki, Astronomii i Informatyki Stosowanej
Uniwersytet Jagielloński

Oświadczenie

Ja niżej podpisany Jarosław Zdebik (nr indeksu: 206) doktorant Wydziału Fizyki, Astronomii i Informatyki Stosowanej Uniwersytetu Jagiellońskiego oświadczam, że przedłożona przeze mnie rozprawa doktorska pt. „Study of the $\phi \to \eta e^+ e^-$ Dalitz decay using KLOE detector" jest oryginalna i przedstawia wyniki badań wykonanych przeze mnie osobiście, pod kierunkiem prof. dr hab. Pawła Moskala. Pracę napisałem samodzielnie.

Oświadczam, że moja rozprawa doktorska została opracowana zgodnie z Ustawą o prawie autorskim i prawach pokrewnych z dnia 4 lutego 1994 r. (Dziennik Ustaw 1994 nr 24 poz. 83 wraz z późniejszymi zmianami).

Jestem świadomy, że niezgodność niniejszego oświadczenia z prawdą ujawniona w dowolnym czasie, niezależnie od skutków prawnych wynikających z ww. ustawy, może spowodować unieważnienie stopnia nabytego na podstawie tej rozprawy.

Kraków, dnia podpis doktoranta

Moim Najbliższym

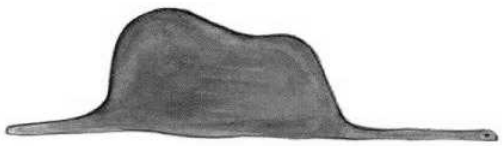

There are thousands of ways to kill time, but no one knows how to resurrect.

Znane są tysiące sposobów zabijania czasu, ale nikt nie wie jak go wskrzesić.

A. Einstein (1879 - 1955)

Abstract

In this thesis the results of the investigation of the $\phi \to \eta e^+e^- \to \pi^+\pi^-\pi^0 e^+e^-$ reaction are presented. The goal of this work is to extract the branching ratio of the $\phi \to \eta e^+e^-$ decay, the slope of an electromagnetic transition form factor of $\phi - \eta$ mesons and a charge radius of the ϕ meson.

For this aim the ϕ mesons were produced in the electron-positron collisions and the η mesons were identified via the $\eta \to \pi^0\pi^+\pi^-$ decay channel. The measurement was performed using the KLOE detector and the electron-positron beams circulated in the DAΦNE accelerator. The detector and accelarator are situated in the Italian National Center for Nuclear Physics in Frascati, near Rome. The DAΦNE collider is running at a center of mass energy of $\sqrt{s} \sim 1020$ MeV in order to produce the ϕ meson almost at rest. The experimental data used in this thesis has been collected in 2004-2005 years.

After selection of the final sample, we reconstructed around $13'000$ events coming from $\phi \to \eta\gamma^* \to \eta e^+e^- \to \pi^0\pi^+\pi^- e^+e^-$ decay with less than 2% background. Thus improving the statistics collected by previous experiments by about two orders of magnitude. The extracted values of form factor slope parameter, $b_{\phi\eta}$, branching ratio, $BR(\phi \to \eta e^+e^-)$ and the radius of ϕ meson for analyzed reaction are: $b_{\phi\eta} = 1.32 \pm 0.23_{stat} \pm 0.02_{syst}$ GeV^{-2}, BR$(\phi \to \eta e^+e^-) = (1.170 \pm 0.035_{stat} \pm 0.008_{syst}) \cdot 10^{-4}$, $< r_\phi^2 >^{1/2} = 0.56 \pm 0.05$ fm, respectively.

The results for slope of transition form factor, branching ratio and the charge radius of ϕ meson are delivered with the biggest precision ever.

Streszczenie

W prezentowanej pracy przedstawione są wyniki badań reakcji $\phi \to \eta e^+e^- \to \pi^+\pi^-\pi^0 e^+e^-$. Głównym celem tej pracy było zmierzenie stosunku rozgałęzień dla rozpadu $\phi \to \eta e^+e^-$, nachylenia czynnika kształtu układu mezonów $\phi - \eta$ oraz promienia rozkładu przestrzennego ładunku mezonu ϕ.

W tym celu mezony ϕ produkowane były w zderzaczu elektronowo-pozytonowym, natomiast mezony η identyfikowane były poprzez rozpad $\eta \to \pi^0\pi^+\pi^-$. Pomiar został wykonany przy użyciu detektora KLOE i wiązek elektronowo-pozytonowych akceleratora DAΦNE. Detektor i akcelerator są położone we Włoskim Narodowym Centrum Fizyki Jądrowej we Frascati, koło Rzymu. Zderzacz DAΦNE, w celu produkcji mezonów ϕ „na progu", pracuje przy energii w centrum masy $\sqrt{s} \sim$ 1020 MeV. Dane eksperymentalne analizowane w tej pracy zostały zebrane w latach 2004-2005.

Po wykonaniu selekcji zdarzeń, w próbce końcowej zrekonstuowano około 13′000 rozpadów $\phi \to \eta\gamma^* \to \eta e^+e^- \to \pi^0\pi^+\pi^- e^+e^-$, zdarzenia tła stanowią mniej niż 2% zawartośći próbki. W rezultacie polepszono statystykę o prawie dwa rzędy wielkości w porównaniu z poprzednimi eksperymentami. Uzyskane wartości nachylenia czynnika kształtu, $b_{\phi\eta}$, stosunku rozgałęzień, $BR(\phi \to \eta e^+e^-)$ i promienia ładunku mezonu ϕ dla analizowanej reakcji wynoszą odpowiednio: $b_{\phi\eta} = 1.32 \pm 0.23_{stat} \pm 0.02_{syst}$ GeV^{-2}, BR$(\phi \to \eta e^+e^-) = (1.170 \pm 0.035_{stat} \pm 0.008_{syst}) \cdot 10^{-4}$, $< r_\phi^2 >^{1/2} = 0.56 \pm 0.05$ fm.

Wyznaczone wyniki nachylenia czynnika kształtu, stosunku rozgałęzień i promienia ładunku mezonu ϕ są najbardziej precyzyjnym pomiarem tych wielkości na świecie.

Contents

1. Introduction

In this work we are investigating the electromagnetic structure of the ϕ and η mesons [1] via the $\phi \to \eta e^+ e^-$ Dalitz decay.

Due to the fact that these mesons are the short-lived particles ($\Gamma_\eta = 1.30 \pm 0.07$ keV and $\Gamma_\phi = 4.26 \pm 0.04$ MeV [1]), with electric charge equal to zero, the investigation of their electromagnetic structure cannot be conducted using the classical methods of scattering. However, the structure of ϕ and η mesons and underlying quark dynamics, in the transition region, can be extracted from e^+e^- invariant mass spectrum for the $\phi \to \eta e^+ e^-$ decay, where the e^+e^- pair originates from the internal conversion of the virtual photon ($\phi \to \eta\gamma^* \to \eta e^+ e^-$). The squared four-momentum transferred by the virtual photon (q^2) corresponds to the squared invariant mass of the created lepton-antilepton pair:

$$q^2 = M^2_{e^+e^-} = (E_{e^+} + E_{e^-})^2 - (\vec{p}_{e^+} + \vec{p}_{e^-})^2.$$

The ratio of q^2 distributions (determined experimentally to calculated assuming a point-like particles) corresponds to the transition form factor of momentum transfer, and the Fourier transform of this form factor to the coordinate space gives the spatial distribution of the transition region [2].

So far the only one measurement with the very limited statistics (74 events) of the slope of transition form factor was performed by the SND collaboration [3] and it is not in good agreement with predictions obtained within the Vector Meson Dominance (VMD) framework [2, 4].

According to the isobar model which describes resonances by the Breit-Wigner formula [5], the form factor in the VMD model takes the following form:

$$F(q^2) = \sum_V \frac{M_V^2}{M_V^2 - q^2 - iM_V\Gamma_V(q^2)}\,, \tag{1.1}$$

where the summation index V runs over the ρ, ω and ϕ vector mesons and the $\Gamma_V(q^2)$ corresponds to the total vector meson width [2, 5–9].

The qualitative behavior of the electromagnetic transition form factor as a function of q^2 is depicted in Fig. 1.1. It should be noted here that study of the electromagnetic transition form factor in $A \to Bl^+l^-$ decays is limited to the time-like region, where the squared four-momentum of the virtual photon, q^2 is greater than $(2M_l)^2$. In this case the mechanism of photon-hadron interaction is especially well pronounced since the squared four-momentum, q^2, approaches the squared mass of the vector meson ($q^2 \approx M_V^2$). The virtual meson reaches its mass shell, i.e. becomes real and then decays to a lepton pair. It results in a strong resonance enhancement of the form factor of a meson. Then, at $q^2 > M_V^2$, the form factor begins to diminish (see Fig. 1.1).

In the framework of the VMD model parametrization of form factor by one-pole approximation is expressed as:

[1] The detailed description of the investigated mesons is given in the Appendix A.

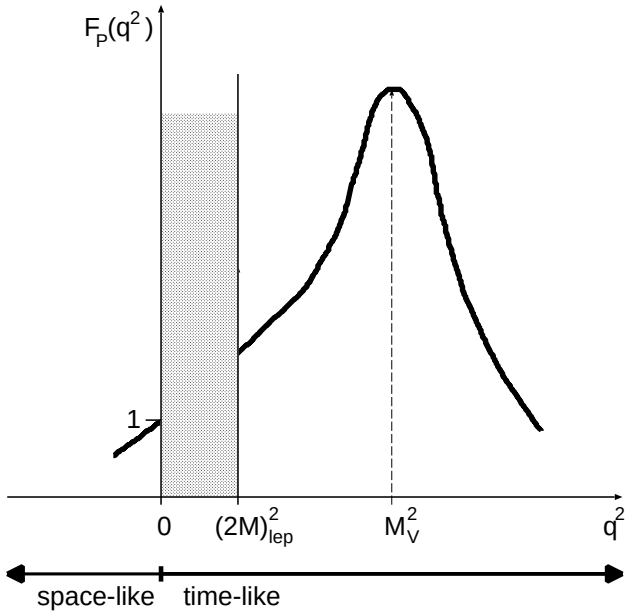

Figure 1.1: The qualitative behavior of the electromagnetic transition form factor as a function of q^2. The shaded area is the region kinematically prohibited (see Eq. 2.4). Picture is adapted from [2].

$$F_{\phi\eta}(q^2) \approx \frac{1}{1 - q^2/\Lambda^2_{\phi\eta}}\,, \tag{1.2}$$

where $q^2 = M^2_{e^+e^-}$ and $\Lambda_{\phi\eta}$ is a free parameter coressponding to the mass of the vector meson ($\Lambda^2_{\phi\eta} = M^2_V$). $M_{e^+e^-}$ is the invariant mass of the electron-positron pair.

The theoretical calculation for $\Lambda_{\phi\eta}$ provides 1.0 GeV (VMD), whereas the value measured by SND is equal to 0.5±0.1 GeV [3].

The precise measured value of the form factor could be useful for verification of predictions of the theoretical models like:

1. Vector Meson Dominance Model (VMD),
2. Quark Model,
3. Leupold-Terschlüsen model [10],
4. Ivashyn model [11].

This work is focused on the measurement of the $\phi \to \eta e^+ e^-$ decay and aims at estimation of branching ratio, slope transition parameter and radius of ϕ meson. The measurement was performed using the KLOE detector and the electron-positron beams circulated in the DAΦNE accelerator which are situated in the Italian National Center for Nuclear Physics in Frascati. The DAΦNE collider is running at a center of mass energy of $\sim$ 1020 MeV corresponding the ϕ meson mass which is produced almost at rest ($\beta \approx 0.0.15$). The main final state channels for a ϕ meson are: K^+K^- (49%), K_SK_L (34%), $\rho\pi$ (15%) and $\eta\gamma$ (1.3%). The channel analysed in this dissertation ($\phi \to \eta e^+ e^-$) constitutes about $1.15 \cdot 10^{-4}$ of all decays of ϕ meson.

The KLOE detection setup consists of two main detectors: an electromagnetic calorimeter and a large drift chamber. The drift chamber and the calorimeter are inside a superconducting coil which produces about 0.52 T magnetic field parallel to the beam axis. The experimental data used in this analysis have been collected in 2004-2005 years.

The four-momentum vector of the η meson was determined using the reconstructed four-momentum vector of the ϕ meson and reconstructed four-momentum vectors of two gamma quanta, two charged pions and e^+e^- pair. The momenta of two gamma quanta were reconstructed using time and energy informations measured by electromagnetic calorimeter. The momenta of charged particles were reconstructed based on the curvature of tracks in the magnetic field, in Drift Chamber. In order to distinguish between pions and electrons, the time-of-flight (TOF) method was used. Finally, the missing and invariant mass techniques were used to identify the η meson.

The additional goal of this work was to understand the signature of the $\phi \to \eta e^+ e^-$ channel in the KLOE detector, since the investiagated reaction is the main and irreducible background for the search of dark matter particles performed at KLOE [12–14].

In the following chapter the theoretical aspects and the results of the previous measurements are presented.

In chapter 3 we describe the DAΦNE collider and the KLOE detector.

Chapter 4 comprises description of experimental conditions and methods of the reconstruction of experimental events.

In chapter 5 the developed simualtion tools dedicated to this analysis are presented.

Chapter 6 presents selection criteria leading to the extraction of the $\phi \to \eta\gamma^* \to \eta e^+ e^- \to \pi^0\pi^+\pi^- e^+ e^-$ signal events.

In chapter 7 the main physics results are presented including the discussion of systematic uncertainties.

Finally, chapter 8 summarises the whole thesis and brings the summary and the outlook.

This thesis is supplemented with appendices. Appendix A presents main properties of ϕ and η mesons and in appendix B the new detectors installed in the KLOE detector are reported.

2. Physics of the Form Factor

The form factor quantity was introduced as a tool for studies of the electromagnetic structure of particles. Such investigations were inaugurated by Hans Geiger and Ernest Marsden in 1909, under the direction of Ernest Rutherford at the Physical Laboratories of the University of Manchester. As a result of „gold foil experiment" for the first time the existence of the atomic nucleus was demonstrated. Since that times the concept of a form factor (FF) plays an important role in such investigations. The FF is defined as a Fourier transform of spatial charge density distribution:

$$F(q^2) = \int \rho(R) e^{iqR} d^3R \,, \tag{2.1}$$

where q denotes a four-momentum transfer, ρ(R) denotes the charge density and R is the radius.

2.1 The $\phi \to \eta e^+ e^-$ Dalitz decay

The existence of the Dalitz decays is a consequence of the presence of radiative decays in the Nature, where a real photon is replaced by a virtual one producing a lepton pair. Such decays in general can be presented as: $V \to P\gamma^* \to Pl^+l^-$, where V is the vector meson, P pseudoscalar meson and γ^* denotes a virtual photon which converts subsequently to lepton and anti-lepton pair (l^+l^-). In our case, the lepton pair consists of electron and positron (e^+e^-). The conversion decays can provide information about the structure of V and P mesons. It can be extracted from the e^+e^- invariant mass spectrum which reflects the meson structure and underlying quark dynamics [2]. The lepton mass spectrum in the $\phi \to \eta e^+ e^-$ Dalitz decay is given by the following formula [2]:

$$\frac{d\Gamma(\phi \to \eta\, e^+e^-)}{dq^2} = \left(\frac{d\Gamma}{dq^2}\right)_{pointlike} \cdot |F_{\phi\eta}(q^2)|^2 =$$

$$= \frac{\alpha}{3\pi q^2}\sqrt{1-\frac{4m_e^2}{q^2}}\left(1+\frac{2m_e^2}{q^2}\right)\cdot\left[\left(1+\frac{q^2}{m_\phi^2-m_\eta^2}\right)^2 - \frac{4m_\phi^2 q^2}{\left(m_\phi^2-m_\eta^2\right)^2}\right]^{\frac{3}{2}} \cdot |F_{\phi\eta}(q^2)|^2 \,, \tag{2.2}$$

where m_ϕ is the ϕ meson mass, m_η is the η meson mass, q denotes the four-momentum transfer and $q^2 = m^2_{e^+e^-}$ denotes the square of invariant mass of the e^+e^- pair.

The first term of equation (2.2) is derived based on the QED calculation for a point-like particle and the second term ($F_{\phi\eta}(q^2)$) stands for the transition form factor which describes effects related with the inner structure of ϕ and η mesons and dynamics of the $\phi \to \eta\gamma^*$ transition.

The kinematic limits for the transition form factor are determined by masses of particles participating in the investigated process. In our case we have $\phi \to \eta e^+ e^-$. So a limit for the mass of virtual photon is equal to:

$$(2m_e)^2 \le q^2 \le (m_\phi - m_\eta)^2 \,. \tag{2.3}$$

In more general form for process $A \to B\gamma^* \to Bl^+l^-$ this formula can be written as:

$$(2m_l)^2 \leq q^2 \leq (m_A - m_B)^2 \,. \tag{2.4}$$

2.2 Predictions of theoretical models

2.2.1 Vector Meson Dominance Model

The seeds of VMD were sown by Nambu [15] in 1957 when he suggested that the charge distribution of the proton and neutron, as determined by electron scattering, could be accounted for by a heavy neutral vector meson contributing to the nucleon form factor. This isospin-zero field is now called the ω.

The VMD model assumes that the hadronic components of the vacuum polarisation of the photon consist exclusively of the known vector mesons. This is certainly an approximation, but in the regions around the vector meson masses, it appears to be a very good one. Hence, the photon is represented by a superposition of neutral vector meson states. It means that it fluctuates between an electromagnetic and a hadronic state. This approach is based on the equivalence of spin, parity and charge conjugation quantum numbers of neutral vector mesons and the photon. Fig. 2.1 shows the coupling of photon and neutral meson [16]. The diagram contains dressed quark propagators and the proper photon-quark vertex.

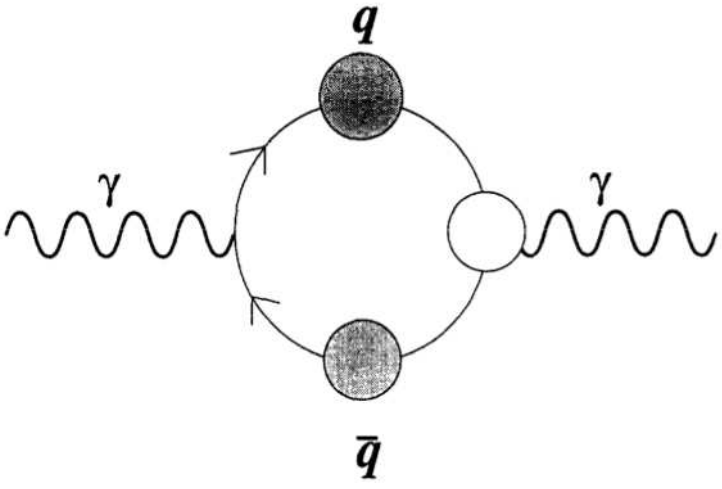

Figure 2.1: One particle irreducible QCD contribution to the photon propagator. The figure is adapted from [16].

Kroll, Lee and Zumino did pursue the idea of reproducing VMD from field theory [16]. Within the simplest VMD model the hadronic contribution to the polarisation of the photon takes the form of a propagating vector meson (Fig. 2.2). This now replaces the QCD contribution to the polarisation process depicted in Fig. 2.1.

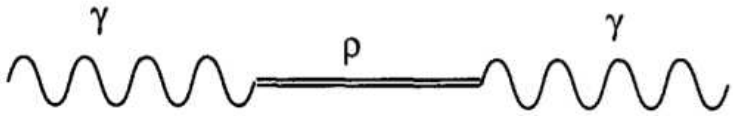

Figure 2.2: A simple VMD-picture representation of the hadronic contribution to the photon propagator. The heavier vector mesons are included in generalised VMD models. The figure is adapted from [16].

According to this model the hadronic electromagnetic current (2.5) is proportional to the vector meson fields $V = \rho, \omega, \phi$ [2]:

$$J_\mu = \sum_{v=\rho,\omega,\phi} \frac{em_v^2}{2g_{v_\gamma}} \cdot v_\mu(x)\,, \tag{2.5}$$

where $g_{v\gamma}$ denotes the coupling constant of vector meson and photon, μ stands for the space-time coordinate, m_v is the mass of proper meson and e is the charge of electron.

Photon interactions with hadrons go through virtual vector mesons. The coefficients $(\frac{em_v^2}{2g_{v_\gamma}})$ determine the strength of the vector meson transitions into photons. In the VMD model, the transition form factors for meson conversion decays ($A \to Bl^+l^-$) are described according to the diagrams shown in Fig. 2.3. In this case the form factors have the form:

$$F_{ab}(q^2) = \frac{\sum_v [g_{abv}/2g_{v_\gamma}] m_v^2 [m_v^2 - q^2 - i\Gamma_v m_v]^{-1}}{\sum_v [g_{abv}/2g_{v_\gamma}]} \simeq \frac{\sum_v [g_{abv}/2g_{v_\gamma}][1 - \frac{q^2}{m_v^2}]^{-1}}{\sum_v [g_{abv}/2g_{v_\gamma}]}\,, \tag{2.6}$$

where for reaction $A \to Bl^+l^-$, A is a vector and B pseudoscalar meson or contrarywise (A pseudoscalar and B vector).

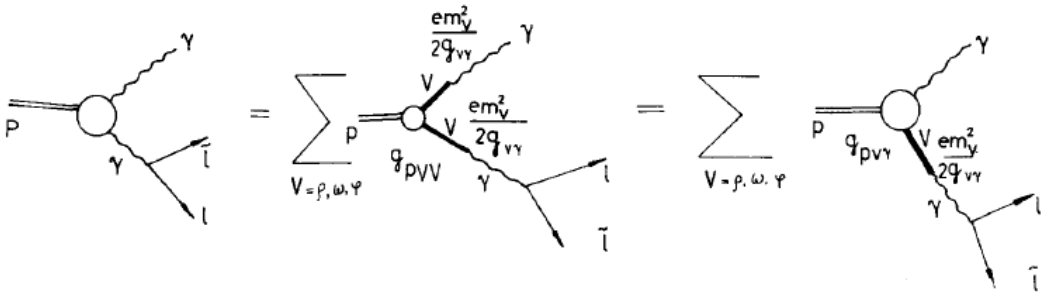

Figure 2.3: Feynman diagrams of transition form factors. The figure is adapted from [2].

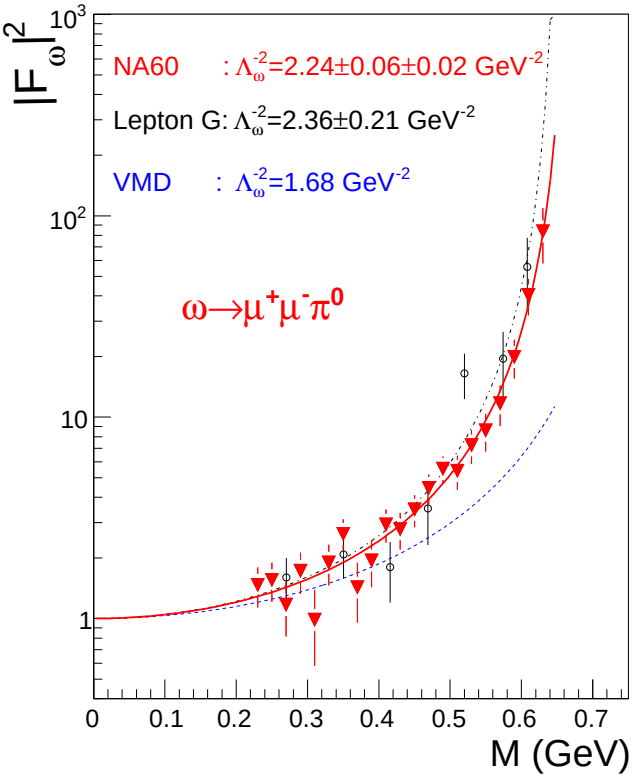

Figure 2.4: Recent experimental data on the ω-meson electromagnetic transition form factor (red triangles) [17], compared to the previous measurement by the Lepton-G experiment (open circles) and to the expectation from VMD (blue dashed line) [17]. The solid red and black dashed-dotted lines are results of fitting the experimental data with the one pole approximation for NA60 and Lepton-G data, respectively.

The standard vector-meson-dominance model (VMD) is very successful in description of the hadronic-electromagnetic reactions but it is not able to describe all of them. One of the example where VMD fails is presented in Fig. 2.4. The $\omega \to \pi^0\gamma^*$ transition form factor calculated based on the VMD is compared to experimental results obtained by the NA60 collaboration [17] and Lepton-G [18] for the decay of the ω meson into $\mu^+\mu^-\pi^0$ final state [17].

The blue dashed line denotes prediction based on the VMD model. The VMD fails to describe the data for this reaction. Therefore there is an ongoing work of finding a better model. Few examples of new approaches are given in next sections.

2.2.2 Leupold-Terschlüsen's model

The Leupold-Terschlüsen's model is based on a new counting scheme, based on the hadrogenesis conjecture, for both the Goldstone bosons and the light vector mesons (details are given in [19,20]). Contrary to the standard counting scheme used in ChPT, the masses of both the Goldstone bosons and the light vector mesons are treated as soft (on equal footing). Thus within the framework of this counting scheme masses up to the mass of the ϕ-meson, $m_\phi \approx 1.02\ GeV$, are soft [21]. If one

describes decays, all involved momenta will be smaller than the mass of the decaying meson and, thus, also of the order of, q, $m_V, m_P, \partial_\mu \sim q$. The restriction to these mesons can be justified by the hadrogenesis conjecture, for which all other low-lying mesons are considered as dynamically generated from interactions of Goldstone bosons and light vector mesons.

In ChPT, the range of applicability, therefore the range for q is limited by the not-considered mesons, in practice by m_V, and (for loops) by the scale $4\pi f$, where f denotes the pion decay constant. In the scheme [19], vector mesons are included and two-particle reducible diagrams (rescattering processes) are resummed.

In Leupold-Terschlüsen's model, the theory determined the leading-order chiral Lagrangian for the decay $V \to P\gamma^*$ by using the counting scheme presented in [19].

The leading-order Lagrangian allows only indirect decays via a virtual vector meson [22]:

$$\begin{aligned}\mathcal{L}_{\text{indir.}} = \quad & -\frac{1}{16f}\, h_A\, \varepsilon^{\mu\nu\alpha\beta}\, \mathrm{tr}\left\{ \left[V_{\mu\nu}, \partial^\tau V_{\tau\alpha}\right]_+ \partial_\beta \Phi \right\} - \frac{1}{16f}\, b_A\, \varepsilon^{\mu\nu\alpha\beta}\, \mathrm{tr}\left\{ \left[V_{\mu\nu}, V_{\alpha,\beta}\right]_+ \left[\Phi, \chi_0\right]_+ \right\} \\ & - \frac{e_V m_V}{4}\, \mathrm{tr}\left\{ V^{\mu\nu} Q \right\} \partial_\mu A_\nu \,, \end{aligned} \tag{2.7}$$

where the photon field is denoted by A_ν. The mass matrix is denoted by $\chi_0 = diag(m_\pi^2, m_\pi^2, 2m_K^2 - m_\pi^2)$ and the quark-charge matrix Q = diag (2/3, -1/3, -1/3). Thereby, the matrix $V_{\mu\nu}$ describes the vector mesons represented by antisymmetric tensor fields,

$$V_{\mu\nu} = \begin{pmatrix} \rho^0_{\mu\nu} + \omega_{\mu\nu} & \sqrt{2}\rho^+_{\mu\nu} & \sqrt{2}K^+_{\mu\nu} \\ \sqrt{2}\rho^-_{\mu\nu} & -\rho^0_{\mu\nu} + \omega_{\mu\nu} & \sqrt{2}K^0_{\mu\nu} \\ \sqrt{2}K^-_{\mu\nu} & \sqrt{2}\bar{K}^0_{\mu\nu} & \sqrt{2}\phi_{\mu\nu} \end{pmatrix}, \tag{2.8}$$

and Φ the Goldstone bosons,

$$\Phi = \begin{pmatrix} \pi^0 + \frac{1}{\sqrt{3}}\eta & \sqrt{2}\pi^+ & \sqrt{2}K^+ \\ \sqrt{2}\pi^- & -\pi^0 + \frac{1}{\sqrt{3}}\eta & \sqrt{2}K^0 \\ \sqrt{2}K^- & \sqrt{2}\bar{K}^0 & -\frac{2}{\sqrt{3}}\eta \end{pmatrix}. \tag{2.9}$$

The first two terms proportional to the parameters h_A and b_A describe the decay of a vector meson into a virtual vector meson and a Goldstone boson and the third term describes the decay of the virtual vector meson into a (real or virtual) photon. The open parameters h_A, b_A and e_A can be fixed by fitting the partial decay widths for the two-body decays $V \to P\gamma$ to the available experimental data. In this model two parameter sets are fixed, parameter set ($P1$) with $e_A = 0$ and $(h_A, b_A) = (2.32, 0.27)$ which describes the leading-order calculation and parameter set ($P2$) with $e_A = 0.015$ and $(h_A, b_A) = (2.10, 0.19)$ which includes the next-to-leading-order term [22]. The next-to-leading-order term is proportional to e_A and so far it is only one next-to-leading-order term calculated in this theory. This term describes a direct vector-pseudoscalar-photon vertex.

The decay of the photon into a dilepton is described by usual QED theory. Fig. 2.5 presents results of calculation of form factor for the decay $\omega \to \pi^0\mu^+\mu^-$ obtained in the framework of the Leupold theory [22]. The solid lines describe the form factors calculated with parameter set (P1), the dotted lines with parameter set (P2) and the dot-dashed lines describe the VMD calculations [22]. The Leupold-Terschlüsen's model is able to describe the NA60 data.

In agreement with isospin conservation and suppression of a decay via a virtual ω meson due to the OZI rule, the decay $\phi \to \eta l^+ l^-$ happens via a virtual ϕ meson in leading order [22–24]. In the

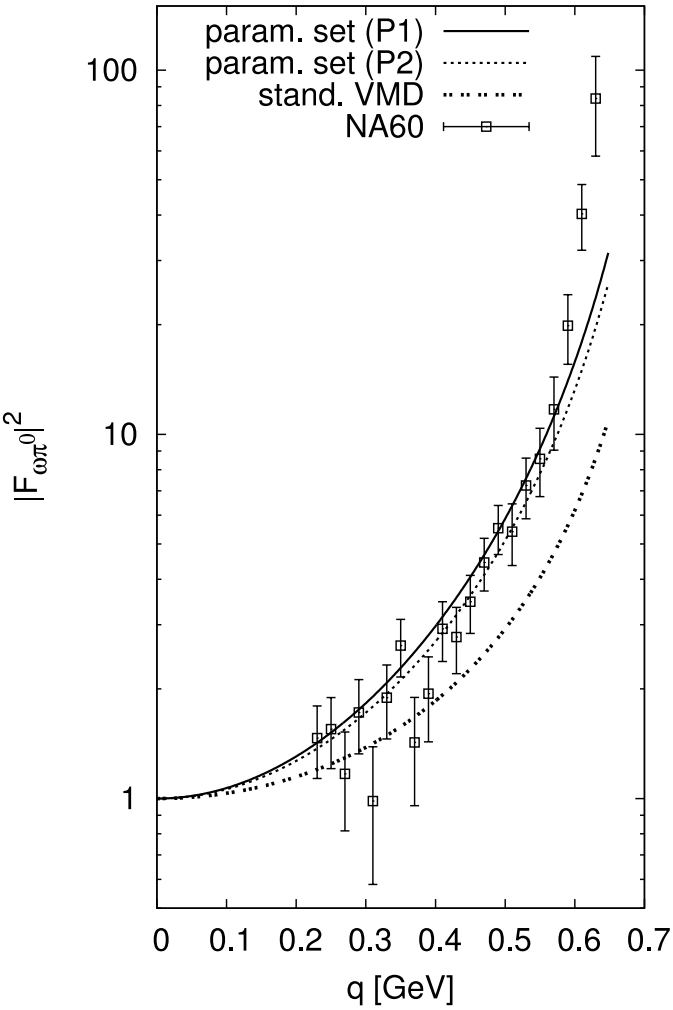

Figure 2.5: Form factor as a function of the four-momentum transfer, for the decay $\omega \to \pi^0\mu^+\mu^-$ calculated with the Leupold-Terschlüsen's theory [22], compared to the experimental data taken by the NA60 collaboration [17].

framework of the discussed model a form factor for the $\phi \to \eta\gamma^*$ transition includes an additional coupling constant term (1 - $g_{\phi\eta}$)[1]:

$$F_{\phi\eta}(q) = g_{\phi\eta}\,\frac{m_\phi^2}{m_\phi^2 - q^2} + (1 - g_{\phi\eta}) \tag{2.10}$$

$$\text{with} \quad g_{\phi\eta} = \frac{2h_A m_\phi^2 - 8b_A\left(2m_K^2 - m_\pi^2\right)}{\left(4\,\frac{e_A}{e_V}\,\frac{m_\phi^2}{m_V^2} + h_A\right)m_\phi^2 - 8b_A\left(2m_K^2 - m_\pi^2\right)} = 2.74 \pm 0.87\,, \tag{2.11}$$

in comparison to the standard VMD form factor:

$$F_{\phi\eta}^{\mathrm{VMD}}(q) = \frac{m_\phi^2}{m_\phi^2 - q^2}\,. \tag{2.12}$$

[1] In order to make sure that the normalised form factor equals 1 at $q^2 = 0$.

Achieved partial decay width in the framework of Leupold-Terschlüsen's model for the decay into a dielectron is in agreement with the experimental data [1, 23, 25]:

$$\Gamma^{Leupold}_{\phi\to\eta e^+e^-} = (4.81 \pm 0.59)\cdot 10^{-7}\,\mathrm{GeV}, \quad (2.13)$$

$$\Gamma^{\mathrm{exp.}}_{\phi\to\eta e^+e^-} = (4.90 \pm 0.47)\cdot 10^{-7}\,\mathrm{GeV}. \quad (2.14)$$

2.2.3 Ivashyn model

This approach [11, 26, 27] is based on the chiral effective field theory with resonances. The energy scale of the applicability of the chiral effective theory with resonances is about 1 GeV due to explicit inclusion of the vector mesons with the order of masses about 1 GeV as the degrees of freedom in the Lagrangian. The momentum-dependent vertices exhibit decoupling in the chiral limit, which allows to fulfil the requirements driven by Chiral Perturbation Theory [27]. In chiral theory with resonances, the strength of vector-vector-pseudoscalar meson transition (VVP) is governed by the effective coupling σ_V which value cannot be theoretically calculated.

This coupling appears in model description of various processes [11, 26] and therefore, it is important to estimate its value from experiment. However, a direct measurement of this coupling is impossible.

In Ivashyn approach the value of σ_V coupling was estimated from fitting the $\omega \to \pi\gamma^*$ form factor, recently delivered by the NA60 from the measurement of the $\omega \to \pi\mu^+\mu^-$. The best $\chi 2$ value is obtained for $\sigma_V \approx 0.58$ [11, 26]. Based on extracted value of σ_V, in the framework of the discussed model the prediction for the $\phi - \eta$ form factor for $\phi \to \eta e^+e^-$ was performed [11, 26].

2.3 Previous experiments

As it was mentioned shortly in the introduction, at present, the only measurement of the $\phi \to \eta e^+e^-$ form factor comes from SND collaboration. The SND (Spherical Neutral Detector) is a general purpose non-magnetic detector situated in Novosibirsk. The main part of the detector is a spherical three layer calorimeter consisting of 1632 NaI(Tl) crystals. The data were collected in 1996 and 1998 by scanning of the energy region around ϕ resonance. The analysis is based on data recorded with the total integrated luminosity of 8.8 pb^{-1}, corresponding to $2.0 \cdot 10^7$ of ϕ meson decays.

The SND experiment was concentrated on the process $\phi \to \eta e^+e^-$, with $\eta \to \gamma\gamma$. The number of selected events which were used to extract the slope of form factor is equal to 74. Additionally, the SND collaboration determined the branching ratio for such process which is equal to $\mathrm{BR}(\phi \to \eta e^+e^-) = (1.19 \pm 0.19 \pm 0.12)\cdot 10^{-4}$. In Fig. 2.6 the final distributions from the SND experiment are shown.

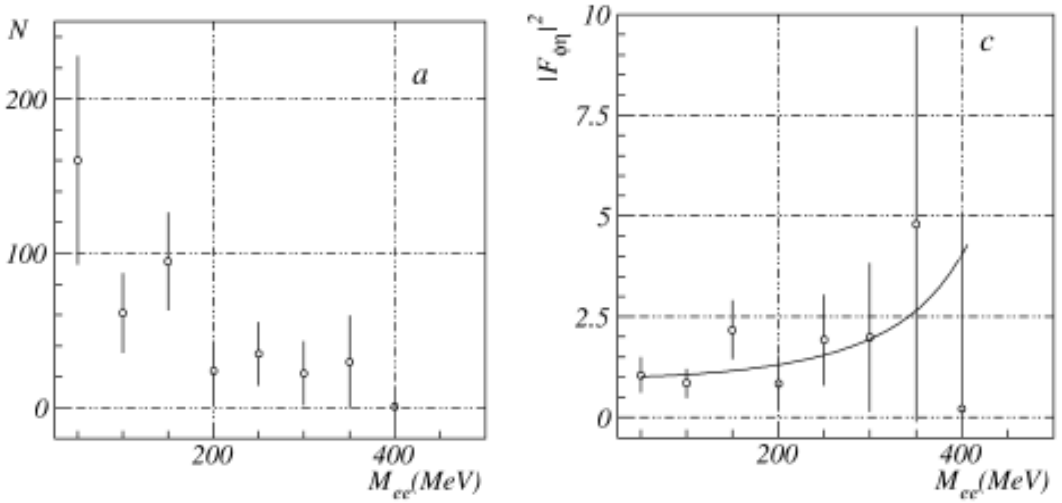

Figure 2.6: The distribution of the e^+e^- pair mass (left part) and transition form factor (right part) for the process $\phi \to \eta\ e^+e^-$ measured by means of the SND detector [3]. Points with error bars denote the experimental data, solid line represents one-pole approximation fit.

The Branching Ratio value for the $\phi \to \eta e^+e^-$ decay was also measured by the CMD-2 (Cryogenic Magnetic Detector) experiment. The CMD-2 detector is installed at the VEPP-2M e^+e^- collider in Novosibirsk. The experiment was performed in a ϕ meson energy range (985-1060 MeV). The data sample which was used during the analysis, corresponds to integrated luminosity of 15.1 pb^{-1}. The missing mass distribution, obtained by CMD-2 experiment, for e^+e^- pair for $\phi \to \eta e^+e^-$ with $\eta \to \pi^0\pi^+\pi^-$ is shown in the Fig. 2.7. The number of reconstructed events in the peak is equal to 53 ± 8.

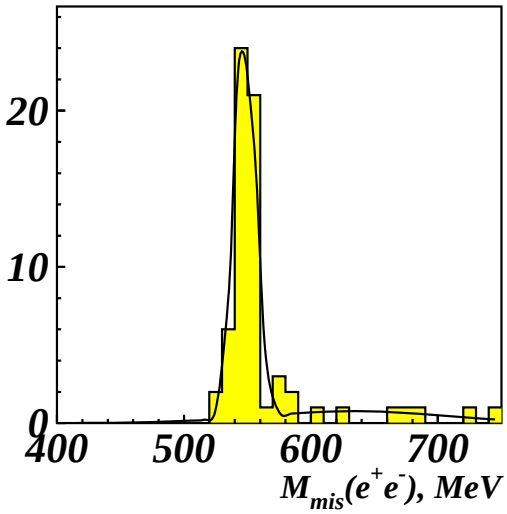

Figure 2.7: Missing mass distribution for $\phi \to \eta e^+e^-$ with $\eta \to \pi^0\pi^+\pi^-$ determined by the CMD-2 experiment. The figure is adapted from [28].

Additionally, the CMD-2 experiment measured the $\phi \to \eta e^+e^-$ modes with $\eta \to 3\pi^0$ and $\eta \to \gamma\gamma$ [28].

Table 2.1 summarizes the results of the data processing for the $\phi \to \eta e^+e^-$ decay observed by the CMD-2 experiment and shows the number of selected events, the expected number of external conversion in the detector material events as well as the obtained branching ratios. The values of BR($\phi \to \eta e^+e^-$) determined from various decay modes of the η meson are consistent within the errors and can be averaged. The averaging procedure, used by CMD-2 experiment in order to deliver the total value, takes into account that some of the sources of the systematic error like e.g. the branching ratios of the intermediate decays are common for three measurements.

Table 2.1: Branching ratio of $\phi \to \eta e^+e^-$ decay measured by CMD-2 experiment [28].

Mode	$N^{exp}_{\phi \to \eta e^+e^-}$	$N^{conv}_{\phi\to\eta\gamma}$	$BR(\phi \to \eta e^+e^-)$, 10^{-4}
$\eta \to \gamma\gamma$	214 ± 20	31 ± 2	$1.13 \pm 0.14 \pm 0.07$
$\eta \to 3\pi^0$	158 ± 13	28 ± 2	$1.21 \pm 0.14 \pm 0.09$
$\eta \to \pi^0\pi^+\pi^-$	53 ± 8	11 ± 1	$1.04 \pm 0.20 \pm 0.08$
Total	425 ± 25	70 ± 3	$1.14 \pm 0.10 \pm 0.06$

2.4 BR and $b_{\phi\eta}$ predictions summary

In Tab. 2.2 the theoretical predictions and previous experimental results for the investigated decay are presented. The table shows Λ, the branching ratio and the form factor slope $b = \frac{dF}{dq^2}|_{q^2=0}$ values.

	Theory			*Experiment*		
	VMD	Leupold	Ivashyn	CMD-2	SND	PDG(2013)
Branching Ratio(10^{-4})	1.1	1.13 ± 0.14	—	1.14±0.16	1.19 ± 0.31	1.15 ± 0.10
$b_{\phi\eta}$ (GeV^{-2})	1.0	2.74 ± 0.87	1.94	—	3.8 ± 1.8	—
$\Lambda_{\phi\eta}$ (GeV)	1.0	—	—	—	0.51 ± 0.12	—

Table 2.2: Decay characteristics.

A more detailed description of the experimental results and the theoretical predictions can be found in the following references [3, 22, 28].

3. KLOE at DAΦNE experimental facility

The KLOE (**KLO**ng **E**xperiment) detector is installed at the interaction point of the electron and positron beams of the DAΦNE (**D**ouble **A**nnular Φ-factory for **N**ice **E**xperiments) collider operating in the Laboratori Nazionali di Frascati (LNF). It has been designed with the primary goal to measure the CP violation parameter R($\frac{\epsilon'}{\epsilon}$) [29, 30]:

$$R = \frac{\Gamma(K_L^0 \to \pi^+\pi^-)/\Gamma(K_L^0 \to \pi^0\pi^0)}{\Gamma(K_S^0 \to \pi^+\pi^-)/\Gamma(K_S^0 \to \pi^0\pi^0)}\,. \tag{3.1}$$

The detector was fully constructed by the end of the year 1998 [31]. The experimental program was completed with integrated luminosity of 2.1 fb^{-1} obtained with the center-of-mass energy equal to the mass of the ϕ meson ($\sqrt{s} \sim M_\phi = 1019.456 \pm 0.020$ MeV [32]).

The cross section for the production of the ϕ vector meson is large and amounts to $\sigma(e^+e^- \to \phi) = 3.1$ μb, this resulted in the production of about $6.5 \cdot 10^9$ ϕ mesons. The ϕ meson decays predominantly into pairs of neutral or charged kaons (see Table A.1), however in about 0.01% it decays also to ηe^+e^- final state.

3.1 DAΦNE collider

The DAΦNE is an e^+e^- collider situated in Frascati, near Rome. The general view of the accelerator complex is presented in Fig. 3.1.

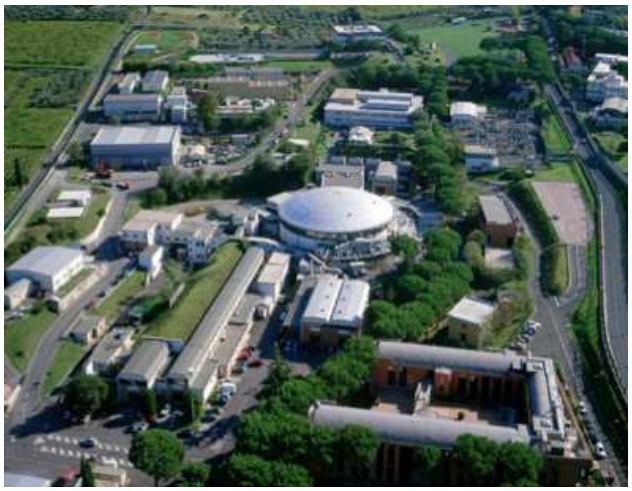

Figure 3.1: View of DAΦNE accelerator complex [33]. In the middle of the photo the ADONE building is seen in which the DAΦNE collider is installed.

The positron and electron beams are injected into a DAΦNE rings at an energy of about 510 MeV and collide at an angle of 25 mrad producing ϕ mesons nearly at rest with a small momentum

of about 13 MeV/c along a x axis (Fig. 3.2).

The DAΦNE collider consists of two intersecting crossing accelerator rings, one for positrons and one for electrons. This layout allows to minimize the perturbation between the electron and the positron beam.

The system of coordinates of DAΦNE collider is presented in Fig. 3.2.

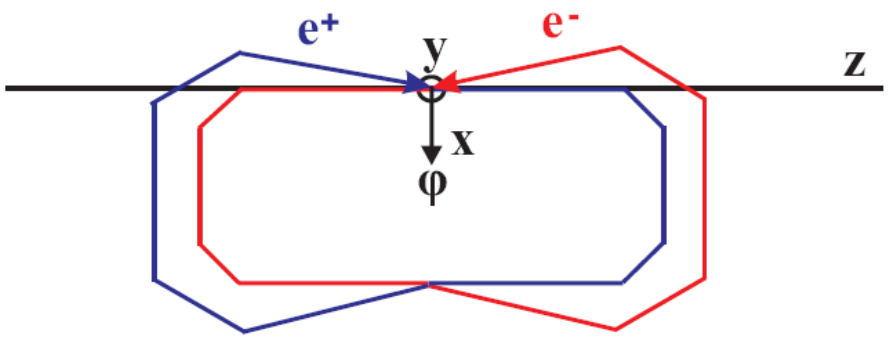

Figure 3.2: The DAΦNE coordinate system.

The main DAΦNE parameters are presented in Table 3.1, and a scheme of the facility is shown in Fig. 3.3.

Parameter	*Value*
Energy [GeV]	0.51
Trajectory length [m]	97.69
RF frequency [MHz]	368.26
Harmonic number	120
Dumping time, τ_E/τ_x [ms]	17.8/36.0
Bunch length at full current e^+/e^- [cm]	2.8/2.2
Beam currents e^+/e^- [A]	2.0/1.4
Bunch length [cm]	1-3
Number of colliding bunches [n]	108
σx $[\mu m]$	700
σy $[\mu m]$	7
σz $[mm]$	25
Emittance, ϵ_x [mm·mrad]	0.34

Table 3.1: The main characteristics of the DAΦNE collider during the 2004-2005 run period [34, 35].

Positrons and electrons are accelerated in the LINAC (**Lin**ear **Ac**celerator) which delivers electron or positron beams in the energy range from 25 to 725 MeV with intensities varying from 10^{10} particle per pulse down to a single-electron [34]. This 60 meters long accelerator is the heart of the DAΦNE injection system. This is an S-band accelerator (2.865 GHz) which delivers 10 ns pulses at a repetition rate of 50 Hz. Electrons, after acceleration to final energy in the LINAC, are

accumulated and cooled in the accumulator and transferred to a single bunch into ring. Positrons require first accelerating of electrons to about 250 MeV to target in the LINAC, where positrons are created. Afterwards the positrons follow the same accelerator elements as electrons [31]. Positrons and electrons after acceleration and accumulation process run around in two storage rings and hit in the collision points. This facility is called a Frascati Φ-factory complex because it produced of about $6.5 \cdot 10^9$ of ϕ mesons during the years from 2000 to 2005. The KLOE experiment is located in one of the two collision points at DAΦNE collider, whereas the second collision point was alternatively occupied by two other experiments: DEAR [36] and FINUDA [37].

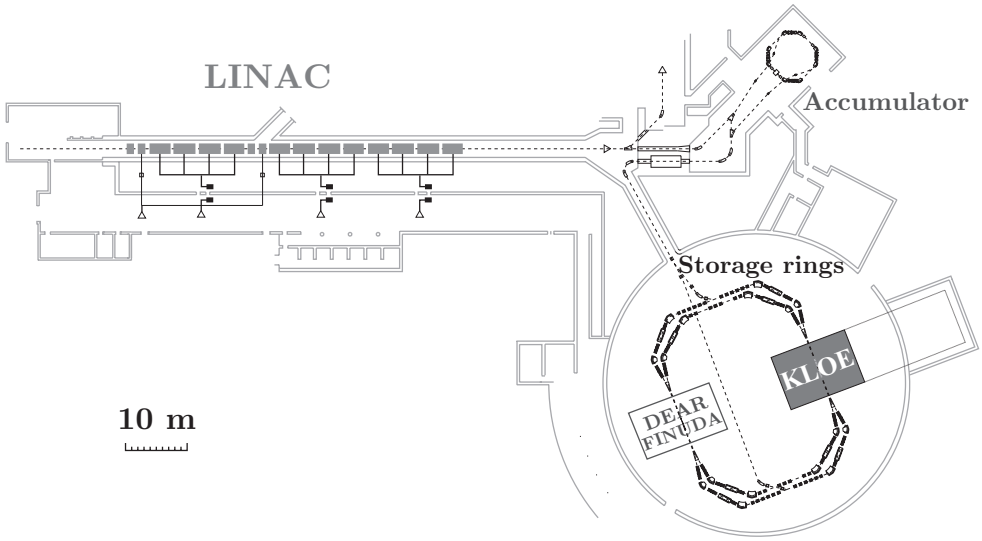

Figure 3.3: Scheme of the DAΦNE collider. The figure is adapted from [31].

At the interaction point (IP) the beam pipe has the shape of a sphere which is made of a beryllium-aluminium alloy with 10 cm diameter and $\sim$ 500 μm thickness [13]. The beryllium, having a low atomic number, has been used to minimize the interaction of particles produced at the interaction point with the beam pipe material [32].

At present a new e^+e^- interaction region was installed [38] in order to increase the collider luminosity by a factor of three [33, 39–42].

3.2 KLOE detector

The KLOE detector (shown schematically in Fig. 3.4) was designed for the study of thr CP violation in the neutral-kaon system. The kaons produced in the ϕ decays travel with approximately one-fifth of the speed of light. The mean path of a K_L meson is about $\lambda_L = \beta\gamma c\tau = 3.4$ m, the size of the apparatus is strongly dependent on this value. This is the reason why the radius of the active part of the KLOE detector is two meters. This size enables to register about 40% decays of neutral long-lived kaons [31]. The detector consists of: an electromagnetic calorimeter (EMC) for the detection of γ quanta, charged pions and K_L mesons [43] and a large drift chamber (DC) for the measurement of the charged particles trajectories [44, 45]. The drift chamber and the calorimeter

are inserted in the magnetic field parallel to the beam axis produced by the superconducting coil [43]. The field value is equal to 0.52 T [32].

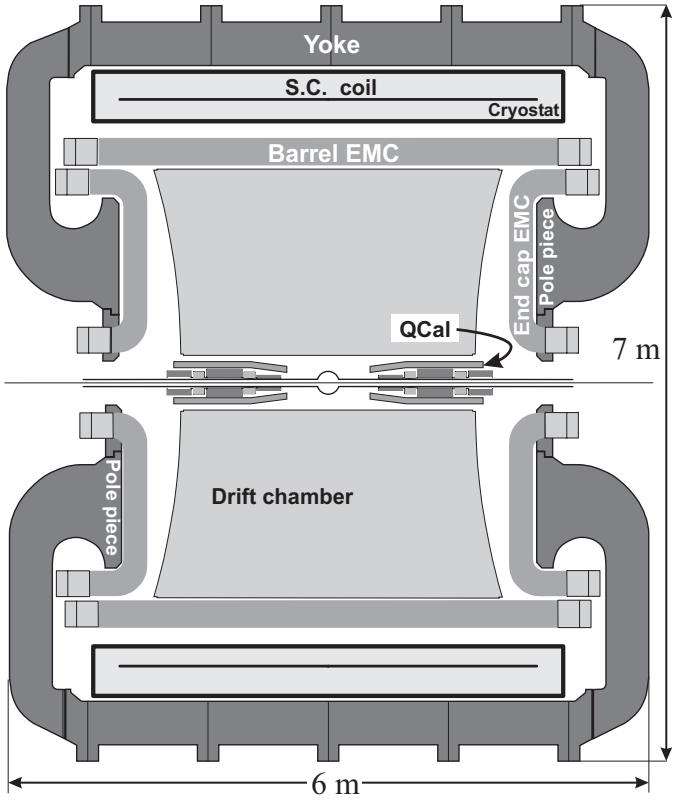

Figure 3.4: Vertical cross section of the KLOE detector. Details are described in the text. The figure is adapted from [31].

In the year 2013 the KLOE detector was upgraded with the new detectors: an inner tracker and a $\gamma\gamma$ tagger, in order to improve its tracking capabilities [39, 46].

3.2.1 Beam Pipe

The beam pipe inside the apparatus is designed in such a way that almost all K_S mesons decay in the vacuum. The sphere of 10 cm radius corresponds to about 17 life times of short-lived kaon which assures that all K_S decays are contained inside [47]. The sphere (Fig. 3.5) made of Be-Al alloy (62% - 38%) is welded on the beam pipe in order to minimize nuclear interactions, photon absorption and kaon regeneration. The beam pipe has also a 50 μm thin layer of cylindrical-shape beryllium with a radius of 4.3 cm. It guarantees electrical continuity to the pipe inside the sphere.

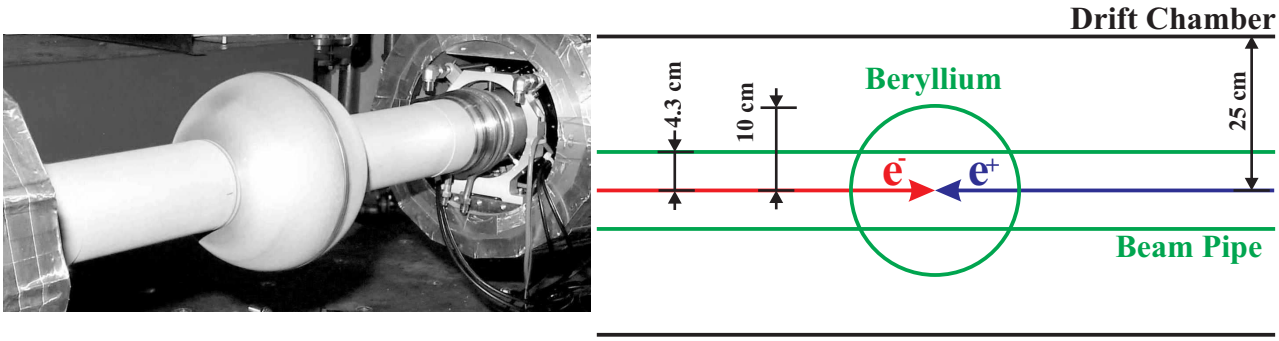

Figure 3.5: Beam pipe at the KLOE interaction region and regeneration surfaces. The realistic view (left panel [31]) and the schematic (right panel).

3.2.2 Drift Chamber

The Drift Chamber (DC) [44] consists of 12582 drift cells (2x2, 3x3 cm^2) arranged in 60 cylindrical layers surrounding the beam pipe. The diameter and length of the DC is equal to 4 m and 3.3 m, respectively [48]. It is filled with 90% helium and 10% isobutane gas mixture, giving a radiation length (gas and wires) equals to 900 m. Charged particles travelling through the drift chamber are ionizing gas medium and then electrons created along the particle trajectory drift to the wires with positive voltage. A multiplication mechanism causes detectable signal at the wire's end [31]. The DC is transparent to γ down to 20 MeV and limits to acceptable levels of the K^0 regeneration and $K^{\pm}$ multiple scattering.

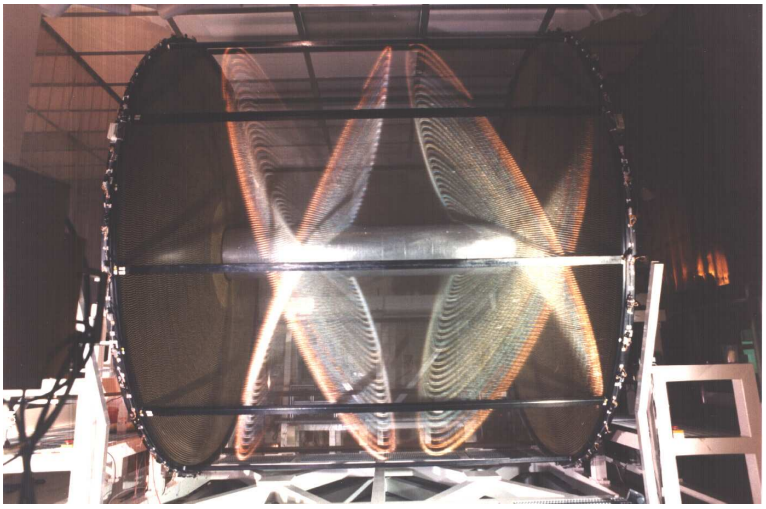

Figure 3.6: The KLOE drift chamber stereo wires geometry. The figure is adapted from [49].

The square of drift cells are arranged in 60 concentric cylinders inclined with alternated stereo angle that progressively increases with the radius. The almost square shape is due to the requirements of three-dimensional track reconstruction and the uniform efficiency throughout the chamber volume. This also implies that the cells are arranged into coaxial layers with alternating stereo angle. The stereo angle of the *k-th* layer, ε, is the angle between the wires and the chamber axis. The discussed angle for the example of one layer is presented in Fig. 3.7 (left). The radial

distance of a wire from the chamber axis changes along z direction, it reaches the maximum (R_p) at the end plates and the minimum (R_0) at the centre of the wire (Fig. 3.7 left). Choosing a constant value for the difference $\delta = R_p - R_0$ implies the most filling of the sensitive volume of the chamber. The *k-th* stereo angle can be written as a function of the δ (Eq. 3.2):

$$tan\ \varepsilon = \pm\frac{2\delta}{L}\sqrt{\frac{2R_0}{\delta} - 1}\,, \tag{3.2}$$

where L is the length of the wire . This allows to fix a value for the δ optimizing the request of a good resolution in the measurement of the z coordinate, since $\sigma_z = \sigma_{r\phi}/tan(\varepsilon)$, and a requirement for a small stereo angle. The δ was chosen to be 1.5 cm, and the stereo angle can range between $\pm$60 mrad and $\pm$150 mrad. The shape of the cells changes slowly along z direction in a periodic way. The wires at radius $R_{p_{k-1}}$ are almost parallel to the wires at R_{p_k} ($\epsilon_k \approx \epsilon_{k-1}$), while the wires at $R_{p_{k+1}}$ have stereo angle $\varepsilon_{k+1} \approx -\varepsilon_k$. The difference between a number of cells in two consecutive layers is constant. Since the track density is higher for small radii, the cells size near the DC inner wall is smaller. The cells area is 2×2 cm^2 in the 12 innermost layers and 3×3 cm^2 in the other 48 layers. Each wire is supported on both sides by a feedthrough inserted in the chamber end plate. The feedthrough hosts a pin which is crimped on the wire. The accuracy of the wire location is ≤ 30 μm [35].

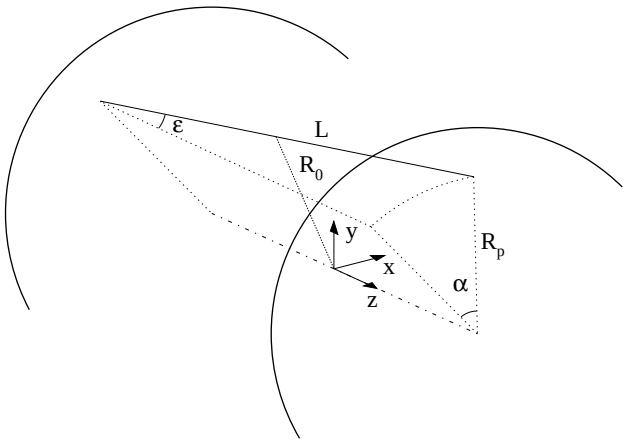

Figure 3.7: Schematic view of KLOE drift chamber wire geometry. The ε is a stereo angle and α the difference in azimuth at the two ends for a wire of the *k-th* layer [50].

The spatial resolution in the azimuthal angle, $\sigma_{r,\phi}$, is about 200 μm. The resolution in the z-coordinate (beam axis) is about 2 mm and resolution of the determination of the decay vertex position amounts to 1 mm. The momentum of the particle is determined from the curvature of its trajectory in the magnetic field with a fractional accurancy $\sigma_p/p \approx 0.4\%$ for the polar angles larger than 45° [50].

The hit identification efficiency is larger than 99%, whereas the efficiency for associating hit to track amounts to about 97% [48].

3.2.3 Electromagnetic Calorimeter

The KLOE electromagnetic calorimeter (EMC) consists of three main parts: a barrel and two endcaps. The barrel (Fig. 3.8) is composed of 24 modules of trapezoid shape and 23 cm thickness, aligned with the beams and surrounding the drift chamber of detector. The endcaps are situated over the magnet pole pieces (see Fig. 3.4), hermetically closing the calorimeter and covering of 98%, of 4π angle [31]. Each of the two endcaps calorimeters consists of 32 vertical modules with length ranging from 0.7 to 3.9 meters. The endcap modules are bent and their cross-section with a plane parallel to the beam axis is rectangular with a thickness of 23 cm [51].

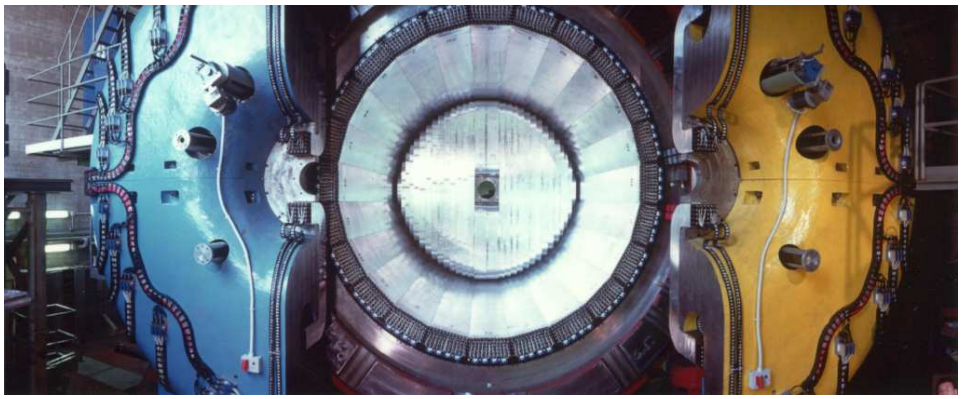

Figure 3.8: Photograph of the KLOE calorimeter. One sees 24 modules of the barrel and the inner plane of the endcap. The figure is adapted from [49].

The KLOE calorimeter module is made of 1,2 mm thickness lead layers (200 layers per 1 module) filled with scintillating fibers of 1 mm diameter (Fig. 3.9).

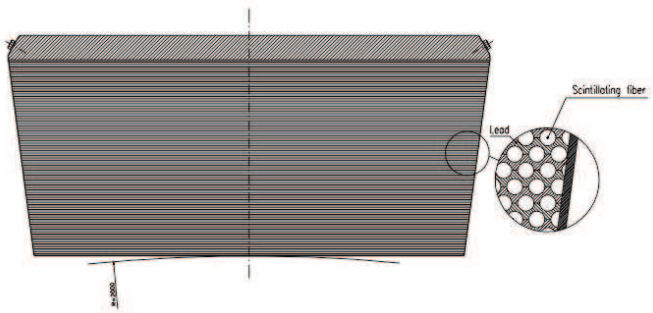

Figure 3.9: Schematic view of the fiber-lead composite of each barrel module of the electromagnetic calorimeter [32].

The volume of the calorimeter consists of 50% of fiber, 40% of lead and 10% of glue. The measured performances for this detector are: full efficiency for γ quanta from 20 to 500 MeV [48], spatial resolution $\sigma(x) \sim 1$ cm, energy resolution $\sigma(E) \sim \frac{5.7\%}{\sqrt{E(GeV)}}$, time resolution $\sigma(t) \sim \frac{57\ \text{ps}}{\sqrt{E(GeV)}} \oplus 140\ ps$ [52]. Analysis of signal amplitude distributions allows to determine the location

where the particle hit the calorimeter module with accuracy of about 1 cm in the transverse plane to the fiber direction. The longitudial coordinate precision is $\sigma(z) \sim \frac{1.2\ cm}{\sqrt{E(GeV)}}$. The mechanical structure of the single trapezoid barrel calorimeter module is shown in Fig. 3.9.

3.2.4 QCAL detector

The KLOE experiment was designed to study the CP violation into the $K\bar{K}$ system through the double ratio $R(\frac{\epsilon'}{\epsilon})$ measurement. The most important background source in these channels is represented by $K_L^0 \to 3\pi^0$ and to reduce it significantly the experiment was provided of a couple of calorimeters surrounding the two DAΦNE quadrupoles close to the IP. These calorimeters (QCAL) have cylindrical shape and they made of layers, of 1.9 mm Pb and 1 mm scintillator tile (BC408). The light signal readout is made by 1 mm fibers (Kuraray Y11-200) optically coupled with the tile in open air. The collected light was sent to the standard photomultipliers. The schematic view of the upper part of the used QCAL detector is presented in Fig. 3.10.

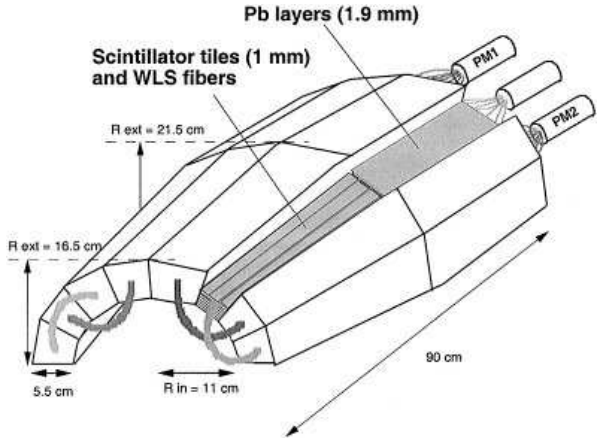

Figure 3.10: Schematic view of the QCAL detector. The figure is adapted from [53].

3.3 DAQ system

The KLOE data acquisition (DAQ) has been designed to sustain a trigger rate of 10^4 Hz, resulting from the combination of ϕ decays, downscaled Bhabha, cosmic rays and DAΦNE collider background. This event rate constraints to acquire event in less than 100 μs on average. In addition to these DAQ tasks, online system has to be able to perform parallel data monitoring and continues detector calibration. The final design of KLOE DAQ has a throughput of 50 Mbyte/s, with average event size of 3.5 KByte. The DAQ readout system involves some of $23'000$ channels of Front End Electronics (FEE) from EMC, DC and the trigger system. For each triggered event, data coming from the whole FEE have to be concentrated in a single CPU for the event building. To perform this concentration a three level scheme has been implemented. At the first level, data from the single FEE crate are readed. The subsequent level combine information from the different crates. The last level, responsible for final event building, subsequent monitor and storage tasks, is implemented via standard TCP/IP connection and works with packets of events in order to optimize the use of network channels [54].

4. Measurement method

4.1 Reconstruction and classification algorithms

The scheme of the offline reconstruction procedure is shown in Fig. 4.1. A raw information in the form of TDC and ADC values of given electronic channels is translated into TDC and ADC values of corresponding detector components, then all EMC information is reconstructed: cell times, positions and energies are put together to build clusters of cells. Clusters are used to give a preliminary estimate of absolute time of the event t_0.

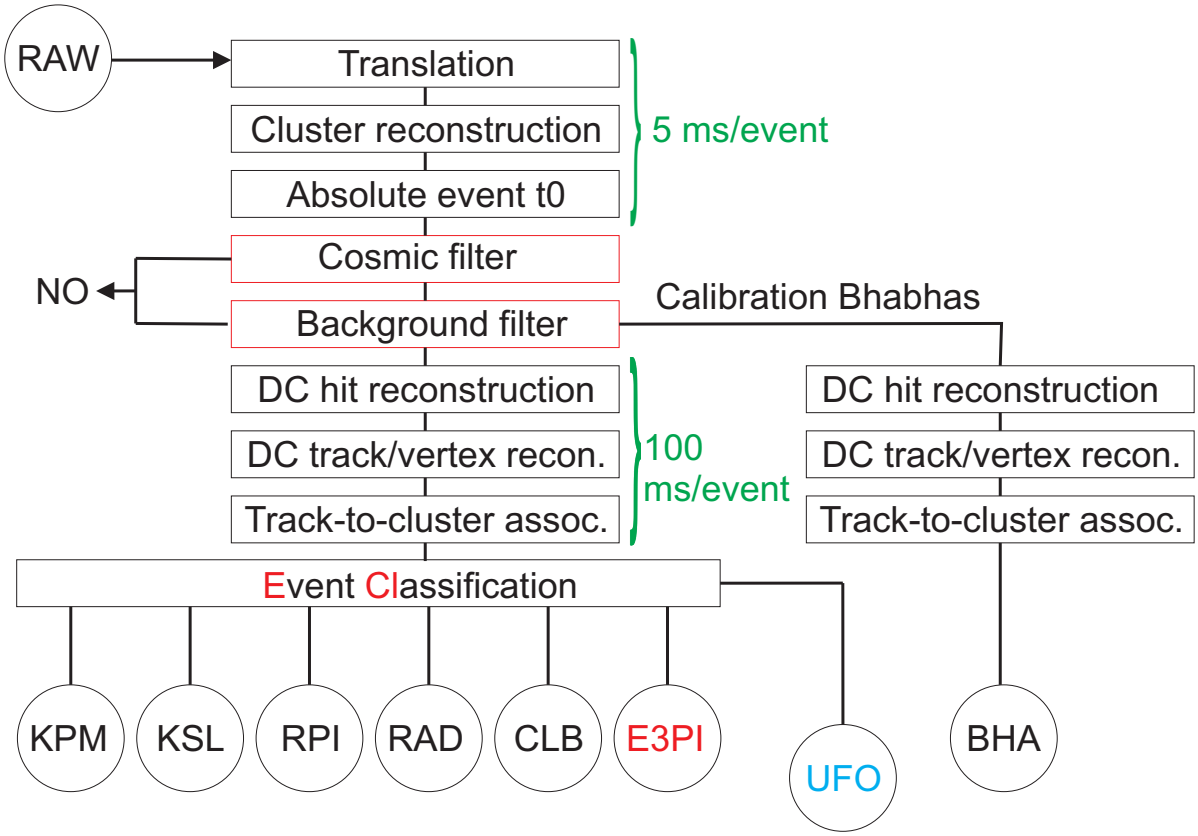

Figure 4.1: Logic scheme of the offline reconstruction. The abbreviations denotes the following decays: $\phi \to K^+K^-$ (**KPM**), $\phi \to K_SK_L$ (**KSL**), $\phi \to \pi^+\pi^-\pi^0$ (**RPI**), $\phi \to P\gamma, S\gamma$ (P, S are a pseudoscalar and a scalar meson) and $e^+e^- \to \pi^+\pi^-\gamma$ decays (**RAD**), Bhabha and cosmic events, with $e^+e^- \to \pi^+\pi^-, \mu^+\mu^-, \gamma\gamma$ (**CLB**), $\phi \to \eta l^+l^-$ with $\eta \to \pi^0\pi^+\pi^-$, implemented for this analysis (**E3PI**), *UnidentiFied Objects*, this stream is filled with events that did not fulfil the requirements related to the previous classes (**UFO**). More detailed description will be presented in next sections.

The clusters information and number of DC hits are used to identify and reject machine

background and cosmic-ray events. For events surviving these rejection filters, the information from DC is extracted. The DC hits times are converted into drift distances. The reconstructed hits positions are then used for track and vertex fitting. After the reconstruction, the events are classified into different categories (streams) by the event classification algorithms (ECL).

4.1.1 Event-builder process

The event-builder process running on the online farm IBM cluster computers (FIBM) writes raw events to the storage area.

For each run, the run number is used to uniquely associate the events with:

- a set of calibration constants,
- values for machine parameters such as energy, beam position,
- quantities related to the detector status such as high-voltage and low-voltage settings, trigger thresholds, drift-chamber gas parameters.

Raw-data files are kept on a local disk until the calibration and the reconstruction are completed, at the end of the reconstruction files are archived on the tape library.

For the drift chamber calibration, two procedures are in use. The first and most commonly used performs a fast analysis to test the validity of the most recent values of the calibration constants. This program runs concurrently with data taking, using cosmic-ray events selected and buffered by the DAQ system. The second procedure performs a complete analysis of the cosmic-ray muon tracks in the DC to update the calibration constants. It is launched only if the existing calibrations fail to describe the detector performance.

For the calorimeter, the calibration procedure is started at the end of each run and lasts about two hours. The procedure uses Bhabha and $\gamma\gamma$ events selected by the DAQ system: the 500 MeV photons are used to set the absolute energy and time scales, while the higher-statistics sample of 500 MeV electrons and positrons allows to the equalization of the energy scale between different calorimeter columns. With an integrated luminosity of 200 nb, the time scale is determined to within 10 ps and the energy scale is accurate at the percent level [55].

4.1.2 Bunch-crossing identification, time t_0

The bunch-crossing time T_{RF} is equal to 2.715 ns. For this reason the trigger is not able to identify the bunch crossing related to each event. The TDC starts as soon as the L1 trigger is phase-locked to a replica of the DAΦNE RF frequency (the clock period is 4×2.715 ns). This allows to obtain the T_{tof}[1] from the T_{TDC} according to the following formula:

$$T_{tof} = T_{TDC} - \delta_C + N_{BC} T_{RF}\,, \tag{4.1}$$

where δ_C is the overall electronic offset and cable delay and N_{BC} is the number of bunch-crossing before the TDC starts[2]. The δ_C and T_{RF} are determined for each data taking run with $e^+e^- \to \gamma\gamma$

[1] T_{tof} is the time of flight of the particle from the event origin to the calorimeter.
[2] $N_{BC}T_{RF}$ is the time needed to generate the TDC start after the $e^+e^- \to \gamma\gamma$ reaction.

events. The distribution of $\Delta_{tof} = T_{clu} - \frac{R_{clu}}{c}$ (Fig. 4.2) reveals well separated peaks: each of them corresponds to a different value of N_{BC}. T_{clu} and R_{clu} denotes the cluster time and position, respectively. The δ_C is defined as the position of the peak with the largest statistics. These values are determined with a precision of ~ 4 ps. A time offset $t_{0,clu} \equiv \delta_C - N_{BC}T_{RF}$ must be subracted from the T_{clu} in order to match this value with the T_{tof}. A value for N_{BC} varies for each event and it can be chosen assuming that the earliest cluster in the event is generated by a prompt photon coming from the interaction point, so that $T_{tof} = \frac{R_{clu}}{c}$ for this cluster. The time offset can be so written as:

$$t_{0,evt} = \delta_C - Int[\frac{Rclu/c - Tclu + \delta_C}{T_{RF}}]T_{RF}\,, \tag{4.2}$$

where the $Int[]$ means the nearest integer to the argument. It is also requested that the energy for this prompt cluster is $E_{clu} > 50$ MeV.

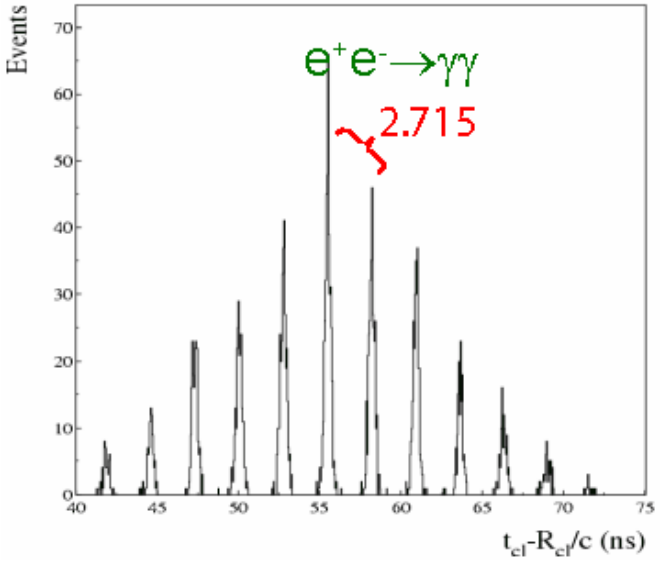

Figure 4.2: Δ_{tof} distribution for 2γ events. The separation of peaks is equal to $T_{RF} = 2.715$ ns [49].

4.1.3 Clusters reconstruction

Each barrel calorimeter module is divided into 60 cells which are arranged in 5 layers and 12 columns (see Fig. 4.3). The barrel calorimeter consists of 1440 cells, each cell is read out on both sides by photomultiplers (referred to as side A and side B in the following). This segmentation provides the determination of the position of energy deposits in the calorimeter.

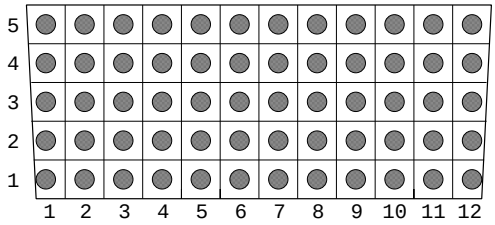

Figure 4.3: Schematic view of the readout cells structure on the one side of the barrel module. Filled circles represent photomultipliers.

For each cell two time signals T^A, T^B (digitized by the Time to Digital Converter (TDC)) and two amplitude signals S^A, S^B (measured by Analog to Digital Converter (ADC)) are recorded.

The arrival time t and the position z of impact point along fiber direction (the zero being taken at the fiber center) is calculated with the aid of times measured at two ends as:

$$t(ns) = \frac{1}{2}(t^A + t^B - t_0^A - t_0^B) - \frac{L}{2v} , \tag{4.3}$$

$$z(cm) = \frac{v}{2}(t^A - t^B - t_0^A + t_0^B) , \tag{4.4}$$

with $t^{A,B} = c^{a,b} \cdot T^{A,B}$, where $c^{A,B}$ are the TDC calibration constants, $t_0^{A,B}$ denotes overall time offsets, L stands for length of the cell and v is the light velocity in fibers.

The energy on one end is calculated according to the formula:

$$E_i^{A,B}(MeV) = \frac{S_i^{A,B} - S_{0,i}^{A,B}}{S_{M,i}} \cdot K , \tag{4.5}$$

where $S_{0,i}$ are the zero-offsets of the amplitude scale, $S_{M,i}$ corresponds to the response for the minimum ionizing particle crossing the calorimeter center and the K factor gives the energy scale in MeV units, and it is obtained from signals of particles with known energy.

For each cell an energy deposit, a position and a time for particles passing through is obtained. These values are used to recognize groups of cells (clusters) belonging to particles entering the calorimeter. For this aim a clustering algorithm is used [43]. Ideally, to each particle the procedure should assign exactly one cluster but in practice it is not always the case. After the recognition of clusters the program reconstructs spatial coordinates and a time of each shower [56]. In particular, the algorithm is based on the following steps. Firstly, for each cell a position and an energy of the shower is reconstructed. Next preclusters are built by connecting the neighboring cells in time and space in order to recreate a full shower [43]. Subsequently, the preclusters are splitted if the spread of the time of the assigned cells is larger than 2.5 ns. On the other hand, cells are merged in one cluster if a distance between them and the center of the precluster is less than 20 cm. After this check the groups of cells are defined as clusters which position and time are computed as energy-weighted averages of the contributing cells. The cell energy formula is expressed as:

$$E_i(MeV) = \frac{E_i^A A_i^A + E_i^B A_i^B}{2} , \tag{4.6}$$

where A,B are correction factors due to the attenuation length along the fiber. Once known the cells energy and times, the cluster energy is obtained as:

$$E_{clu} = \sum_i E_i \,, \tag{4.7}$$

while the cluster position and the cluster time are computed as:

$$\overrightarrow{R}_{clu} = \frac{\sum_i E_i \overrightarrow{R}_i}{\sum_i E_i} \,, \tag{4.8}$$

$$T_{clu} = \frac{\sum_i E_i t_i}{\sum_i E_i} \,, \tag{4.9}$$

with $\overrightarrow{R}_i = (x_i, y_i, z_i)$, where t_i and z_i are calculated according to formulas 4.3 and 4.4, respectively. The z_i is the coordinate along the fiber, x_i and y_i delivering the nominal position of cell.

4.1.4 Tracks reconstruction

Track reconstruction in the chamber consists of three steps: pattern recognition, track fit and vertex fit. The pattern recognition associates hits and reconstructs segments in the *x-y* plane, starting from the outermost layer towards the interaction point. The hits are detected and associated to form a chain. When three hits make a chain, a fourth hit is added if the curvature of the *n-2*, *n-1*, *n* hits and *n-1*, *n*, *n+1* are consistent. To fix the left-right ambiguity, a χ^2 is computed choosing the lowest value. A track requires at least four hits in at least two wire layers. The track is then refitted and the parameters computed on the two sides of the chambers: the tracks are chosen combining the two views according to curvature values and geometrical compatibility. The z coordinate is then added to complete 3D reconstruction. The track fit minimizes the χ^2 function computing the difference between measured distance (expected from space-time relation) and the fit. The procedure is iterative since the cells response depends on track parameters. The track fit adds hits missed by pattern recognition, rejects the ones wrongly assigned to the track and joins the splitted tracks. The vertex fit computes a χ^2 for each track pair. The aim is to reconstruct primary and secondary vertices. In the extrapolation, the particle momentum is corrected for energy loss in the beam pipe and in the drift chamber inner wall, while the multiple scattering is taken into account in the covariance matrix [35].

4.1.5 Track-to-cluster association

To identify photons, one must reject cases in which a charged particle hits the calorimeter producing a cluster. This case is identified by the track-to-cluster algorithm. The track-to-cluster association module establishes correspondences between tracks in the drift chamber and clusters in the calorimeter. The procedure starts by assembling the reconstructed tracks and vertices into decay chains and isolating the tracks at the end of these chains. For each of these tracks, the measured momentum and the position of the last hit in the drift chamber are used to extrapolate the track to the calorimeter. The extrapolation gives the track length L_{ex} from the last hit in the

chamber to the calorimeter surface, and the momentum $\overrightarrow{p_{ex}}$ and position $\overrightarrow{x_{ex}}$ of the particle at the surface. The resulting impact point is then compared with the positions $\overrightarrow{x_{cl}}$ of the reconstructed cluster centroids. A track is associated to a cluster if the distance to the centroid in the plane orthogonal to the direction of incidence of the particle on the calorimeter:

$$Dtcl = |\frac{(\overrightarrow{x}_{cl} - \overrightarrow{x}_{ex}) \times \overrightarrow{p}_{ex}}{|\overrightarrow{p}_{ex}|}|, \tag{4.10}$$

is less than 30 cm. For each track, the associated clusters are ordered by ascending D_{tcl} values.

4.1.6 Offline filter: FILFO

FILFO (FILtro di FOndo, background filter in italian language) was implemented in order to minimise the CPU time necessary for the whole event reconstruction. It takes into account only information on cluster and on DC cells counts. This allows to reject background events before the reconstruction in the drift chamber which is the most CPU-intensive section of reconstruction program. The main FILFO features are the downscaling of Bhabha and cosmic events, and machine background rejection. For the identification of background events, cuts are applied on the number of clusters, the number of DC hits, the total energy in the calorimeter, the average polar angle, position, the depth of the (two) most energetic clusters, the ratio between the number of hits in the innermost DC layers and the total number of DC hits. These cuts have been studied to minimize losses for physics channels. Additionally, a simple cut on anomalously large energy deposits in any calorimeter region is included to reject rare machine background topologies due to sporadic beam-loss events. More detailed description of this filter is available in [57].

The main machine background consists of:

- Coulomb scattering on residual gas,
- bremsstrahlung in the residual gas and in vacuum chamber in the beam pipe wall,
- Touschek effect, i.e. Coulomb scattering between particles in the same bunch.

4.1.7 Events classification: ECL

For events which pass the FILFO selection the classification (ECL) on the basis of information of events topology into different streams is done to be easier use for different physics analyses. The ECL routine identifies the major physics channels at DAΦNE:

- KPM, $\phi \to K^+K^-$ decays,
- KSL, $\phi \to K_SK_L$ decays,
- RPI, $\phi \to \pi^+\pi^-\pi^0$ decays,
- RAD, $\phi \to P\gamma, S\gamma$ (P, S are a pseudoscalar and a scalar meson) and $e^+e^- \to \pi^+\pi^-\gamma$ decays,
- CLB, Bhabha and cosmic events, to be used in calibration purposes, together with $e^+e^- \to \pi^+\pi^-, \mu^+\mu^-, \gamma\gamma$ decays,

- ETA3PITAG (E3PI), $\phi \to \eta l^+ l^-$ with $\eta \to \pi^0\pi^+\pi^-$ events (implemented for this analysis),
- UFO, *UnidentiFied Objects*, this stream is filled with events that did not fulfil the requirements related to the previous classes.

In the analysis described in this thesis the ETA3PITAG algorithm was used, which accepted events fulfilling the following requirements:

- two prompt clusters,
- two positively charged particles from the interaction point (IP),
- two negatively charged particles from IP.

A prompt cluster is defined as an energy deposit in the calorimeter without associated tracks with energy larger than 7 MeV, $|cos(\Theta_{cl})| < 0.92$ and in the expected time window:

$$|T_{cl} - R_{cl}/c| \leq MIN(3\sigma_t, 2ns)\,, \tag{4.11}$$

where σ_t is the calorimeter time resolution parametrized as a function of the cluster energy E_{cl}:

$$\sigma_t(E_{cl}) = \frac{57 \text{ ps}}{\sqrt{E_{cl}(GeV)}} \oplus 140\ ps\,. \tag{4.12}$$

The cuts on 2 ns and on 7 MeV are used to reduce the number of machine background clusters accidentally overlapping with the event. The cut on polar angle selecting the events with:

$$|cos(\Theta_{cl})| \leq 0.92 \longleftrightarrow 23^\circ \leq \Theta_{cl} \leq 157^\circ\,. \tag{4.13}$$

A particle comes from the IP region when the closest approach of trajectory and IP is inside a cylinder with transverse radius $R_{FV} = 4$ cm and half height $Z_{FV} = 10$ cm. For all the possible combinations of the selected clusters and tracks, the invariant mass of two photons and two particles (one positive and one negative) is evaluated assuming that these particles are pions.

If one of the combination is inside a window around the η mass value, 450-650 MeV, the event is selected.

The detail description of KLOE classification procedures could be found in kloe memos [58] and [59]. The preselection steps will be described in detail in a next chapter.

5. Generation of signal events

In this chapter a short description of a new dedicated simulation tools developed for our analysis is given. In order to study the $\phi \to \eta e^+ e^-$ reaction in the KLOE detector a dedicated fast Monte Carlo (MC) simulation program has been evaluated in FORTRAN-90 language. Subsequently, the prepared program has been implemented into GEANT-3 [60] code which comprises also the geometry of the KLOE detector and its realistic material composition. Additionally, the Final State Radiation (FSR) effect based on the PHOTOS package [61], was implemented into the code. The simulation of $\phi \to \eta e^+ e^-$ Dalitz decay was based on the Vector Meson Dominance model. The form factor slope parameter at the beginning of the analysis was taken from the measurement done by SND experiment, which has $\sim 50\%$ error [3], however for the final analysis we changed this value (in Eq. 7.3) to the final one extracted in this work. The performed simulations corresponds to an integrated luminosity ten times larger than the one of the collected data analysed in this work, takes into account changes in the machine operation and background conditions on a run-by-run basis [62]. Corrections for cluster energies and tracking efficiency, evaluated with radiative Bhabha events and $\phi \to \rho\pi$ samples, have been applied [13], respectively.

$M_{e^+e^-}$ distribution

The Monte Carlo (MC) simulation for the signal $\phi \to \eta e^+ e^-$, with $\eta \to \pi^+\pi^-\pi^0$ has been carried out taking into account the $\frac{d\Gamma(\phi \to \eta e^+ e^-)}{dm_{e^+e^-}}$ distribution according to Vector Meson Dominance (VMD) model [2]. The generated shape of the invariant mass distribution of e^+e^- pair is presented in Fig. 5.1.

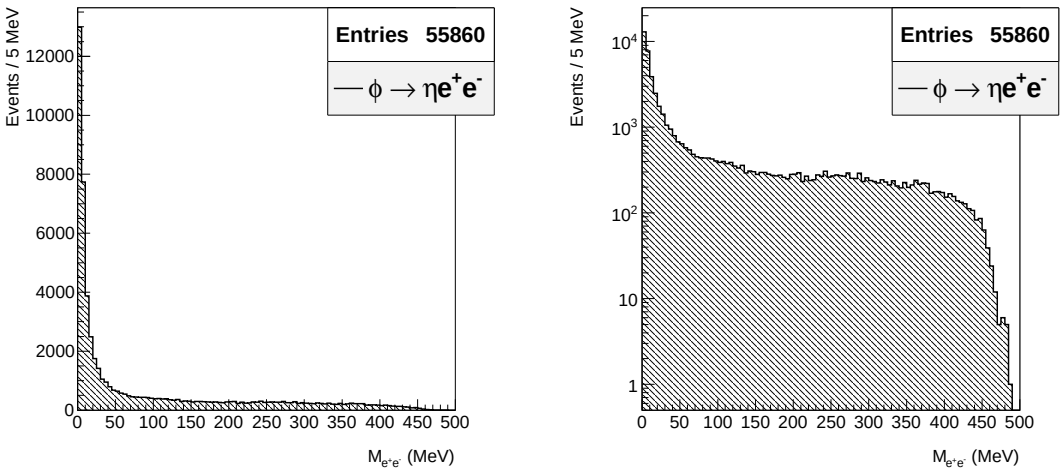

Figure 5.1: Simulated invariant mass of e^+e^- pair for the $\phi \to \eta e^+ e^-$ decay, with $\eta \to \pi^+\pi^-\pi^0$ in linear (left) and logarithmic scale (right). The simulations were performed using the form factor parametrization from the SND experiment [3].

FSR photons

The additional photons can be emitted, in any process that contains coloured or charged objects in the initial or final state. Gluon or photon radiation may change the overall topology of events.

In the investigated reaction two processes could contribute to the final state: Initial State Radiation (ISR), in which the γ quantum is emitted by the incoming electron or positron and Final State Radiation (FSR) where the γ quantum is emitted by one of the two pions or electrons.

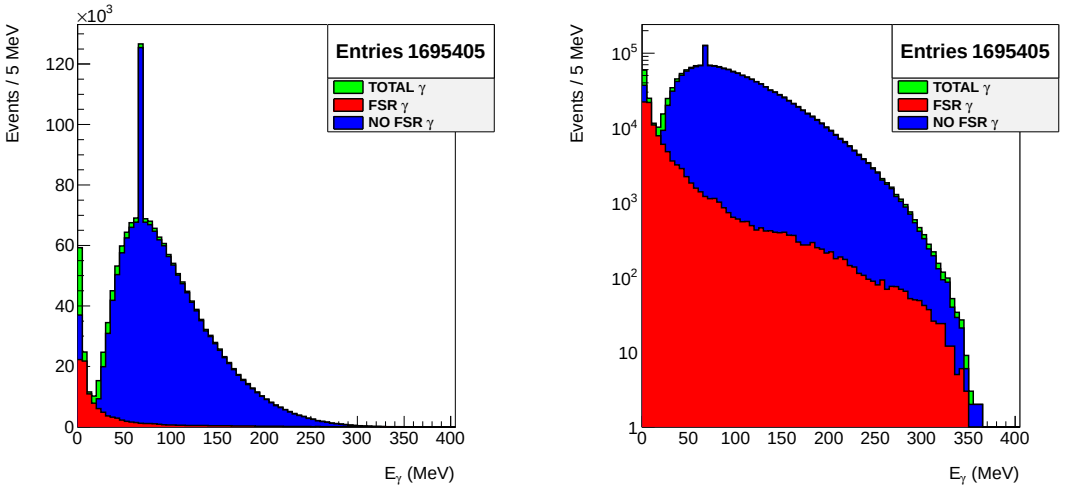

Figure 5.2: Energy of photons for $\phi \to \eta e^+ e^-$ decay, with $\eta \to \pi^+\pi^-\pi^0$. FSR photons were simulated with the package PHOTOS [61]. The results are presented in linear (left) and logarithmic scale (right). The sharp maximum seen at E_γ around 70 MeV corresponds to gamma quanta from π^0 decay.

In the analysed channel, in the final state, we observe six particles ($e^+e^-\pi^+\pi^-\gamma\gamma$) with two γ quanta originating from π^0 meson. However due to existence of the FSR effect an additional photons could be produced changing the total number of particles in the final state.

A QED radiative corrections were simulated for signal using the PHOTOS package. It is a universal Monte Carlo algorithm that simulates the effects of QED radiative corrections in decays of particles and resonances. The first version of this algorithm was released in 1991 [63].

Main purpose of the implementation of the FSR effect into the simulation program was checking its influence on the efficiency of signal preselection due to different signal topology in the final state where we can observe events with additional one or two photons. This test was interesting to perform since at a preselection level we select events with exactly two neutral clusters, two charged positive and two charged negative tracks registered in DC, in the final state.

The simulations show that about 42% of FSR photons have energy less than 10 MeV and the fraction of photons, produced via FSR effect in investigated reaction, is less than 3% of total signal events. This shows that this effect is negligible for the investigated reaction.

6. Selection of events corresponding to the $\phi \to \eta e^+ e^-$ decay

The $\phi \to \eta e^+ e^-$ decay, with the final topology $\phi \to \pi^+\pi^-\gamma\gamma e^+ e^-$, was measured by the KLOE detector during a long data taking period in the years 2000-2005. The main experimental data sample, which is investigated in this thesis, obtained in years 2004-2005, corresponds to the luminosity of 1.52 fb^{-1}. It was collected by colliding of the e^+ and e^- at the energy corresponding to the ϕ meson mass. Altogether about $5 \cdot 10^9$ ϕ mesons were produced giving possiblility to reconstruct around 13000 events of the $\phi \to \eta e^+ e^-$ channel.

6.1 Trigger logic

The main goal of the KLOE trigger system is to:

- record a signal of production of the ϕ meson,
- recognize Bhabha and cosmic-ray events and accept a downscaled sample for calibration purposes,
- reject a machine background.

There are two main sources of background which have to be suppressed at the trigger level. One is due to Bhabha events at small angles, where electrons and positrons hit the low-β quadrupoles and produce showers inside the detector. The other source is due to particle losses from the DAΦNE beams. These off-momentum particles come from beam-gas interactions or Touschek scattering.

The trigger is based on a local energy deposit in the calorimeter and a multiplicity information from the drift chamber. In order to produce an early trigger with a good timing to start the acquisition operations and to use as much information as possible from the drift chamber, the trigger logic is divided into two levels (Fig. 6.1). Specifically, after the arrival of a first level trigger, an additional information is collected from the drift chamber, which is used, together with the calorimetric information, to confirm the former and to start the data acquisition system. For the trigger purposes the fine granularity of the calorimeter is not needed, therefore the signal coming from the 4880 photo-multipliers is summed, shaped and discriminated in order to define 240 trigger sectors. This concentration is a compromise between the goal of minimizing the number of the trigger signal and the desire of triggering on single particles. The calorimeter barrel drives three groups of 48 trigger channels named *normal*, *overlap* and *cosmic* series. Each barrel trigger sector in the *normal* and *overlap* series is made of 5 cells $\times$ 6 columns (as indicated in Fig. 6.2). The cosmic series are used for the cosmic flag and consist only of the cells of the fifth plane of the calorimeter. In total there are 48 $\times$ 3 sectors. The calorimeter triggers on local energy deposits larger than a programmable threshold. Two thresholds are given for each EMC signal, the first at low energy (LET) $\sim$ 50 MeV in order to trigger on low energy particles from ϕ decays and the second at high energy $\sim$ 350 MeV in order to identify Bhabha events. The drift chamber trigger is based on the multiplicity of fired wires.

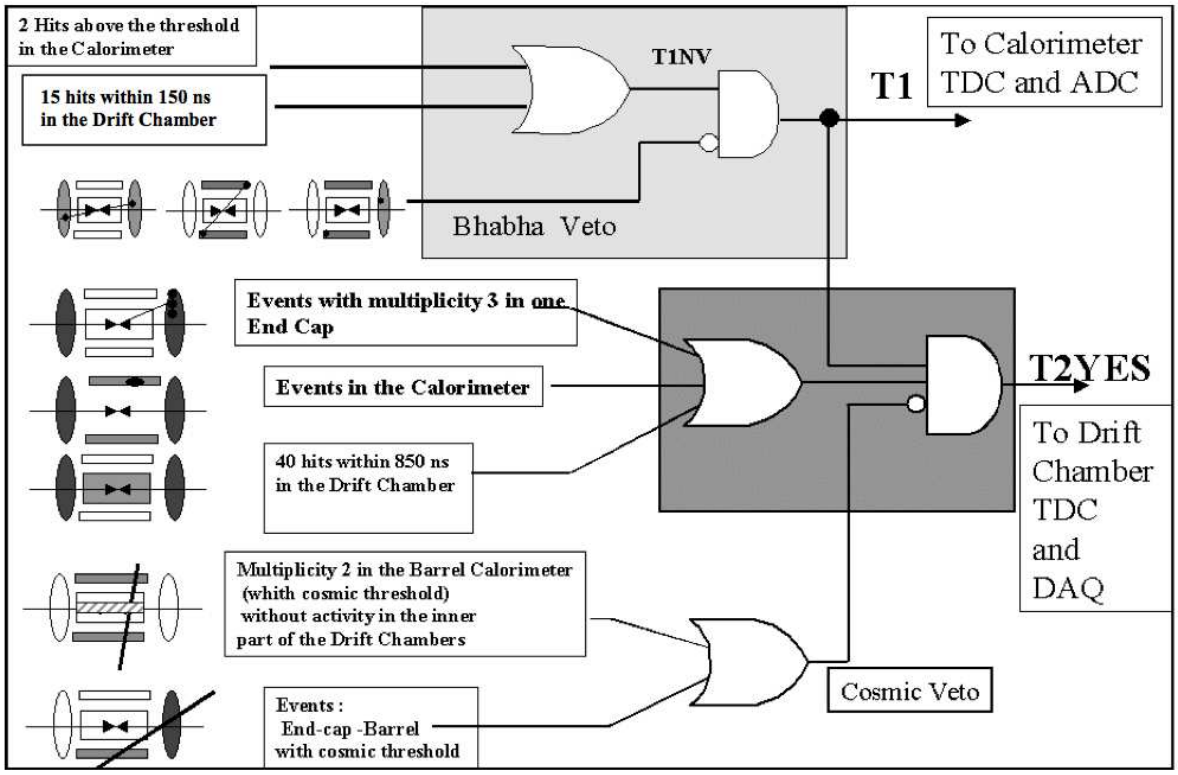

Figure 6.1: Schematic view of the KLOE trigger logic [64]. T1 and T2 denote the trigger level one and two, respectively.

The level one trigger (T1) sets a $\sim$ 2 μs long acknowledge signal, which vetoes other first level triggers and allows signals formation from the drift chamber cells. Before being distributed, the first level trigger is synchronized with a resolution of 50 ps with the DAΦNE radiofrequency divided by 4 (T = 10.8 ns). Therefore, the calorimeter TDCs measure the time with respect to a bunch crossing coming N_{BC} periods after the collision that originated the event, where N_{BC} has to be determined by the offline reconstruction of the event. This technique allows to preserve the resolution on time measurement at the level of picosecond, which would be otherwise spoiled by the intrinsic jitter of the trigger signal formation. At the end of the dead time the trigger system asks for a confirmation of the level one decision and makes veto for cosmic-rays using energy deposit localized in the outermost calorimeter plane. The cosmic flag requires two energy release above the threshold (30 MeV) on the outermost plane of the calorimeter in the Barrel-Barrel or Barrel-Endcap configuration. With this choice of threshold the trigger rate on cosmic rays decreases from 2.6 KHz without flag, to 0.68 KHz, thus giving an efficiency in cosmic ray events identification of $\sim$80%.

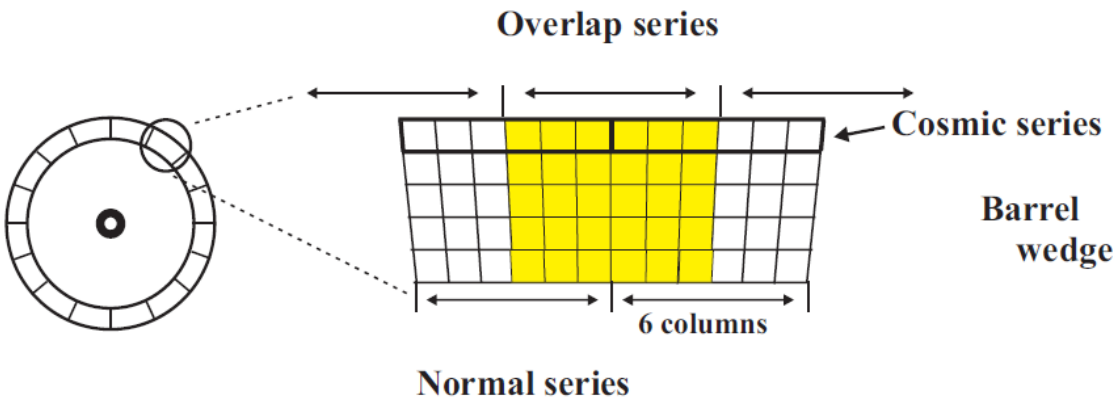

Figure 6.2: Trigger sectors in the barrel. Details are given in the text.

The signal from these dedicated channels are treated in the same way as those used to define the ϕ or Bhabha calorimetric triggers but with a threshold chosen to be equal to the average energy released in a cell by a minimum ionizing particle (MIP) (40-50 MeV). Once two sectors are above the threshold, the cosmic rays bit is activated and the event flagged. To avoid rejection of $\mu^+\mu^-$ events, which trigger easily the external planes of the calorimeter, a third level trigger (T3) has been developed to recover those events. The T3 filter performs a fast preliminary pattern recognition looking for tracks coming from the interaction point. If no track is coming from the IP the event is rejected. The level two trigger T2 gives the stop to chamber TDCs and starts the data acquisition exactly 2 μs after the T1. The second level trigger algorithm can be summarized in this way (Fig. 6.1):

- ϕ trigger: (at least 2 calorimeter hits in the barrel or 3 hits in the same endcap) OR (40 drift chamber hits integrated during 850 ns after T1).

- Cosmic flag: 2 hits on the external plane of the calorimeter with barrel-barrel or barrel-endcap topology.

6.2 Identification of the $\phi \to \eta e^+e^- \to \pi^+\pi^-\pi^0 e^+e^- \to \pi^+\pi^-\gamma\gamma e^+e^-$ decay

The analysis of the $\phi \to \eta\ e^+e^-$ decay with subsequent, $\eta \to \pi^+\pi^-\pi^0$, has been performed using 1.52 fb^{-1} of the KLOE data set. The first preselection of simulated events and experimental data is done with the ETA3PITAG algorithm described in section 4.1.7. Next, as the first step of the analysis the rejection of split tracks is performed [65]. Events with exactly four tracks corresponding to two positive and two negative particles and two photon candidates are then used in the further analysis. Pion tracks are identified by assuming that the particles are pions and calculating the invariant mass of the $\pi^+\pi^-\gamma\gamma$ system. The pions are assigned to these tracks for which the calculated invariant mass is closest to the mass of the η meson.

The first step of the analysis was the preselection of events, that have to satisfy the following criteria:

1. two „positive" and two „negative" tracks with a point of closest approach to the beam line being inside a cylinder around the interaction point (IP), with a transverse radius R=4 cm and a length Z=20 cm,

2. two energy clusters in calorimeter with $E > 7$ MeV not associated to any track, in an angular acceptance $|\cos\theta_\gamma| < 0.92$ and in the expected time window for a photon ($|T_\gamma - R_\gamma/c| <$ MIN$(3\sigma_t, 2\,\text{ns})$), cut described in 4.1.7 section,

3. loose cuts on $\pi^+\pi^-\gamma\gamma$ and $\gamma\gamma$ invariant masses ($495 < M_{inv}(\pi^+\pi^-\gamma\gamma) < 600$ MeV, $70 < M_{inv}(\gamma\gamma) < 200$ MeV).

The distribution of invariant mass of two γ quanta is presented in Fig. 6.3. A clear signal from the $\pi^0 \to \gamma\gamma$ decay is visible. For further analysis events with $70 < M_{inv}(\gamma\gamma) < 200$ MeV are accepted as indicated by the red vertical lines. After the preselection, a clear peak corresponding to $\phi \to \eta\, e^+e^-$ events is observed in the distribution of the recoil mass of the e^+e^- pair (Fig. 6.4) at the mass value equals to the mass of the η meson. The second peak at ~ 590 MeV is due to $\phi \to K_S K_L$, $K_S \to \pi^+\pi^-$ events with a wrong mass assignment. Events in the $535 < M_{\text{recoil}}(e^+e^-) < 560$ MeV window are retained for further analysis.

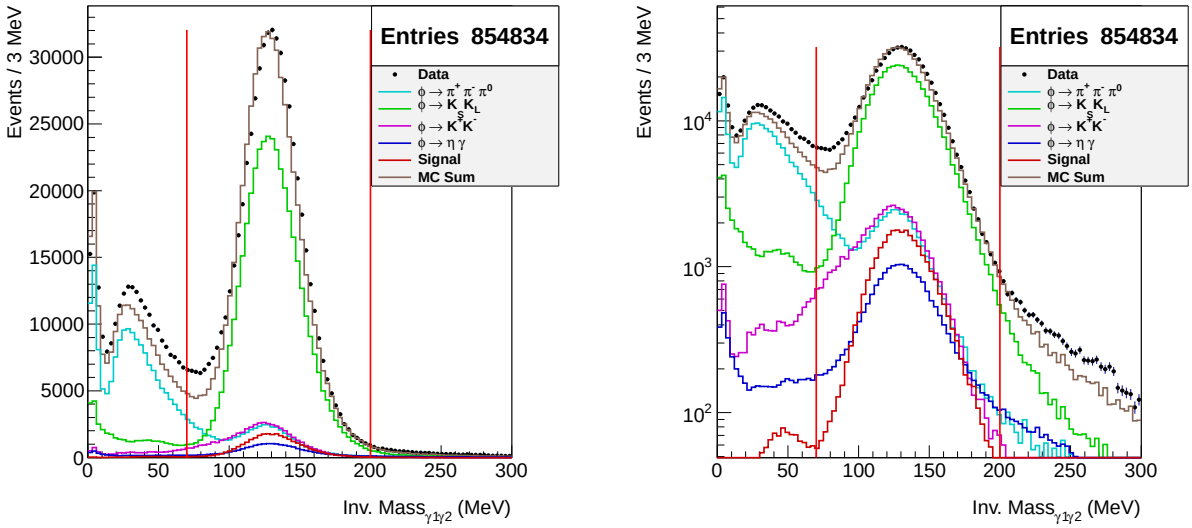

Figure 6.3: Invariant mass of two photons presented in linear (left) and logarithmic scale (right). The vertical red lines denote the performed cut. Events in range 70-200 MeV are accepted. The points denote experimental data and coloured histograms correspond to results of simulations of the decays as indicated in the legend. The results of simulations are normalized in amplitude to the experimental luminosity (1.52 fb^{-1}).

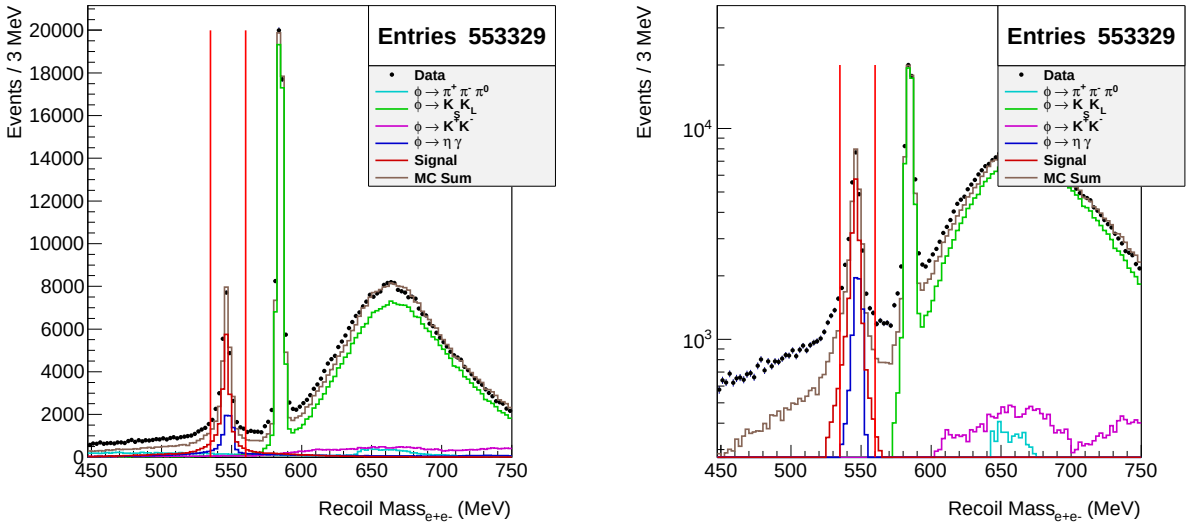

Figure 6.4: Recoiling mass against the e^+e^- pair after preselection. Presented in linear scale (left) and logarithmic scale (right). The points denote experimental data and coloured histograms correspond to the results of simulations of the decays as indicated in the legend. The results of simulations are normalized in amplitude to the experimental luminosity (1.52 fb^{-1}).

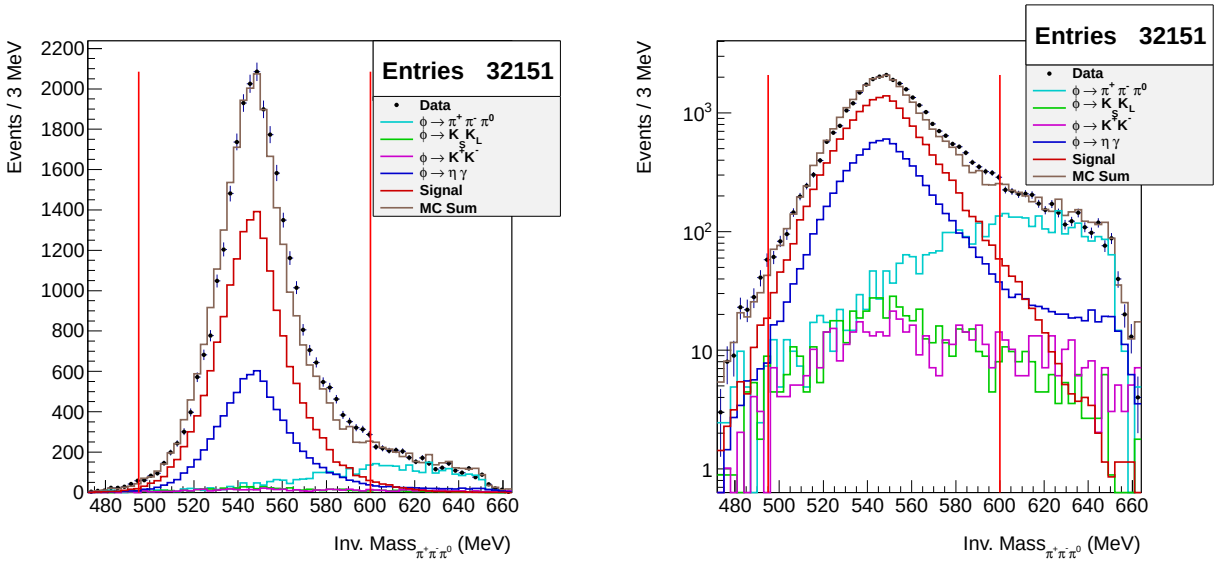

Figure 6.5: Invariant mass of three pions presented in linear (left) and logarithmic scale (right). The red lines denote the performed cut, the events in range 495-600 MeV are accepted. The points denote experimental data and coloured histograms correspond to results of simulations of the decays as indicated in the legend. The results of simulations were normalized in amplitude to the experimental luminosity (1.52 fb^{-1}).

The additional cut on invariant mass of $\pi^+\pi^-\pi^0$ was performed (Fig. 6.5) in order to suppress the background due to the direct pions production in reaction $\phi \to \pi^+\pi^-\pi^0$ and to select pions originating from the η meson decay. After the preselection, the remaining background comes mainly from the $\phi \to \eta\gamma$ reaction and events with more than two charged pions in the final state. The $\phi \to \eta\gamma$ decay may lead to the same final state as $\phi \to \eta e^+e^-$ decay due to conversion of real photon on a detector material ($\gamma \to e^+e^-$). This conversion appears on the beam pipe (BP) or on Drift Chamber Wall (DCW). The schematic view of a conversion of γ quantum on a beam pipe is shown in Fig. 6.6.

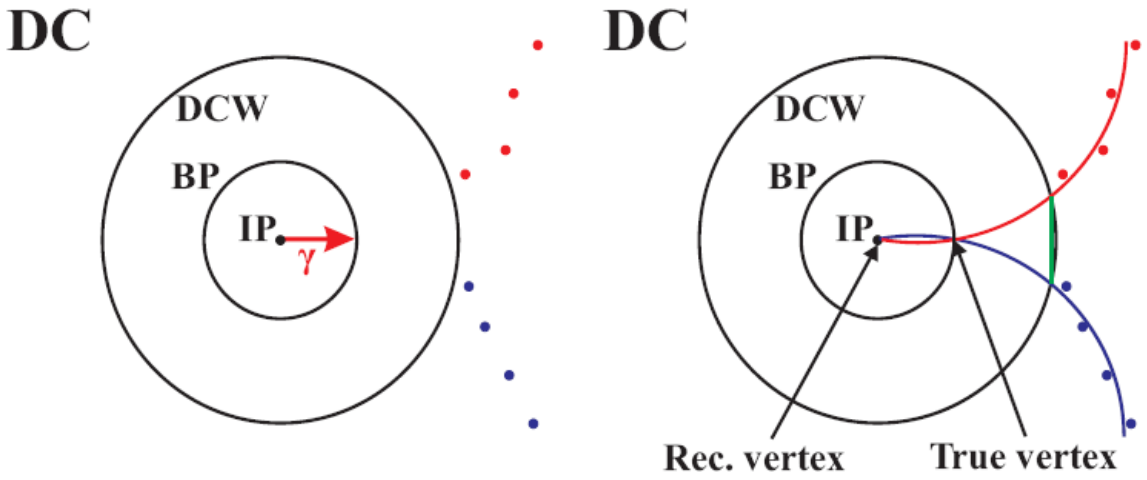

Figure 6.6: Schematic view of the conversion process of γ quantum in the x-y plane of KLOE detector. The photon from background process $\phi \to \eta\gamma$ converts on the BP surface. The two tracks can imitate the signal final state topology (right panel). The dots represent hits in the DC.

This background fakes a signal topology because the KLOE reconstruction algorithms can find a vertex of two tracks close to the interaction point (Fig. 6.6 right panel) even if those tracks were produced by the photon conversion on a detector material.

The background is rejected by tracing back the tracks of the e^+, e^- candidates and reconstructing their invariant mass ($M_{e^+e^-}$) assuming that they originate from the BP or DCW surfaces and calculating distance ($D_{e^+e^-}$) between them on the conversion surface.

In case of conversion at the conversion surface, the distance between two tracks ($D_{e^+e^-}$) should be minimum and the invariant mass ($M_{e^+e^-}$) should be small (close to zero at the GeV scale). These informations were used to develop the rejection algorithm for this kind of background. Thus, $\phi \to \eta\gamma$ background is reduced by rejecting events with:

$$M_{e^+e^-}(BP) < 10 \text{ MeV and } D_{e^+e^-}(BP) < 2 \text{ cm} ,$$
$$M_{e^+e^-}(DCW) < 80 \text{ MeV and } D_{e^+e^-}(DCW) < 10 \text{ cm} ,$$

where $M_{e^+e^-}(BP)$ and $M_{e^+e^-}(DCW)$ are the invariant masses of electron-positron pair calculated on BP and DCW surfaces, respectively. The performed cuts are presented in Fig. 6.7 and Fig. 6.8.

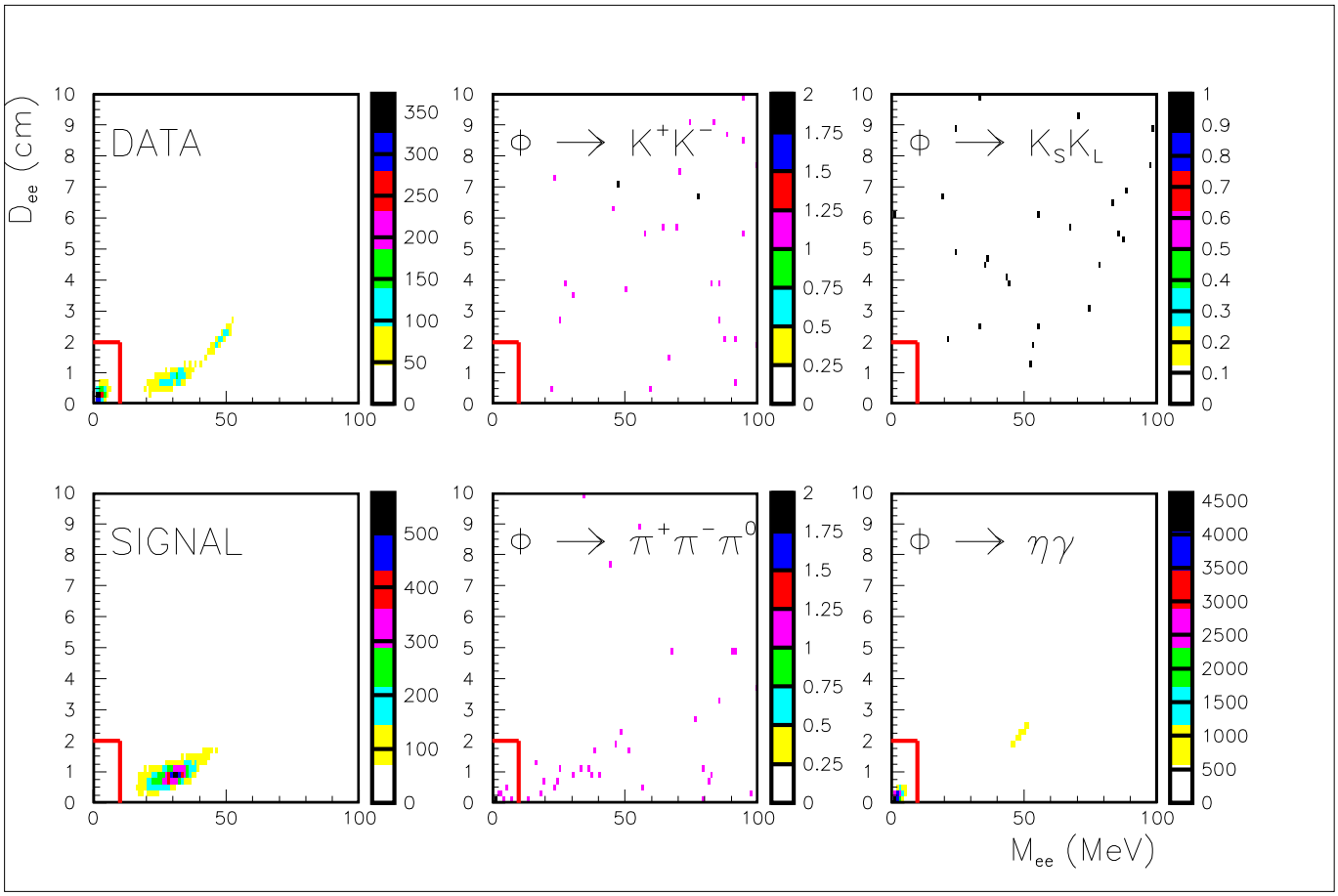

Figure 6.7: Conversion variables evaluated on BP surface. The distance between two tracks on BP surface, $D_{e^+e^-}(BP)$, is shown on Y axis as a function of invariant mass, $M_{e^+e^-}(BP)$, (X axis). The experimental result is shown in left-upper figure. The other figures show result of simulations of $\phi \to K^+K^-$ (top center), $\phi \to K_S K_L$ (top right), signal $\phi \to \eta e^+e^-$ (bottom left), $\phi \to \pi^+\pi^-\pi^0$ (bottom center), $\phi \to \eta\gamma$ (bottom right). The events inside the red box at low $M_{e^+e^-}$ and $D_{e^+e^-}$ values are rejected. The results of simulations aren't normalized in amplitude to the experimental luminosity.

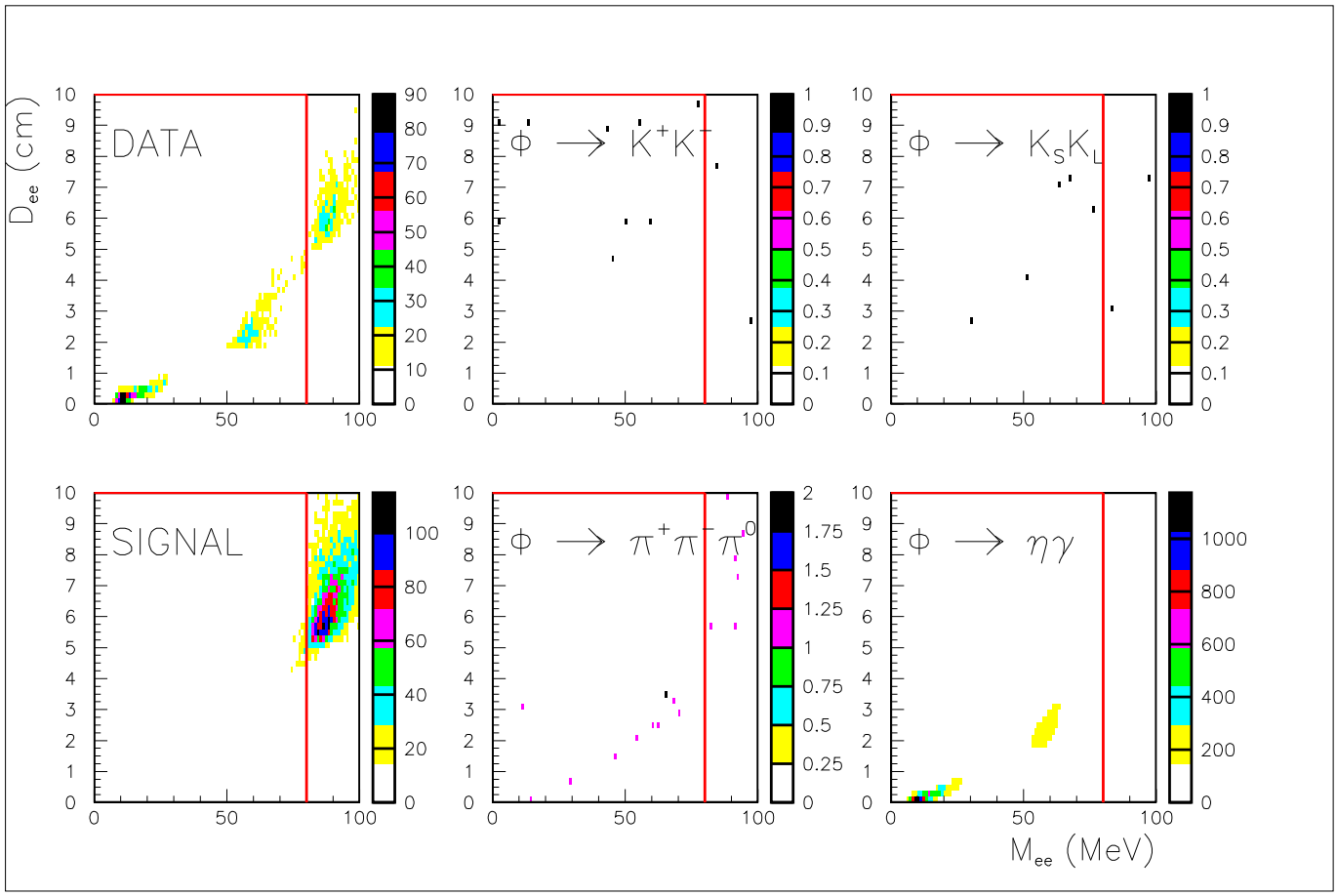

Figure 6.8: Conversion variables evaluated on DCW surface. The distance between two tracks on DCW surface, $D_{e^+e^-}(DCW)$, is shown on Y axis as a function of invariant mass, $M_{e^+e^-}(DCW)$, (X axis). The experimental result is shown in left-upper figure. The other figures show result of simulations of $\phi \to K^+K^-$ (top center), $\phi \to K_S K_L$ (top right), signal $\phi \to \eta e^+e^-$ (bottom left), $\phi \to \pi^+\pi^-\pi^0$ (bottom center), $\phi \to \eta\gamma$ (bottom right). The events inside the red box at low $M_{e^+e^-}$ and $D_{e^+e^-}$ values are rejected. The results of simulations aren't normalized in amplitude to the experimental luminosity.

The second relevant background, originating from $\phi \to K_S K_L \to \pi^+\pi^-\pi^+\pi^-\pi^0$ decays (Fig. 6.9) is due to missidentification of pions with electrons in the final state and can be suppressed using time-of-flight (TOF) to the calorimeter.

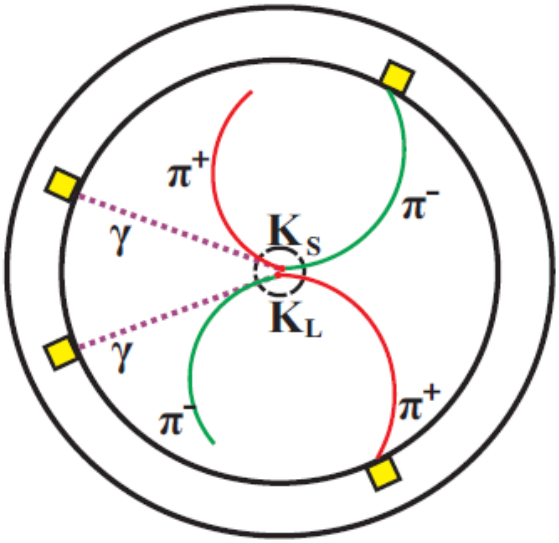

Figure 6.9: Pictorial view of background process $\phi \to K_S K_L \to \pi^+\pi^-\pi^+\pi^-\pi^0$ with $\pi^0 \to \gamma\gamma$. This background can fake the signal topology in the final state when one $\pi^+\pi^-$ pair will be reconstructed as a e^+e^- pair.

When cluster is connected to a track, the arrival time to the calorimeter is evaluated both using the calorimeter timing ($T_{\rm cluster}$) and the particle trajectory ($T_{\rm track} = L_{\rm track}/\beta c$). The $\Delta T = T_{\rm track} - T_{\rm cluster}$ variable is then evaluated for both electron (ΔT_e) and pion (ΔT_π) mass hypotheses. Events with an e^+, e^- candidate outside a 3σ's window on the ΔT_e variables are rejected (Fig. 6.10).

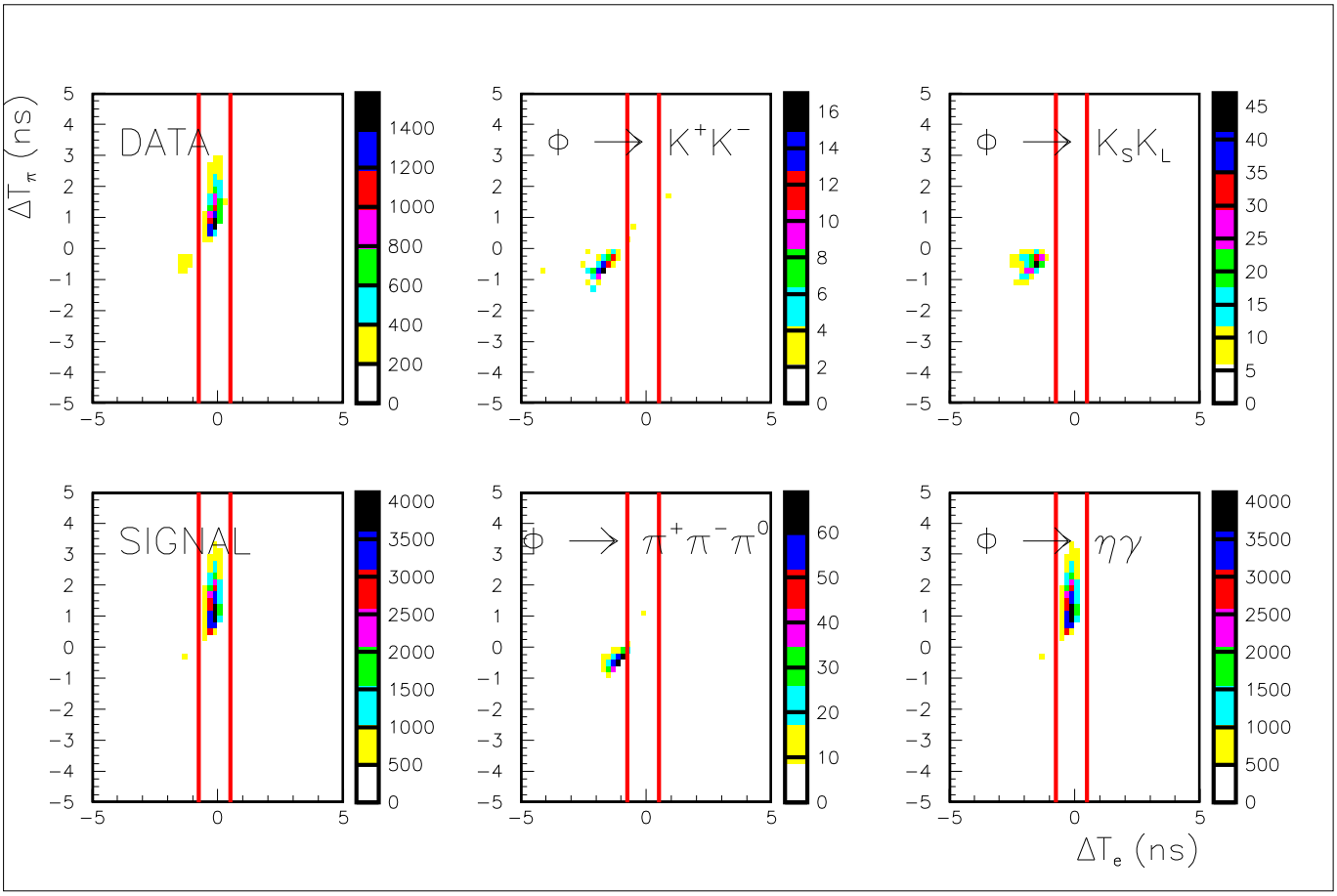

Figure 6.10: Time-of-flight variables for e^+e^- candidates. The difference between a time of cluster and a reconstructed time from momentum is evaluated for both the electron (x-axis) and the pion (y-axis) mass hypotheses. The experimental result is shown in left-upper figure. The other figures show the result of simulations of $\phi \to K^+K^-$ (top center), $\phi \to K_S K_L$ (top right), signal (bottom left), $\phi \to \pi^+\pi^-\pi^0$ (bottom center), $\phi \to \eta\gamma$ (bottom right). Red lines show the 3σ cut applied on the ΔTe variable (-0.75 $<$ ΔTe $<$ 0.5 ns). The results of simulations aren't normalized in amplitude to the experimental luminosity. Details are described in the text.

Fig. 6.11 shows a ΔT_{e+} distribution determined for positron hypothesis.

The last preselection cut was done on distribution of recoil mass for the $\phi \to e^+e^-\pi^+\pi^- X$ decay. In the case of signal the mass of X should be equal to the mass of the π^0 meson. Therefore, events in the range 100-160 MeV are accepted for the further analysis (Fig. 6.12).

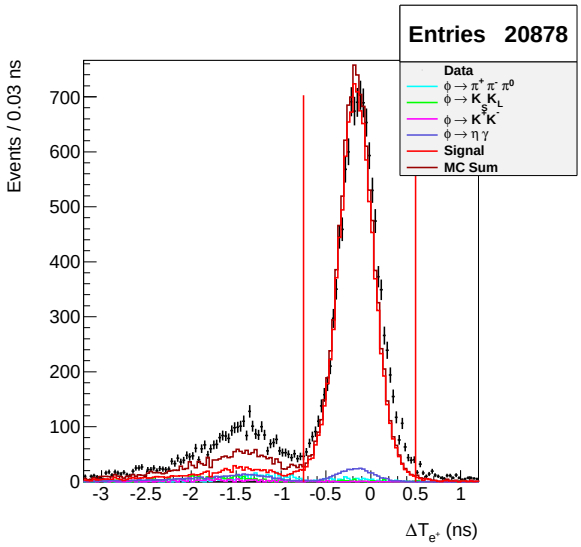

Figure 6.11: ΔT_{e^+} distribution for positron candidate. The red lines denote the performed cut. The events in the range from -0.75 to 0.5 ns are accepted. The points denote experimental data and coloured histograms correspond to results of simulations of the decays as indicated in the legend. The results of simulations are normalized in amplitude to the experimental luminosity (1.52 fb^{-1}).

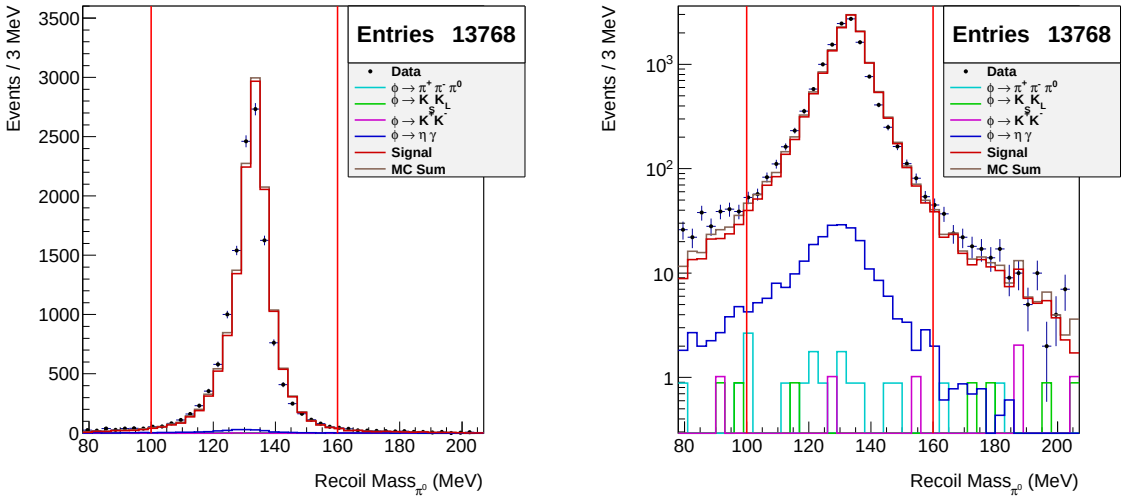

Figure 6.12: Recoil mass of the $\phi \to e^+e^-\pi^+\pi^- X$ decay presented in linear scale (left) and logarithmic scale (right). The red lines denote the performed cut. Events in the range from 100 to 160 MeV are accepted. The points denote experimental data and coloured histograms correspond to results of simulations of the decays as indicated in the legend. The results of simulations are normalized in amplitude to the experimental luminosity (1.52 fb^{-1}).

In Tab. 6.1 the total and relative efficiency for signal selection at different steps of the analysis

chain are shown. The main drop of signal events is due to the detector acceptance. The overall efficiency is equal to 10.04%.

Cut	ε_{rel} *(%)*	ε_{total} *(%)*
4trks+2γ's	21.59	21.59
$M_{inv}(\gamma\gamma)$	96.39	20.81
$M_{recoil}(e^+e^-)$	63.55	13.23
$M_{inv}(\pi^+\pi^-\pi^0)$	97.06	12.84
Conv. Cut	92.42	11.86
Tof Cut	86.89	10.31
$M_{recoil}(\pi^0)$	98.11	10.04

Table 6.1: Total and relative analysis efficiency. The ε_{rel} indicates efficiency for a signal selection after application of a „cut" described in the first column.

The efficiency of the $\phi \to \eta e^+e^-$ identification as a function of invarinat mass of e^+e^- pair is presented in Fig. 6.13. The efficiency is ranging from about 7% to around 16%.

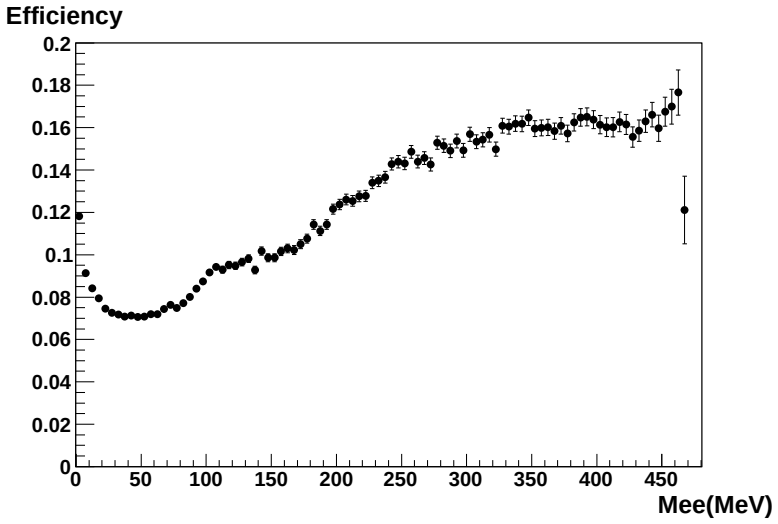

Figure 6.13: Simulations of the signal reconstruction efficiency as a function of invariant mass of electron-positron pair.

The invariant mass spectra of e^+e^- pair for data and simulated signal and background at each analysis step, are presented in Fig. 6.14. Worth to mention is that after the preselection the analysed data sample is very clean. There is less than 2% background contamination mainly coming from $\phi \to \eta\gamma$ channel with conversion of the γ quantum on detector material.

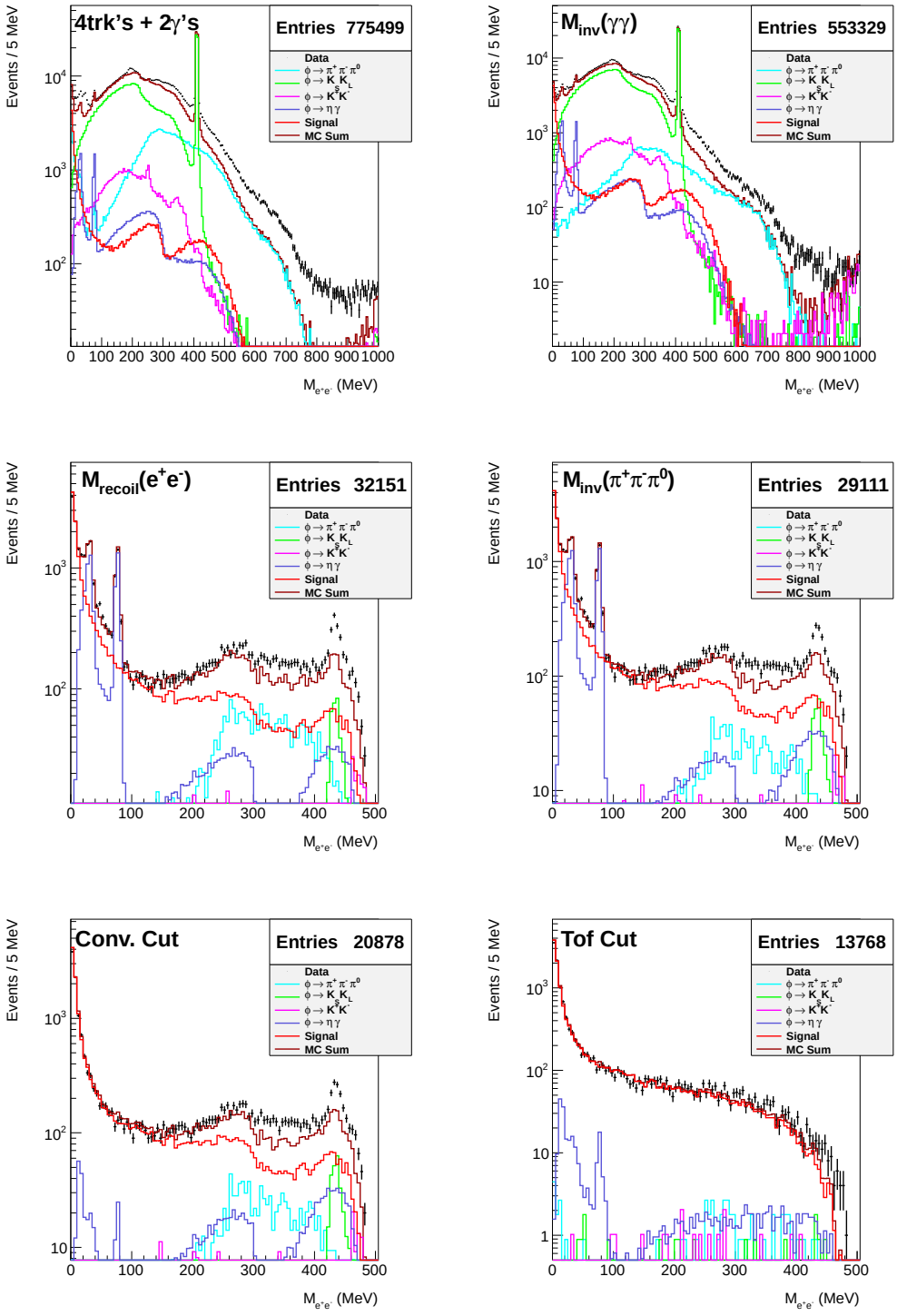

Figure 6.14: The distribution of invariant mass of e^+e^- pair, after each level of selection. The abbreviation of the name of selection criterium is indicated in the left, upper corner of each plot. Points denote experimental data and coloured histograms correspond to results of simulations of the decays as indicated in the legend. Results of simulations were normalized in amplitude to the experimental luminosity (1.52 fb^{-1}).

The final distribution of invariant mass of e^+e^- pair after application of all selection criteria, including cut on recoil mass of π^0, ($M_{recoil}(\pi^0)$), is presented in Fig. 6.15.

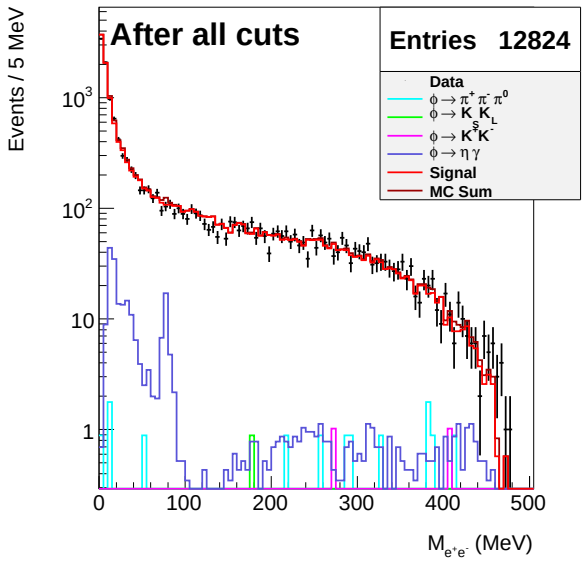

Figure 6.15: The distribution of the invariant mass of e^+e^- pair, after all analysis cuts discussed in this section and listed in Tab. 6.1. The points denote experimental data and coloured histograms correspond to results of simulations of the decays as indicated in the legend. The results of simulations are normalized in amplitude to the experimental luminosity (1.52 fb^{-1}).

6.3 Background subtraction

Two methods were compared in this analysis in order to subtract the background in the $M_{e^+e^-}$ spectrum. In the first method the background was estimated based on simulations and the simulated spectra were subtracted from the experimental result. In the second method the background was estimated for each $M_{e^+e^-}$ interval separately based on the experimental distribution of recoil mass of e^+e^- pair.

6.3.1 Estimation of background based on simulations

The results of simulations, of the background channels are shown in Fig. 6.15 by coloured histograms. The invariant mass distribution of e^+e^- pair after subtraction of background estimated based on simulations normalized to the experimental luminosity (1.52 fb^{-1}) is presented in Fig. 6.16.

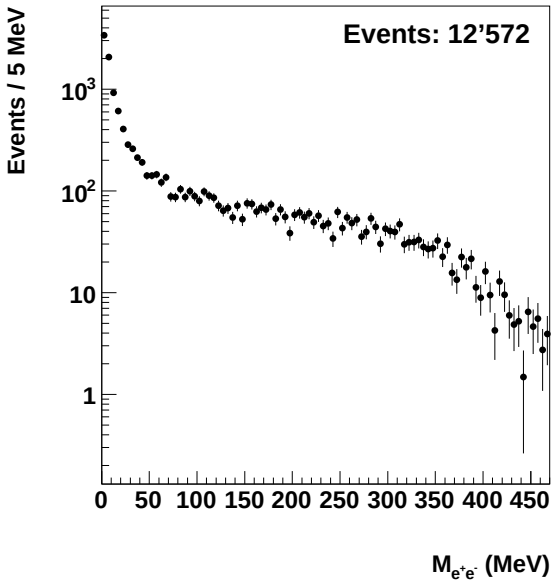

Figure 6.16: The distribution of invariant mass of e^+e^- pair for the $\phi \to \eta e^+e^-$ decay, after subtraction of background estimated based on simulations.

6.3.2 Estimation of background for each $M_{e^+e^-}$ interval separately

To perform subtraction of background for each $M_{e^+e^-}$ interval separately, we resigned from using cut on the recoil mass distribution directly, but instead we plot the recoil mass of e^+e^- distribution for each bin of $M_{e^+e^-}$ spectrum and using polynomial fit to the side bands we estimated the background in the region of the η meson mass in the window 535-560 MeV. All distributions of $M_{e^+e^-}$ are presented in panels of Fig. 6.17-6.20. The red lines correspond to the polynomial fits described by the mathematical function:

$$F(mm, a, b, c) = a + b \cdot mm + c \cdot mm^2, \tag{6.1}$$

where mm denotes the missing mass and a,b and c are the free parameters varied during the fit. The blue lines indicate the signal region (535-560 MeV) and the dark green line, in the middle between two blue lines, indicates the η mass value equal to 547.853 MeV [1]. The signal region range (535-560 MeV) is the same as which was used in the analysis where background subtraction was based on simulations.

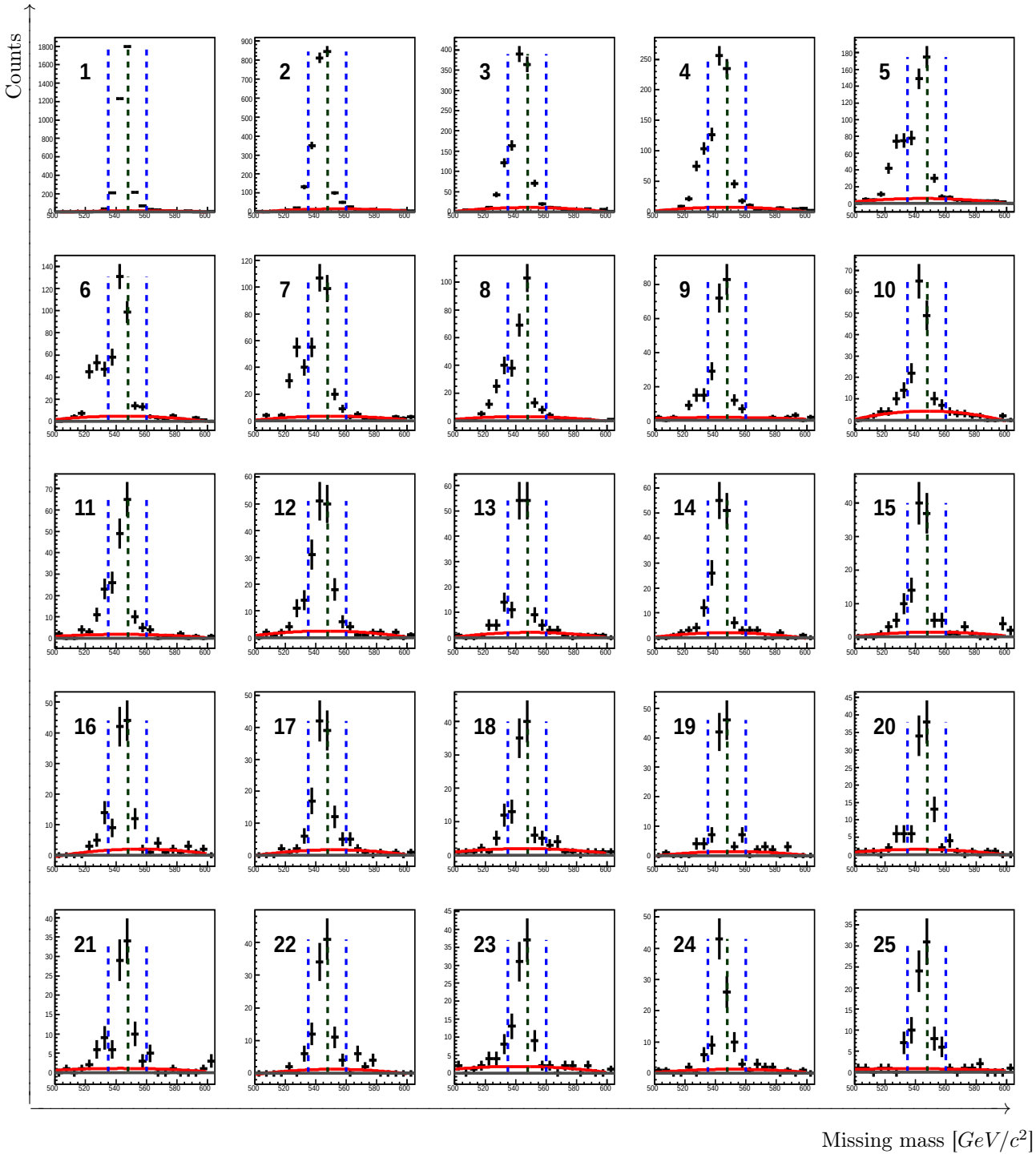

Figure 6.17: The distribution of recoil mass, of e^+e^- pair, $M_{recoil}(e^+e^-)$, of experimental data. Each distribution is performed for 5 MeV bin from invariant mass of e^+e^- distribution. Bins with number from 1 to 25 correspond to range of $M_{e^+e^-}$ from 0 to 125 MeV. Number of the $M_{e^+e^-}$ bin is indicated inside the figure. The blue lines indicate the signal region (535-560 MeV) and the dark green line, in the middle between two blue lines, indicates the η mass value equal to 547.853 MeV [1].

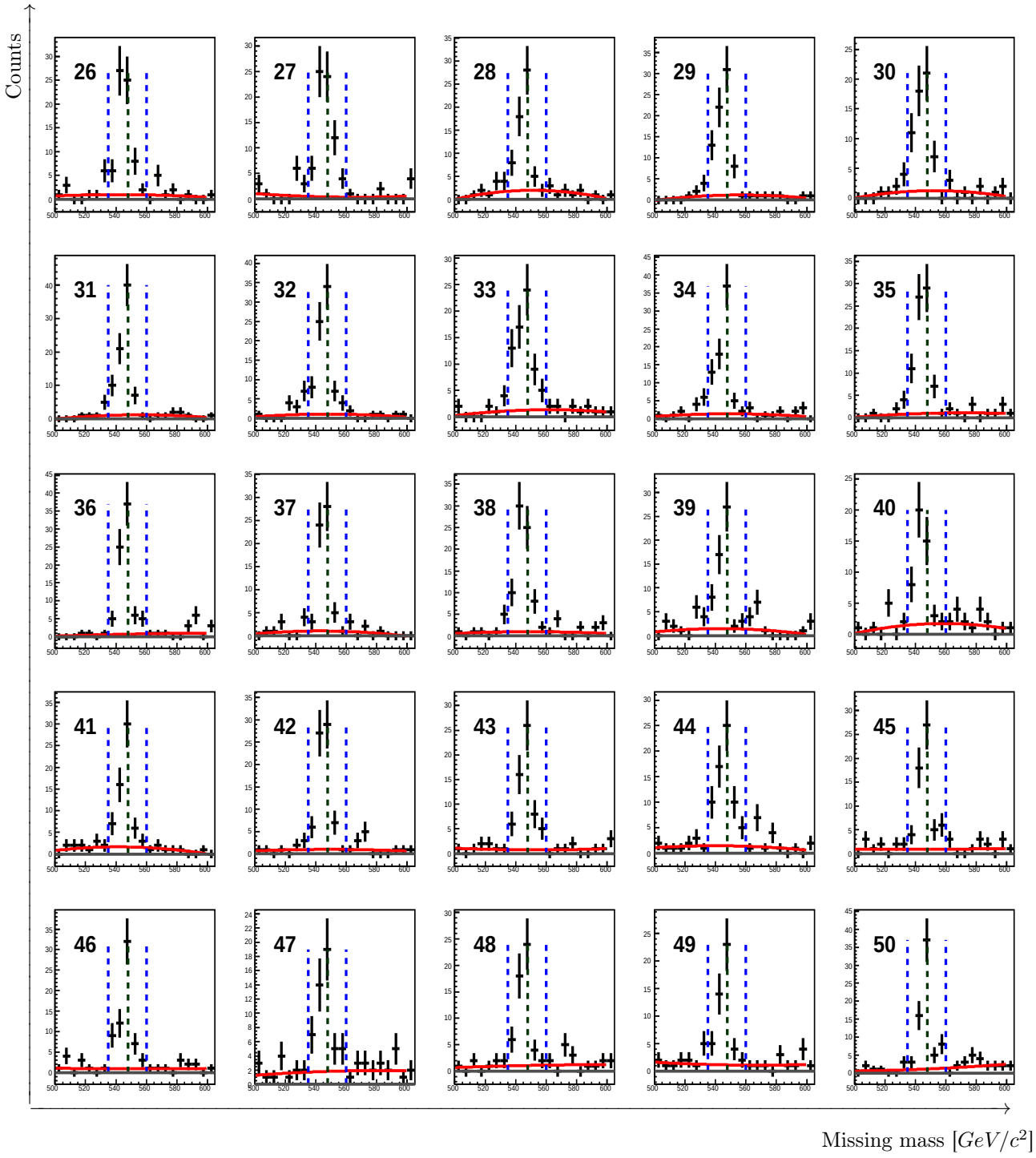

Figure 6.18: The distribution of recoil mass, of e^+e^- pair, $M_{recoil}(e^+e^-)$, of experimental data. Each distribution is performed for 5 MeV bin from invariant mass of e^+e^- distribution. Bins with number from 26 to 50 correspond to range of $M_{e^+e^-}$ from 125 to 250 MeV. Number of the $M_{e^+e^-}$ bin is indicated inside the figure. The blue lines indicate the signal region (535-560 MeV) and the dark green line, in the middle between two blue lines, indicates the η mass value equal to 547.853 MeV [1].

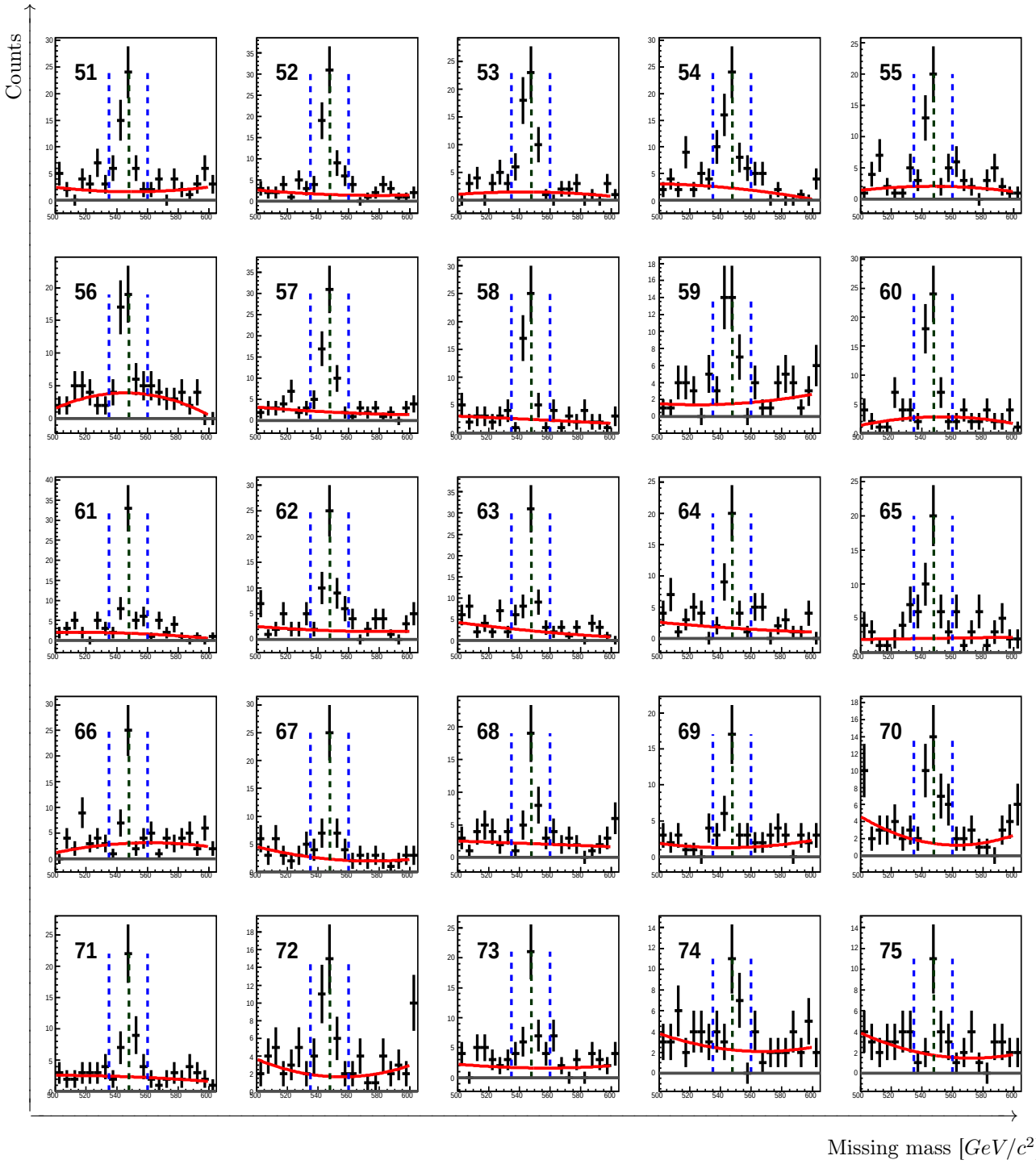

Figure 6.19: The distribution of recoil mass, of e^+e^- pair, $M_{recoil}(e^+e^-)$, of experimental data. Each distribution is performed for 5 MeV bin from invariant mass of e^+e^- distribution. Bins with number from 51 to 75 correspond to range of $M_{e^+e^-}$ from 250 to 375 MeV. Number of the $M_{e^+e^-}$ bin is indicated inside the figure. The blue lines indicate the signal region (535-560 MeV) and the dark green line, in the middle between two blue lines, indicates the η mass value equal to 547.853 MeV [1].

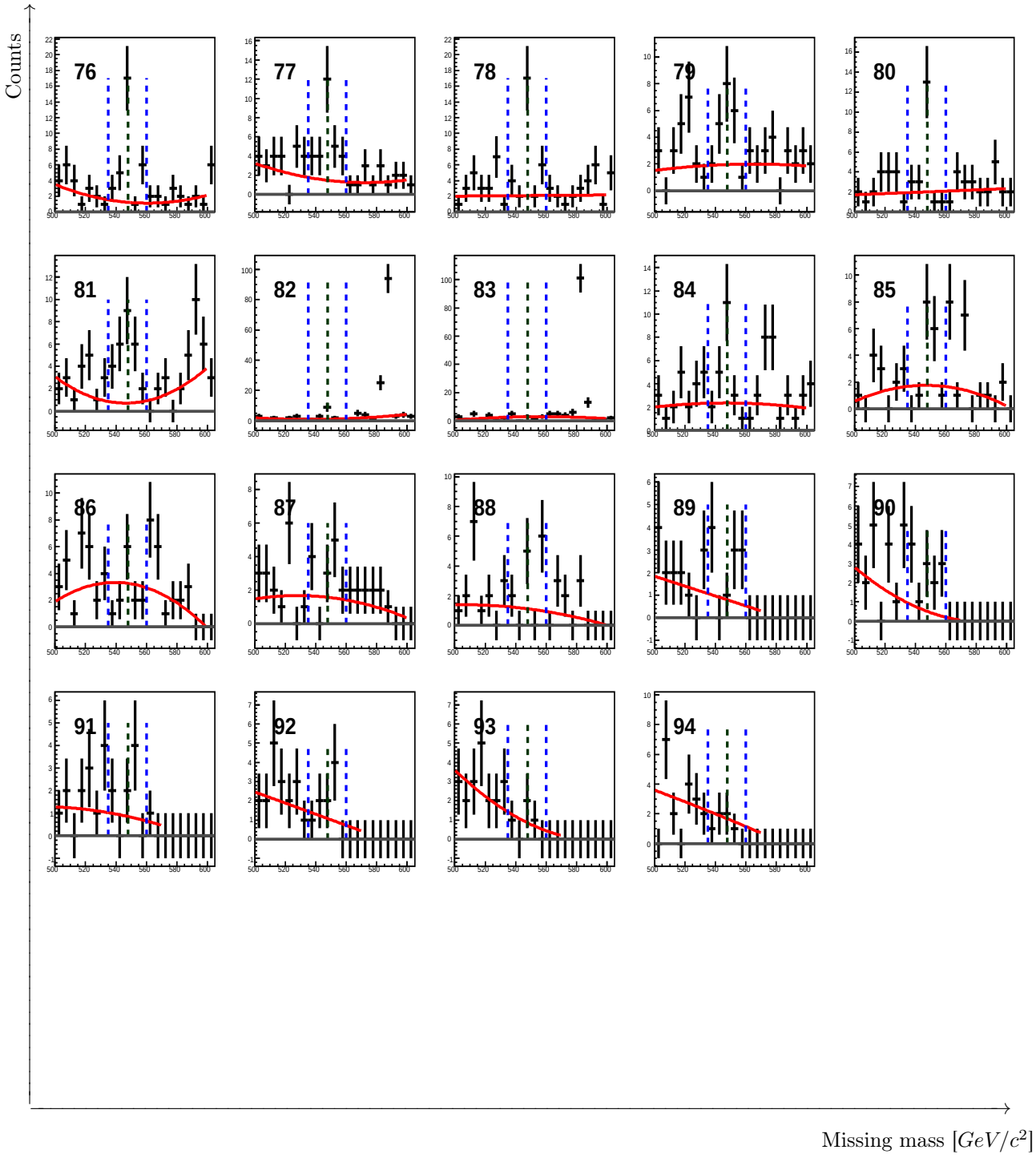

Figure 6.20: The distribution of recoil mass, of e^+e^- pair, $M_{recoil}(e^+e^-)$, of experimental data. Each distribution is performed for 5 MeV bin from invariant mass of e^+e^- distribution. Bins with number from 76 to 94 correspond to range of $M_{e^+e^-}$ from 375 to 470 MeV. Number of the $M_{e^+e^-}$ bin is indicated inside the figure. The blue lines indicate the signal region (535-560 MeV) and the dark green line, in the middle between two blue lines, indicates the η mass value equal to 547.853 MeV [1].

The distribution of the invariant mass of e^+e^- pair after all analysis cuts and after background subtraction for each $M_{e^+e^-}$ interval separately is reported in Fig. 6.21.

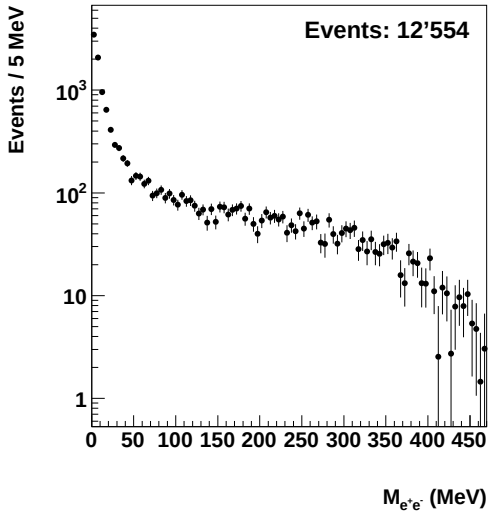

Figure 6.21: Final distribution of the e^+e^- invariant mass for the process $\phi \to \eta\, e^+e^-$ with $\eta \to \pi^+\pi^-\pi^0$ decay chain after subtraction of background performed for each $M_{e^+e^-}$ interval separately.

6.3.3 Comparison of results obtained with two different background subtraction methods

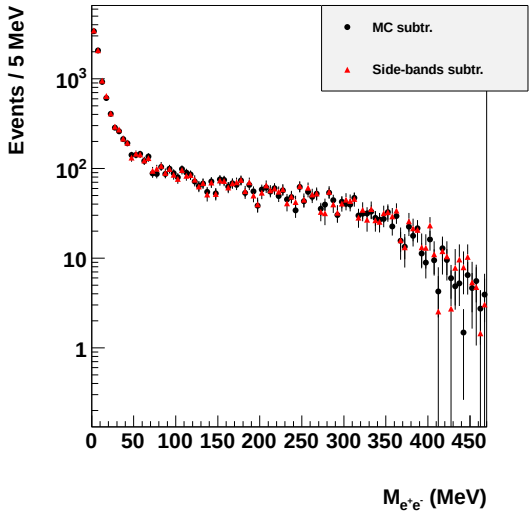

Figure 6.22: Comparison between the $M_{e^+e^-}$ distributions obtained after subtraction of simulated background (black dots) and after subtraction of background using the side-bands method on recoil mass spectrum (red triangles).

After performed selection procedure, final sample of around 13′000 events of $\phi \to \eta\, e^+e^-$ reaction were reconstructed. The statistics is almost two orders of magnitude larger than in any previous measurement. It is important to stress that the remained background is less than 2% in the final sample and that two methods of the background subtraction gave the consistent result (see Fig. 6.22).

7. Results

7.1 Branching Ratio extraction

After the subtraction of the background we obtained 12554 of $\phi \to \eta e^+ e^-$ events[1].

The value of the efficiency, defined as the ratio between the number of generated events and the number of the events at the end of the analysis is equal to 10.04%. The branching ratio of the $\phi \to \eta e^+ e^-$ decay was determined using a following formula:

$$\begin{aligned} N_{data} &= \varepsilon \cdot L \cdot \sigma_{e^+e^- \to \phi} \cdot BR(\phi \to \eta e^+ e^-) \cdot BR(\eta \to \pi^0\pi^+\pi^-) \ , \\ BR(\phi \to \eta e^+ e^-) &= \frac{N_{data}}{\varepsilon \cdot L \cdot \sigma_{e^+e^- \to \phi} \cdot BR(\eta \to \pi^0\pi^+\pi^-)} \ , \\ BR(\phi \to \eta e^+ e^-) &= \frac{12554}{0.1004 \cdot 1.5163 \cdot 10^6 \cdot 3100 \cdot 0.2274} = 1.170 \cdot 10^{-4} \ , \end{aligned} \tag{7.1}$$

where $\mathcal{L}$=1.5163 fb^{-1} is the integrated luminosity, σ=3100 nb is the cross section of the $e^+e^- \to \phi$ process and ε=0.1004 denotes the analysis efficiency. The N=12554 is the number of the reconstructed signal events, $BR_{\eta \to \pi^0\pi^+\pi^-} = 0.2274$ is the branching ratio of $\eta \to \pi^0\pi^+\pi^-$ decay. The statistical error of evaluated BR reads:

$$\begin{aligned} BR^2_{error} &= (\mid \frac{dBR}{d\mathcal{L}} \mid \cdot \Delta\mathcal{L})^2 + (\mid \frac{dBR}{d\sigma} \mid \cdot \Delta\sigma)^2 + (\mid \frac{dBR}{dN} \mid \cdot \Delta N)^2 + \\ &+ (\mid \frac{dBR}{d\varepsilon} \mid \cdot \Delta\varepsilon)^2 + (\mid \frac{dBR}{dBR\eta} \mid \cdot \Delta BR\eta)^2 \ , \\ BR_{error} &= 0.035 \cdot 10^{-4} \ , \end{aligned} \tag{7.2}$$

where $\Delta\mathcal{L}$=0.6%·1.52 fb^{-1}=9.12 pb^{-1}, $\Delta\sigma$=80 nb, $\Delta N = \sqrt{N_{all}} = \sqrt{12824} \approx 113$, $\Delta\varepsilon \approx \sqrt{\varepsilon(1-\varepsilon)/\mathrm{N_{gen.}}} \approx 0$ [67] and $\Delta BR_{\eta \to \pi^0\pi^+\pi^-}$=0.28% [1]. In table 8.2, the result of this analysis is compared to the results from the measurements of SND and CMD-2 experiments. One can see that it is in agreement with results of previous measurements performed by CMD-2 and SND collaborations and also with the theoretical predictions in the framework of VMD and Leupold models.

	Theory		*Experiment*		
	VMD	Leupold	CMD-2	SND	**Our analysis**
Branching Ratio (10^{-4})	1.1	1.13 ± 0.14	1.14±0.16	1.19 ± 0.31	$\mathbf{1.170 \pm 0.035}$

Table 7.1: Branching ratio of the $\phi \to \eta e^+ e^-$ decay determined in this work compared to SND and CMD-2 results, and to theoretical predictions.

[1] This was determined by integrating the $M_{e^+e^-}$ distribution obtained after background subtraction for each $M_{e^+e^-}$ interval separately.

7.2 Extraction of the transition form factor slope

The slope of form factor was extracted directly from data by performing the fit to the final invariant mass distribution[2]. The decay parametrization is taken from Ref. [2]. The used formula is presented in Eq. 7.3:

$$\frac{d\Gamma(\phi \to \eta\, e^+e^-)}{dq^2} =$$

$$\frac{\alpha}{3\pi}\frac{|F_{\phi\eta}(q^2)|^2}{q^2}\sqrt{1-\frac{4m^2}{q^2}}\left(1+\frac{2m^2}{q^2}\right)\cdot\left[\left(1+\frac{q^2}{m_\phi^2-m_\eta^2}\right)^2-\frac{4m_\phi q^2}{\left(m_\phi^2-m_\eta^2\right)^2}\right]^{\frac{3}{2}}\,, \qquad (7.3)$$

with

$$F_{\phi\eta}(q^2) = \frac{1}{1-q^2/\Lambda^2_{\phi\eta}}\,, \qquad (7.4)$$

which is the form factor parametrization in one-pole approximation and $q^2 = M^2_{e^+e^-}$. Performing the fit to the $M_{e^+e^-}$ distribution using the MINUIT package [66] and using Eq. 7.3 we extracted the $\Lambda_{\phi\eta}$ value. The theoretical function was corrected by taking into account the analysis efficiency and experimental smearing. The fit parameters are $\Lambda_{\phi\eta}$ (reported in Eq. 7.4) and an overall normalisation parameter. Each simulated bin has been corrected for its analysis efficiency (ε_i) and smeared using smearing matrix ($A(j,i)$), representing the probability for the signal event to migrate from the i^{th} to the j^{th} bin either due to resolution or to a wrong reconstruction of the event:

$$TC_j = \sum_i T_i \cdot \varepsilon_i \cdot A_{j,i}\,, \qquad (7.5)$$

where j denotes a reconstructed bin and i a simulated bin, T denotes calculated values for theory function and TC the corrected theory function with smearing matrix and efficiency values. The smearing matrix and efficiency value have been evaluated by simulations.

To estimate $\Lambda_{\phi\eta}$ from the fit, we calculate the χ^2 as follows:

$$\chi^2(\Lambda_{\phi\eta}, Norm) = \sum_j \frac{(N_j^{exp} - TC_j(\Lambda_{\phi\eta}, Norm))^2}{\delta^2_{Sj}}\,, \qquad (7.6)$$

where δ_S denotes the statistical uncertainty and $Norm$ is a normalisation parameter. Then χ^2 was minimized. Only the experimental bins inside the kinematical boundaries of the Dalitz plot are used to evaluate the χ^2. Analysis efficiency as a function of $M_{e^+e^-}$, evaluated for $\phi \to \eta e^+e^-$ events, was reported in Fig. 6.13 in the previous chapter. Smearing effects, important mostly in the first energy bins (0-10 MeV), are of the order of few percents. In Fig. 7.1 the smearing matrix for the generated vs reconstructed M_{e+e-} values is reported. As the result of the fit we found[3]:

$$\Lambda_{\phi\eta} = (0.872 \pm 0.075)\ \text{GeV}\,, \qquad (7.7)$$

which corresponds to the form factor slope ($b_{\phi\eta} = \Lambda^{-2}_{\phi\eta}$)[4]:

$$\mathrm{b}_{\phi\eta} = (1.32 \pm 0.23)\ \text{GeV}^{-2}\,, \qquad (7.8)$$

[2] As a final $M_{e^+e^-}$ distribution we used the one with background subtraction performed by polynomial fit to side-bands.

[3] The theoretical calculation based on VMD gives $\Lambda_{\phi\eta} = 1.0\ GeV$ [68].

[4] The form factor slope is defined as: $b_{\phi\eta} = \frac{dF}{dq^2}|_{q^2=0}$, and in one-pole approximation it is equal to $\Lambda^{-2}_{\phi\eta}$.

with $\chi^2/\mathrm{ndf} = 0.92$ and $\mathrm{prob}(\chi^2) \approx 76\%$. The result is in agreement with VMD theory predictions. The central value is different from the result obtained by the SND experiment [3] (see Tab. 7.2). The slope parameter error was estimated using the following method (Eq. 7.9):

$$\triangle b_{\phi\eta} = |\frac{db_{\phi\eta}}{d\Lambda_{\phi\eta}}| \cdot \triangle\Lambda_{\phi\eta} = 2\Lambda_{\phi\eta}^{-3} \cdot \triangle\Lambda_{\phi\eta} = 0.23\ GeV^{-2}\ . \tag{7.9}$$

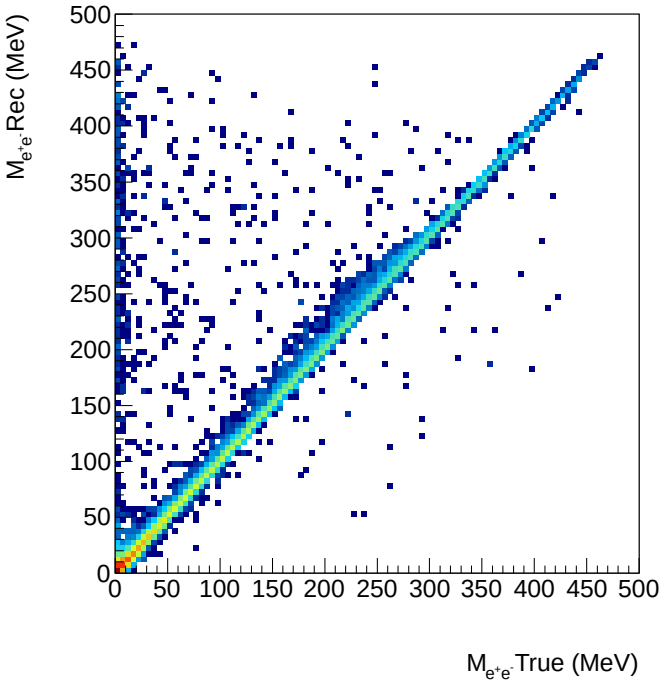

Figure 7.1: Distribution of reconstructed ($M_{e^+e^-}Rec$) versus generated mass ($M_{e^+e^-}True$) of the e^+e^- pair from simulations of $\phi \to \eta e^+e^-$ decay. For each generated $\phi \to \eta e^+e^-$ event a response of the KLOE detector was determined and after that the same analysis was performed like for the experimental data.

	Theory			*Experiment*	
	VMD	Leupold	Ivashyn	SND	**Our analysis**
$b_{\phi\eta}$ (GeV^{-2})	1.0	2.74±0.87	1.94	3.8 ± 1.8	$\mathbf{1.32 \pm 0.23}$

Table 7.2: Comparison of the form factor slope determined in this thesis with experimental results of SND and with the theoretical predictions.

The result of the fit is shown in Fig. 7.2.

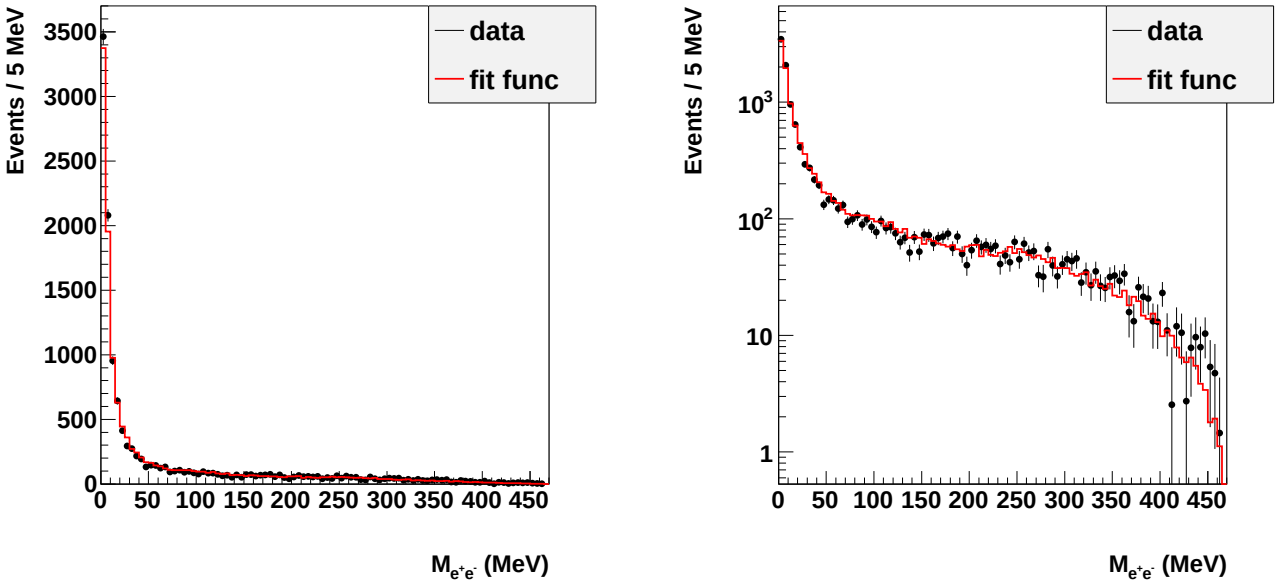

Figure 7.2: Fit (Eq. 7.6) to the $M_{e^+e^-}$ spectrum for $\phi \to \eta e^+e^-$ candidates, both in linear (left) and logarithmic (right) scale. As a result of the fit the $\Lambda_{\phi\eta} = (0.872 \pm 0.075)$ GeV was determined.

Fit normalized residuals, defined as $\frac{(N_{data}-N_{fit})}{\sigma_{data}}$, for fit presented in Fig 7.2, are shown in Fig. 7.3. It can be see that distribution of differences between experimental data and fitted function are as expected from the statistical errors.

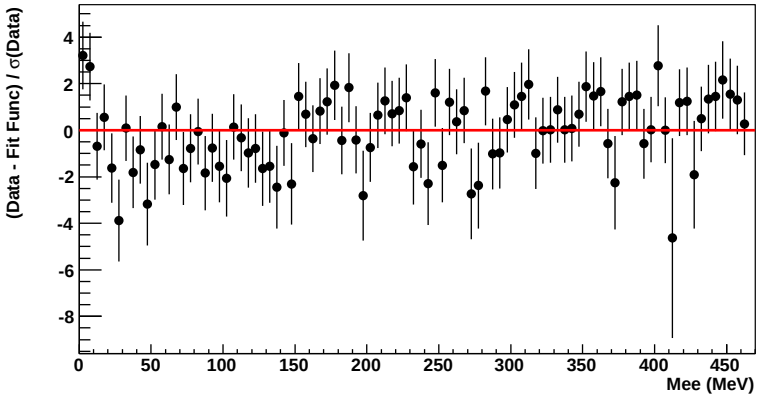

Figure 7.3: Residuals of the fit normalized to uncertainty (σ) of data. σ denotes the statistical error of each bin.

In order to extract a form factor dependence as a function of $M_{e^+e^-}$ the experimental data points were divided by the simulated points with transition form factor equal to one. Both distributions, shown in Fig. 7.4 (the experimental data and simulated with FF equal to one) were corrected for efficiency.

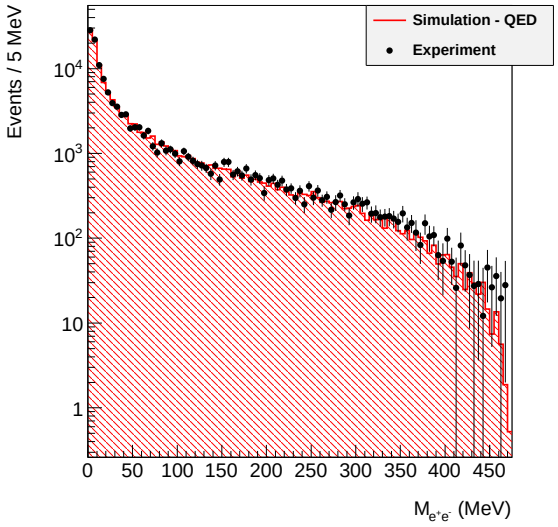

Figure 7.4: Experimental spectrum of the $M_{e^+e^-}$ after the background subtraction (black points) and the signal simulated with the transition form factor equals to one (red area). Both distributions are corrected for efficiency.

The resulting distribution of the transition form factor squared, $|F_{\phi\eta}|^2$, as a function of the invariant mass of the electron-positron pair, $M_{e^+e^-}$, is presented in Fig. 7.5.

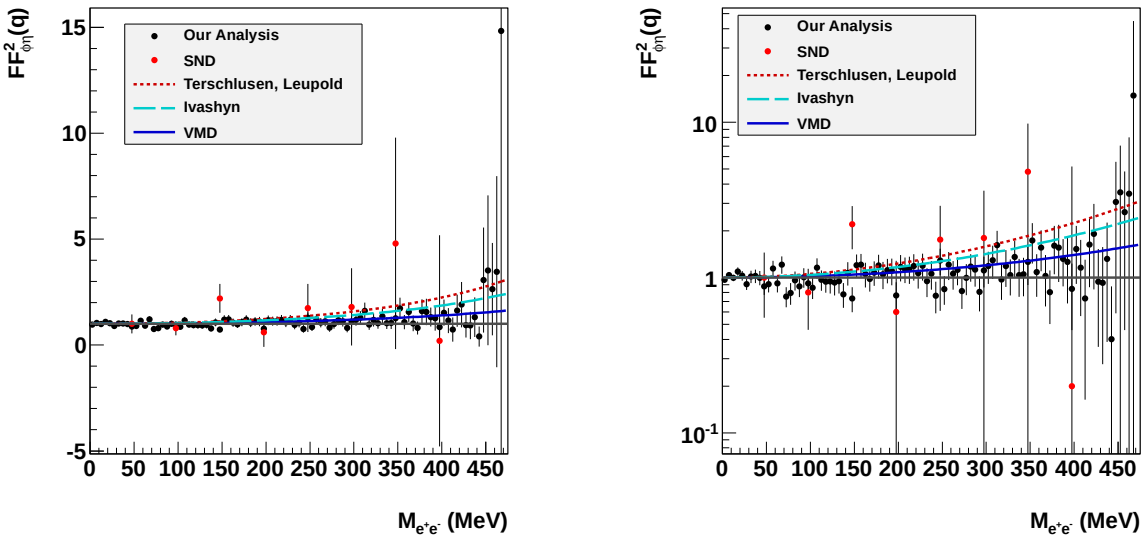

Figure 7.5: Experimental spectrum of the squared transition form factor, $|F_{\phi\eta}|^2$, as a function of $M_{e^+e^-}$. The result of SND experiment is compared to the result of this thesis using linear (left) and logarithmic scale (right). Superimposed lines described in the legend indicates results predicted by Leupold, Ivashyn and VMD models.

The data are compared to the predictions of VMD, Leupold and Ivashyn models. One can see that the predictions of VMD model are the closest to the data points, however none of the model describes the data well.

7.3 Charge radius of the ϕ meson

For medium-mass quarks in a non-relativistc description it is possible to calculate radius of charge distribution of mesons, using the Chou-Yang hypothesis [69, 70]. According to this model the radius of charge distribution of the ϕ meson is equal to:

$$< r_\phi^2 >^{1/2} \simeq 0.37^{+0.20}_{-0.37}\ fm\,. \tag{7.10}$$

Having the slope parameter of the $\phi - \eta$ system, one can attempt to evaluate its radius of charge distribution. The charge distribution is related to the form factor by the Fourier transform:

$$F(q^2) = \int d^3r\rho(\mathbf{r})e^{-i\mathbf{q}\cdot\mathbf{r}} \simeq 1 - \frac{q^2}{6} < r^2 > +..., \tag{7.11}$$

where $\frac{<r^2>}{6} = b_{\phi\eta}$. Taking into account a value of $b_{\phi\eta}$ extracted in this thesis we obtain:

$$< r_\phi^2 >^{1/2} \simeq 0.56 \pm 0.05\ fm\,, \tag{7.12}$$

which is in agreement with the theoretical predictions, however the central value is larger than predicted. This quantity was measured experimentally the first time for the ϕ meson.

7.4 Estimation of the systematic uncertainty

The estimation of the systematic uncertainty, for the slope parameter $b_{\phi\eta}$ and BR values, has been done in two ways. Firstly, results ware reevaluated changing the initial condition of each selection criteria separately. The systematic error σ_{syst}, was calculated as the square root of the quadratic sum of all contributions:

$$\sigma_{syst} = \sqrt{\sum (x_i - x_r)^2}\,, \tag{7.13}$$

where x_i is the result obtained by analyzing data with changing the value of the i^{th} condition and x_r is the result obtained by using the final scheme of cuts and background subtraction methods as described in section 6.3.2. The second evaluation of the systematic uncertainty was done based on the method described in [71].

Using the final scheme of cuts, performed in this analysis, we extracted $b_{\phi\eta} = (1.32 \pm 0.23_{stat})$ GeV^{-2} and BR$(\phi \to \eta e^+ e^-) = (1.170 \pm 0.035_{stat}) \cdot 10^{-4}$, the values extracted with changed cuts and contribution to the systematical error for each cut are presented in Tab. 7.3 and 7.4. The check was done, for the cuts used in analysis, by changing the range accepted by each criterium by $\pm 5\%$ of its value used in selection. Below we will discuss the applied changes of the selection criteria. Each change was done separately for individual cuts assuming that the sources of systematic errors are uncorrelated. The following criteria have been tested:

1. **Invariant mass of two γ cut**

   Which was done to select gamma quanta from the π^0 meson.

2. **Invariant mass of $\pi^+\pi^-\pi^0$ cut**

   Used for selection of events from the η meson decay.

3. **Conversion cut**

   Main purpose for this cut was rejection of events coming from conversion of γ with subsequent conversion of γ from radiative channel $\phi \to \eta\gamma$ on detector surface (Beam Pipe or Drift Chamber Wall).

4. **Time-of-flight cut**

   Rejects mainly misidentified events with $2\pi^+2\pi^-$ in the final state coming from the kaons decays.

5. **Missing mass of π^0 cut**

   Used for selection of events coming from π^0.

6. **Missing mass of e^+e^- pair, cut done in the η window (535-560 MeV) for each interval on $M_{e^+e^-}$ distribution**

   Cut performed in order to select events coming from the η meson decay.

7. **Range of $M_{e^+e^-}$ distribution used in fit**

   Additionally, for evaluation of systematic uncertainty of $b_{\phi\eta}$ parameter we estimated the influence to the final result by changing the fit range for three cases (0-420 MeV, 50-420 MeV, 50-470 MeV), for all fits we achieved a consistent value of $b_{\phi\eta}$ parameter.

8. **Bin size of $M_{e^+e^-}$ distribution**

   The next check was done by fitting the $M_{e^+e^-}$ distribution with increased width of each bin from 5 MeV to 10 MeV, also in this case we obtained the consistent result.

9. **Requirement that e^+ and e^- arrive at EMC at appropriate time**

   Finally, the fit stability was checked for time-of-flight cut „fit 2e to EMC". To check the TOF cut we repeated the analysis by retaining only events where e^+ and e^- arrive to the calorimeter and have a TOF consistent with the electron hypothesis. The fit result is in agreement with the precedent result, as shown in Fig. 7.6.

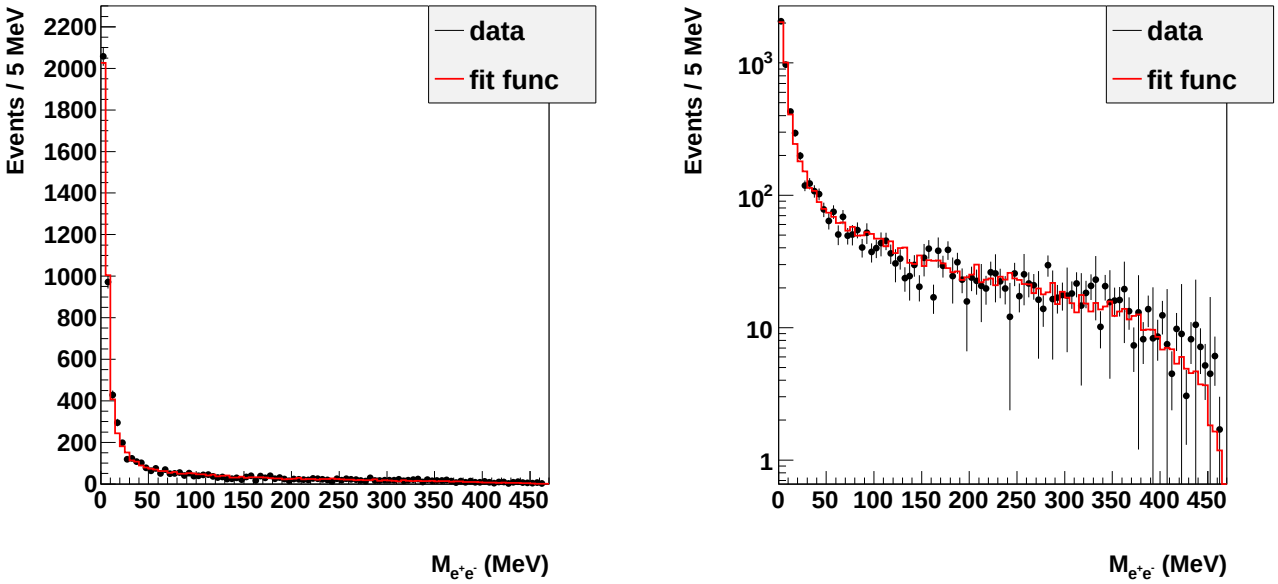

Figure 7.6: Fit to the $M_{e^+e^-}$ spectrum for events for which both e^+ and e^- gave signals in calorimeter with TOF consistent with electron mass hypothesis, both in linear (left) and logarithmic (right) scale.

The extracted slope value is 1.10±0.45 which is in agreement with our final result. Normalized residuals also for this case are shown in Fig. 7.7. The statistical error is larger than previous result because the requirement that e^+e^- pair must give a signal in calorimeter reduced the data sample.

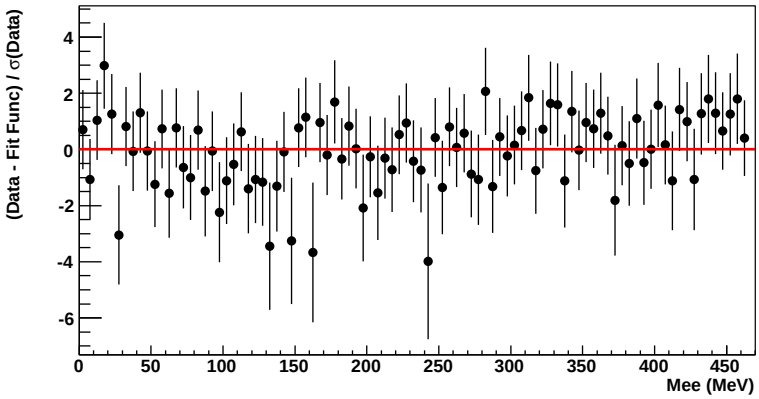

Figure 7.7: Residuals of the fit normalized to uncertainty (σ) of data. σ denotes the statistical error of each bin. This figure shows result for events for which both e^+ and e^- gave signals in calorimeter with TOF consistent with electron mass hypothesis.

10. **Background subtraction method**

Additionally, the estimation of systematic error coming from choosing the background

subtraction method was performed. This uncertainty comes due to the assumption of the shape of $M_{e^+e^-}$ distibution of the background. In order to estimate the influence of those errors to the final result, the number of background events extracted under two different (Section 6.3) assumptions of background shape were compared.

Results of the performed tests are presented in Tab. 7.3.

N.	*Cut*	$b_{\phi\eta}$ (GeV^{-2})	$\lvert\Delta b_{\phi\eta}\rvert$ (GeV^{-2})	$\Lambda_{\phi\eta}$ (GeV)	$\lvert\Delta\Lambda_{\phi\eta}\rvert$ (GeV)	σ (GeV^{-2})	$\Delta\sigma$ (GeV^{-2})	$\frac{\lvert\Delta b_{\phi\eta}\rvert}{\Delta\sigma}$
1.	$M_{inv}(\gamma\gamma)$	1.3078	0.0072	0.8744	0.0024	0.2259	0.0202	0.36
2.	$M_{inv}(\pi^+\pi^-\pi^0)$	1.3204	0.0054	0.8703	0.0017	0.2248	0.0301	0.18
3.	Conv. Cut	1.2957	0.0193	0.8785	0.0065	0.2263	0.0151	1.28
4.	Tof Cut	1.3066	0.0084	0.8748	0.0028	0.2262	0.0165	0.51
5.	$M_{recoil}(\pi^0)$	1.3195	0.0045	0.8705	0.0015	0.2250	0.0285	0.16
6.	$M_{recoil}(e^+e^-)$	1.3051	0.0099	0.8753	0.0033	0.2258	0.0213	0.46
7.	Fit range on $M_{e^+e^-}$							
	50-470 (MeV)	1.3261	0.0111	0.8684	0.0036	0.2327	0.0521	0.05
	0-420 (Mev)	1.2451	0.0699	0.8962	0.0242	0.2059	0.0951	0.34
	50-420 (MeV)	1.4908	0.1758	0.8190	0.0530	0.2971	0.1919	0.59
8.	$M_{e^+e^-}$ interval size	1.3500	0.0350	0.8607	0.0113	0.2497	0.1045	0.33
9.	fit 2e to EMC	1.1010	0.2140	0.9531	0.0811	0.4525	0.3916	0.55
10.	Bkg subtr. via MC	1.3560	0.0410	0.8588	0.0132	0.2596	0.1263	0.32

Table 7.3: Values of $b_{\phi\eta}$ parameter, obtained after changing the range of a cut by 5%. Δ denotes the difference between values obtained with the final scheme of cuts: $\boldsymbol{b_{\phi\eta} = 1.3150\ (GeV^{-2})}$, and the value obtained after a specific test. Details are given in the text.

Taking into account all discussed contributions to the systematic uncertainty and adding the estimated uncertainties in quadrature we obtained the total systematic error. The value of the systematic uncertainty, calculated using Eq. 7.13, for $b_{\phi\eta}$ and $BR(\phi \to \eta e^+e^-)$ amounts to: 0.29 GeV^{-2} and $0.010 \cdot 10^{-4}$, respectively.

It is worth to stress that obtained value of systematic uncertainty agrees within one standard deviation of the statistical uncertainty for $b_{\phi\eta}$ and BR($\phi \to \eta e^+e^-$) case. Therefore, this estimation of the systematic error can be treated as conservative upper limit only.

The second evaluation of the systematic uncertainty was done using the method described in reference [71]. In this approach the deviation of the original result (x_r) with respect to the value extracted with modified cut (x_i), denoted as $\Delta b_{\phi\eta}$ and ΔBR, are compared with $\Delta\sigma$, defined as:

$$\Delta\sigma = \sqrt{|\sigma_r^2 - \sigma_i^2|}\,, \tag{7.14}$$

where σ_r and σ_i denote the statistical uncertainties of x_r and x_i, respectively. And for the estimation of systematic uncertainty only these contributions are taken into account for which the value of $\frac{\Delta b_{\phi\eta}}{\Delta\sigma}$ is larger than one. In opposite case we treate the systematic error value as an upper limit only [71].

Cut	$BR(10^{-4})$	$\lvert\Delta BR(10^{-4})\rvert$	$\sigma(10^{-4})$	$\Delta\sigma(10^{-4})$	$\frac{\lvert\Delta BR\rvert}{\Delta\sigma}$
$M_{inv}(\gamma\gamma)$	1.1718	0.0021	0.0351	0.0026	0.81
$M_{inv}(\pi^+\pi^-\pi^0)$	1.1722	0.0025	0.0351	0.0026	0.96
Conv. Cut	1.1776	0.0079	0.0353	0.0046	1.72
Tof Cut	1.1689	0.0008	0.0351	0.0026	0.31
$M_{recoil}(\pi^0)$	1.1718	0.0021	0.0351	0.0026	0.81
$M_{recoil}(e^+e^-)$	1.1727	0.0030	0.0351	0.0026	1.15
Bkg subtr. via MC	1.1713	0.0016	0.0351	0.0026	0.62

Table 7.4: Values of branching ratio BR, obtained after changing the range of a cut by 5%. Δ denotes the difference between values obtained with the final scheme of cuts: $\boldsymbol{BR = 1.1697 \cdot 10^{-4}}$, and the value obtained after a specific test. Details are given in the text.

Almost all performed checks give a non-significant deviation which manifest itself in $\frac{\Delta b_\phi}{\Delta\sigma}$ less than one. According to the methodology suggested in reference [71] in case of BR for the estimation of systematic uncertainty one should take into account only contributions from test of conversion cut (Conv. Cut) and $M_{recoil}(\pi^0)$ cut and in case of $b_{\phi\eta}$ parameter only from conversion cut. Because only in this case $\frac{\Delta BR}{\Delta\sigma}$ and $\frac{\Delta b_\phi}{\Delta\sigma}$ are larger than one. In this case we would obtain 0.02 GeV^{-2} systematic uncertainty for $b_{\phi\eta}$ parameter and $0.008 \cdot 10^{-4}$ uncertainty for BR.

To summarize foregoing tests, the upper limit of the systematic uncertainty evaluation for $b_{\phi\eta}$ and BR($\phi \to \eta e^+e^-$) is accepted as 0.02 GeV^{-2} and $0.008 \cdot 10^{-4}$.

8. Summary and outlook

In this work, based on experimental data measured by the KLOE collaboration, the $\phi \to \eta e^+ e^-$ decay has been investigated. The goal of this work is to extract the branching ratio for the $\phi \to \eta e^+ e^-$ decay, the slope of an electromagnetic transition form factor for $\phi - \eta$ mesons and a charge radius for the ϕ meson. The information about the quark's spatial distribution of mesons involved in the $\phi \to \eta\gamma^* \to \eta e^+ e^-$ process has been extracted by comparing the experimental mass spectrum of the lepton pair with results based on QED for pointlike particles. Extracted information gave possibility to test the theoretical predictions for this channel (like VDM, Ivashyn and Leupold-Terschlüsen models).

The measurement was performed using the KLOE detector and the electron-positron beams circulated in DAΦNE accelerator. The detector and accelarator are situated in the Italian National Center for Nuclear Physics in Frascati, near Rome. The DAΦNE collider is running at a center of mass energy of $\sqrt{s} \sim 1020$ MeV in order to produce the ϕ meson almost at rest. In the 2004-2005 years the KLOE detector registered about $5 \cdot 10^9$ ϕ mesons produced in e^+e^- collisions at DAΦNE accelerator. This data constitute the experimental base for this thesis. The KLOE detection setup consists of two main detectors: an electromagnetic calorimeter and a large drift chamber. The drift chamber and the calorimeter are inside a superconducting coil which produces about 0.52 T magnetic field parallel to the beam axis.

The four-momentum vector of the η meson was determined using the reconstructed four-momenta of ϕ meson, two gamma quanta, two charged pions, electron and positron. The four-momenta of two gamma quanta were reconstructed using time and energy measured by the electromagnetic calorimeter. The momenta of charged particles were reconstructed from the particles curvature in the Drift Chamber. In order to distinguish between pions and electrons, the time-of-flight (TOF) method was used.

After selection of the final sample, we reconstructed around 13′000 events coming from $\phi \to \eta\gamma^* \to \eta e^+ e^- \to \pi^0\pi^+\pi^- e^+ e^-$ decay with less than 2% background contamination. In presented work two methods of the background subtraction in the $M_{e^+e^-}$ spectrum were tested. In the first method the background was estimated based on simulations and the simulated spectra were subtracted from the experimental result. In the second method the background was estimated for each $M_{e^+e^-}$ bin separately based on the experimental distribution of the recoil mass of e^+e^- pair.

The estimation of the systematic uncertainty, for the slope parameter $b_{\phi\eta}$ and BR values, has been done by changing the initial condition of each selection criteria separately. The upper limit of systematic error σ_{syst}, was calculated as the square root of the quadratic sum of all contributions. Almost all performed checks give a non-significant deviation with respect to the statistical uncertainty. Therefore, for the final estimation of systematic uncertainty only this contribution were taken into account for which the deviations were statistically significant.

The value of $\Lambda_{\phi\eta}$ parameter extracted from the $M_{e^+e^-}$ distribution is equal to $\Lambda_{\phi\eta} = (0.872 \pm$

0.075) GeV, which corresponds to the value of form factor slope:

$$b_{\phi\eta} = (1.32 \pm 0.23 \pm 0.02)\ GeV^{-2}\ . \tag{8.1}$$

Within the statistical and systematic uncertainties, the value of form factor slope confirms the calculations of the Vector Meson Dominance model within one standard deviation and differs by more than two standard deviations from Ivashyn and Leupolds models predictions. It is important to stress that in literature we didn't find the values of uncertanties of estimations of the $b_{\phi\eta}$ parameter in Ivashyn and VMD models and also uncertainty for branching ratio value in VMD model.

The extracted values of BR($\phi \to \eta e^+ e^-$) and the radius of ϕ meson for analyzed reaction are:

$$\begin{aligned} &BR(\phi \to \eta e^+ e^-) = (1.170 \pm 0.035_{stat} \pm 0.008_{syst}) \cdot 10^{-4}\ , \\ &< r_\phi^2 >^{1/2} = 0.56 \pm 0.05\ fm\ . \end{aligned} \tag{8.2}$$

The value of BR extracted in our analysis is in agreement with the theoretical predictions and experimental measurements.

Summary of all extracted results in this analysis compared with previous experimental values and theoretical predictions is presented in Tab. 8.1 and Tab. 8.2.

	Theory			*Experiment*	
	VMD	Leupold	Ivashyn	SND	**Our analysis**
$b_{\phi\eta}$ (GeV^{-2})	1.0	2.74±0.87	1.94	3.8 ± 1.8	$\mathbf{1.32 \pm 0.23 \pm 0.02}$

Table 8.1: Form factor slope of the $\phi - \eta$ transition, determined in this work, compared to the theoretical predictions and SND results [3, 22].

	Theory		*Experiment*			
	VMD	Leupold	CMD-2	SND	PDG	**Our analysis**
BR(10^{-4})	1.1	1.13 ± 0.14	1.14±0.16	1.19 ± 0.31	1.15 ± 0.10	$\mathbf{1.170 \pm 0.035 \pm 0.008}$

Table 8.2: Branching ratio of the $\phi \to \eta e^+ e^-$ decay, determined in this work, compared to the theoretical predictions and experimental results [1, 3, 22, 28].

It is shown, that KLOE detector is a precise tool to investigate the $\phi - \eta$ transition form factor with negligible background contamination coming from other ϕ decays and machine background. The measured results for slope of transition form factor, branching ratio and the charge radius of ϕ meson are delivered with the biggest precision ever.

Additionaly, it is worth to mention that achieved results can still be improved because the investigations of this decay will be continued with the upgraded KLOE detector (KLOE-2). Modification of the collision region on DAΦNE accelerator, done in last years, improved the accelerator luminosity by a factor of three. During the next data taking period (2013-2015) we

plan to collect total integrated luminosity amounting to about 20 fb^{-1}, which is more than ten times higher statistic than was used in this analysis. In addition, the new data will be delivered with a higher quality due to the fact that KLOE performance have been improved by adding new detectors subsystems like Inner Tracker (Cylindircal GEM vertex detector) and several calorimeters. The new detectors will increase the KLOE acceptance and reduce the background. Details are presented in appendix B.

A. Φ and η mesons properties

Mesons are particles which are built of quark and antiquark. The first time the term *meson*[1] was used by Hideki Yukawa in order to describe the particle with the mass in the middle between masses of an electron and a proton. Nowadays, this particle is known as the π meson. Mesons are divided into groups depending on their quantum numbers.

In 1960 J. J. Sakurai [72–74] predicted the existence of vector mesons which are characterized by a spin equals to one and a negative parity ($J^P = 1^{-1}$). The first experimentally confirmed member of vector mesons group was the ρ meson in 1961 [75]. In the same year the discovery of the ω meson took place [76]. The next vector meson (ϕ) was discovered in the year 1962 [77]. This latter particle constitutes one of our main interests. It is built predominantly of strange quark and antiquark ($\phi = s\overline{s}$) in S state creating the spin triplet ($\uparrow\uparrow$) [78], with the mass of 1019.445±0.020 MeV [1].

Another kind of mesons family are pseudoscalars mesons, particles characterised by an orbital angular momentum value equals to zero, a negative parity and a positive charge conjugation. Quarks inside the psudoscalar meson are situated with anti-parallel spins ($\uparrow\downarrow$). They constitute the lightest nonet of the particles build with quarks and antiquarks. To this family belongs the η meson which is a second particle constituting our main interest. The η meson was discovered in 1961 at the Berkeley Bevatron [79].

The analysed decay $\phi \to \eta e^+ e^-$ is rather rare (see Tab. A.1). Also the decay $\eta \to \pi^0\pi^+\pi^-$ isn't the most frequent decay of the η meson (Tab. A.2).

The most frequent decays with the biggest branching ratio values for ϕ and η mesons are presented in Tab. A.1 and Tab. A.2, respectively. The investigated decay chain was marked with the bold font.

Decay Mode	*Branching Ratio(%)*
$\phi \to K^+K^-$	48.9 ± 0.5
$\phi \to K_L^0 K_S^0$	34.2 ± 0.4
$\phi \to \rho\pi$ / $\pi^+\pi^0\pi^-$	15.32 ± 0.32
$\phi \to \eta\gamma$	1.309 ± 0.0240
$\phi \to \pi^0\gamma$	$(1.27 \pm 0.06) \cdot 10^{-1}$
$\phi \to e^+e^-$	$(2.954 \pm 0.030) \cdot 10^{-2}$
$\phi \to \mu^+\mu^-$	$(2.87 \pm 0.19) \cdot 10^{-2}$
$\boldsymbol{\phi \to \eta e^+ e^-}$	$\boldsymbol{(1.15 \pm 0.10) \cdot 10^{-2}}$

Table A.1: Main decays of the ϕ meson [1].

[1]The word is coming from greek word *mesos* which means „in the middle", or „intermediate".

Decay Mode	*Branching Ratio(%)*
$\eta \to \gamma\gamma$	39.30 ± 0.20
$\eta \to 3\pi^0$	32.56 ± 0.23
$\boldsymbol{\eta \to \pi^+\pi^-\pi^0}$	$\mathbf{22.73 \pm 0.28}$
$\eta \to \pi^+\pi^-\gamma$	4.60 ± 0.16
$\eta \to e^+e^-\gamma$	0.70 ± 0.07

Table A.2: Main decays of the η meson [1].

B. Upgrade of the KLOE detector

Currently, the KLOE detector is being upgraded in a view of the new experimental program which will extend the studies to the more precise measurement of the K_S mesons and the production of mesons in the $\gamma\gamma$ fusion [39, 46, 50]. For this aim the vertex detector and the $\gamma\gamma$-tagger [80] are being built [81].

New QCAL (QCALT)

The upgrade of QCAL detector (Fig. 3.10) [53] was needed, because the interaction region was modified and in the present scheme the angle between colliding beams has been increased from 8 to 18 degrees, which practically excludes the possibility to use the existing QCAL calorimeter [81].

The upgraded detector, with improved position resolution, will allow to extend the search for $K_L \to 2\pi^0$ events also in case when three photons are reconstructed in the EMC and one photon in QCALT, thus strongly reducing the correction for acceptance [81] and the contamination from $K_L \to 3\pi^0$ when some photons hit the detector. Using upgraded detector will increase a detection efficiency and reduce the accidental losses, the KLOE-2 experiment will be provided with two new tile calorimeters around the quadrupoles of DAΦNE machine. Each calorimeter has dodecagonal structure (Fig. B.1 (top left)), 0.9 m length, is made of 5 layers of 3.5 mm thick lead and 5 mm thick BC408 scintillator tiles (Fig. B.1 (top right)), along the z axis each layer is segmented in 18 cells. The time resolution is about 750 ps and the spatial resolution along z axis is 1.5 cm.

CCALT

The electromagnetic calorimeter of KLOE covers up to $\geq 21^o$. To extend the coverage at lower angles (8^o), both as a veto detector ($K_S^0 \to \gamma\gamma$) or as acceptance extension for the rare decay channels ($K_S^0 \to 3\pi^0$), two small barrels of 24 crystals, with the length from 10 to 13 cm and transversal area 1.5 × 1.5 to 2 × 2 cm^2 will be installed between the IP and the QCALT, as shown in Fig. B.1 (bottom left). The energy resolution has been measured at beam test facility (BTF) in LNF and the fit to the data gives the following terms: $\frac{2.4\%}{\sqrt{E(GeV)}}$ (stochastic), $\frac{0.8\%}{E(GeV)}$ (electronic noise) and 5% (constant due to leakage, light production and collection non uniformity, calibration).

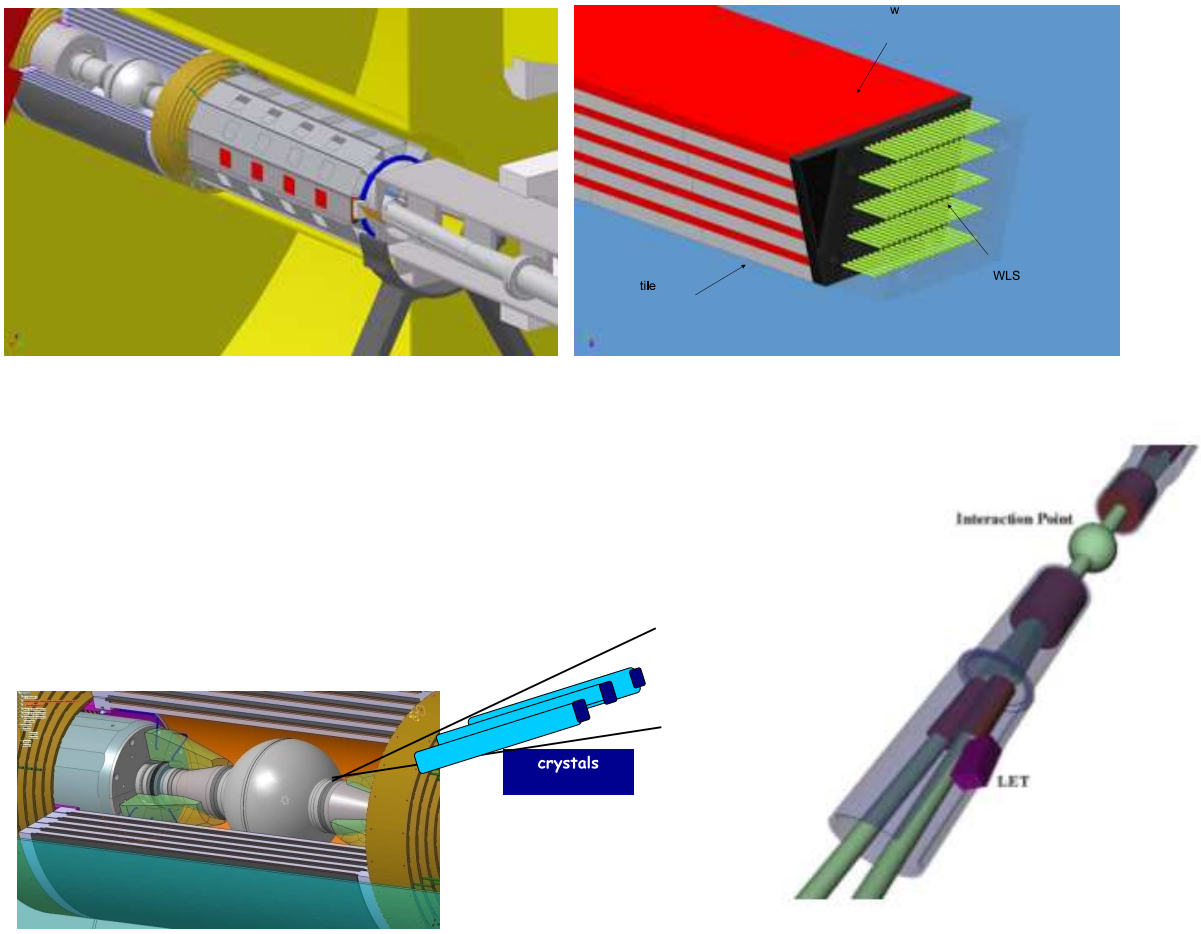

Figure B.1: Integration of the QCALT (top left), a cross-section of a one module, of the QCALT (top right), the integration of the CCALT (bottom left), integration of the LET (bottom right). The pictures are adapted from [35].

HET and LET

A part of the physics program of the KLOE-2 project is devoted to the $\gamma\gamma$ physics. As a matter of fact the photon-photon scattering gives an access to states with $J^{PC} = 0^{\pm+}, 2^{\pm+}$ and in particular the golden channel $\gamma\gamma \to \pi^0\pi^0$ in the low energy region suitable for the investigations of the $\sigma(600)$ meson. In order to reduce the huge background coming from the ϕ decays, a couple of tagging system is needed: low-energy tagger (LET) and high energy tagger (HET). The first (matrix of LYSO crystals) is placed 1 m far from the IP in the horizontal plane and will detect final leptons with energy between 50 and 450 MeV. The latter is placed inside the machine lattice, 11 m far from the IP, as close as possible to the beam line.

The HET tagger consists of 30 fast scintillators (type EJ228) which provide a spatial resolution of 2 mm corresponding to 500 keV/c momentum resolution. The HET detector is presented in Fig. B.2, the two parts of this detector were installed on opposite sides of the KLOE detector.

Figure B.2: The HET detector. The figure is adapted from [82].

The main task of HET detector ($\gamma\gamma$-tagger) is the detection of e^+ and e^- from $\gamma\gamma$ reactions emitted at small angle [83, 84] with the widest possible energy ranges. The $\gamma\gamma$ tagger provides information on the angle and the energy of the scattered electrons and positrons [85, 86] and hence it will permit to study the production of mesons in $\gamma\gamma$ fusion via the reaction:

$$e^+e^- \to e^+e^-\gamma^*\gamma^* \to e^+e^- + X, \tag{B.1}$$

where X is some arbitrary final state allowed by conservations laws. The diagram of this proces is presented in Fig. B.3.

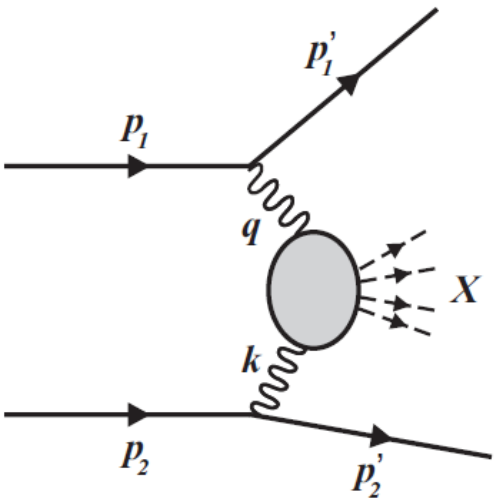

Figure B.3: Two-photon particle production in a e^+e^- collider.

The Vertex Detector: Inner Tracker

In the KLOE detector the first hit is measured by a drift chamber at a radius of 28 cm from the interaction point (IP) [39]. Therefore in order to improve the resolution of the determination of the K_S and K_L decay near the interaction point a new vertex detector is constructed [80]. This detector will consist of four concentric layers of cylindrical triple-GEM (C-GEM), completely realized with very thin polyimide foils [87–91]. The scheme of the vertex detector is presented in Fig. B.4.

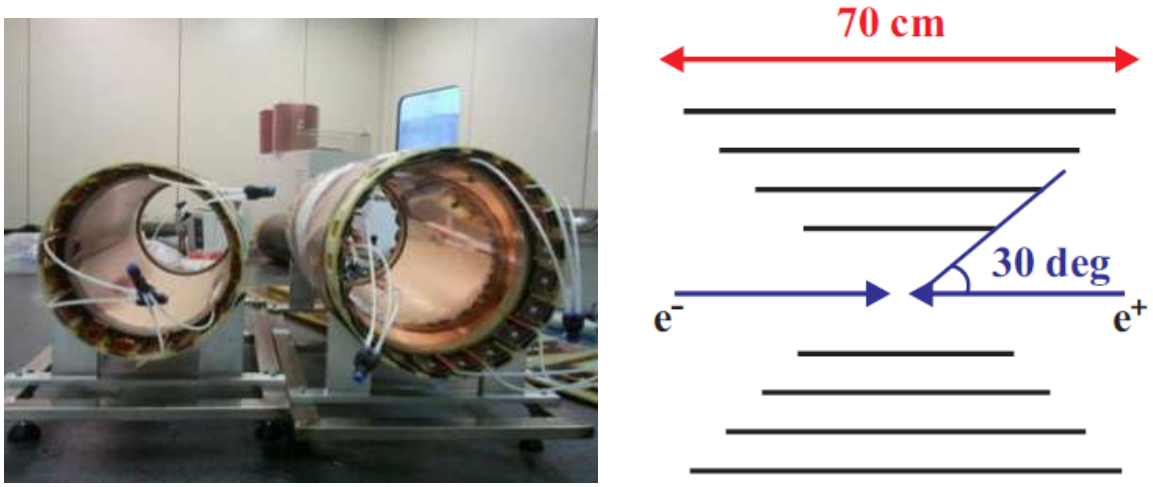

Figure B.4: Realistic view of already constructed two layers of vertex detector [82] (left). Schematic view of complete vertex detector (right).

The layers are made of light materials in order to minimize γ absorption [83]. The expected resolution in a $r\phi$ plane is $\sigma_{r\phi} \sim$ 200 μm and along the beam axis is $\sigma_Z \sim 400$ μm, this means an improvement of a factor of three for the resolution of the K_S decay point determination.

An inner tracker will be placed between the beam pipe and the DC inner wall. This detector will:

- reduce the track extrapolation length and improve the decay vertex reconstruction capability,
- increase the geometrical acceptance for low momentum tracks, presently limited by KLOE magnetic field and by the distance of the DC first layer and optimize their detection,
- improve the momentum resolution.

Education is what remains after one has forgotten everything he learned in school.

Edukacja jest tym co zostaje jak zapomni się wszystko czego nauczyło się w szkole.

Albert Einstein (1879 - 1955)

Acknowledgments

I would like to express my highest gratitude to people who support and help me during the Ph.D. studies, at my work time and in the private live. And without whom this dissertation would never be completed. This short note isn't enought to express everything with my poor english. However, I would like to express my appreciation especially to:

- Prof. dr hab. Paweł Moskal for organizing an additional place at COSY Summer School in the year 2006. Since this event my real adventure with physics has begun. I also would like to thank you Paweł for great patience, for all the time spent correcting this thesis, for many usefull suggestions and remarks when I discovered the another problem in analysis and also for hours of discussions and motivating me during the last six years,

- Dr Simona Giovannella for many hours of working together with data analysis, reconstruction algorithms and for being my KLOE supervisor. This was a great time working together,

- Dr Fabio Bossi, Dr Catherina Bloise and Dr Antonio Passeri for letting me work in Laboratori Nazionali di Frascati and for financial support of my stays in Frascati which gave me opportunity to work with the very modern detector,

- Dr Wojciech Krzemień for his great friendship during the last four years, for many discussions, coffees and help in my professional and private life. And for all positive things which happen in life during that time,

- Dr Marcin Zieliński for common work in the rooms 222 and 05A, for many hours of discussions, coffees, for his friendship and all the time spend together during the last six years,

- Dr Marek Jacewicz for his friendship and introduction to KLOE reconstruction algorithms, for time spend together in Uppsala and Frascati,

- Dr Roberto Versaci for introduction to the KLOE analysis, for help with many problems related with the fortran code and for lots of things not related with the work time,

- Prof. dr hab. Bogusław Kamys for letting me work in the Nuclear Physics Division of the Jagiellonian University,

- Prof. dr hab. Lucjan Jarczyk for his pertinent suggestions and remarks during meetings and seminars in Nuclear Physics Division of the Jagiellonian University,

- Prof. dr hab. Wojciech Wiślicki for many interesting discussions about physics issues and computer science,

- Kraków KLOE group: Dr Michał Silarski, Dr Eryk Czerwiński, Izabela Pytko, Krzysztof Kacprzak, Alek Gajos, Daria Kamińska for many working meetings and lot of discussions during them. Also for nice atmosphere during the work,
- Dr Anna Sochocka for helping me with organization my Ph.D. duties and working time,
- Dr Gianfranco Morello for lots of discussions related with the KLOE detection setup and for support in Frascati,
- my KLOE-2 colleagues: Dr Erika De Lucia, Dr Antonio De Santis, Dr Salvatore Fiore and Ivano Sarra for lots of remarks and not only scientific discussions,
- all my colleagues from Jagiellonian University: Dr Małgorzata Hodana, Dr Joanna Klaja, Dr Paweł Klaja, Magdalena Skurzok, Tomasz Bednarski, Tomasz Twaróg, Szymon Niedźwiecki and Andrzej Pyszniak for a nice atmosphere during the work,
- authors of physics theories which describing the decay investigated in this dissertation, Dr Sergiy Ivashyn, Carla Terschlüsen and Prof. Stefan Leupold, for lots of disscussions about physics and for correcting some parts of this thesis,
- Jan Kowalski, Seweryn Ożóg and Michał Cichocki for their help, patience and support.

Chciałbym również podziękować moim rodzicom za wszystko to czego mnie nauczyli w życiu i za ciągłe wsparcie, którego mi udzielają przez te wszystkie lata, mojemu bratu, który był zawsze kiedy go potrzebowałem. Na koniec chciałem podziękować mojej drugiej połowie, której wiara we mnie zawsze dodawała mi sił.

And at the end I would like to thank all the people without whom this thesis would never be accomplished, and with whom I could work with pleasure in Kraków, Frascati, Uppsala and Jülich.

Bibliography

[1] Particle Data Group (2012) J. Beringer et al. (Particle Data Group), Phys. Rev., **D 86**, 010001 (2012)

[2] L. G. Landsberg, *Electromagnetic Decays of Light Mesons*, Phys. Rept. **128**, 301, (1985)

[3] M.N. Achasov et al., Phys. Lett., **B 504**, 275, (2001)

[4] A. Faessler, C. Fuchs, M.I. Krivoruchenko, Phys. Rev., **C 61**, 035206, (2000)

[5] M. Soyeur, *Dilepton production: A tool to study vector mesons in free space in nuclei and in nucleus nucleus collisions*, Acta Phys. Polon., **B 27**, 401, (1996)

[6] J. F. McGowan, e-Print: arxiv 9501399, (1995)

[7] V. M. Budnev and V. A. Karnakov, *Eta meson decay into gamma mu+ mu- in the Vector Dominance Model*, Pisma Zh. Eksp. Teor. Fiz., **29**, 439 (1979)

[8] A. Bramon and E. Masso, Q^2 *duality for electromagnetic form factors of mesons*, Phys. Lett., **B 104**, 311, (1981)

[9] L. P. Kaptari and B. Kampfer, η *and* η' *production in nucleon-nucleon collisions near thresholds*, Acta Phys. Polon. Supp., **2**, 149, (2009)

[10] C. Terschlüsen, S. Leupold, Phys. Lett., **B 691**, 191, (2010)

[11] Problems of Atomic Science and Technology N 1., Series: Nuclear Physics Investigations (57) 179-182 (2012)

[12] C. Boehm, P. Fayet, Nucl. Phys., **B 683**, 219, (2004)

[13] F. Archilli et. al, Phys. Lett., **B 706**, 251, (2012)

[14] D. Babusci et. al, e-Print: arxiv 1210.3927, (2012)

[15] Y. Nambu, *Possible Existence of a Heavy Neutral Meson*, Phys. Rev., **106**, 1366, (1957)

[16] H. B. O'Connel, B. C. Pearce, A. W. Thomas and A. G. Williams, Progress in Particle and Nuclear Physics, **39**, 201, (1997)

[17] R. Arnaldi et al, Phys. Lett., **B 677**, 260, (2009)
R. Arnaldi et al, e-Print: arxiv 0902.2547, (2009)

[18] R. I. Djeliadin et al., Phys. Lett. **B 102**, 296, (1981)

[19] M.F.M. Lutz and S. Leupold, Nucl. Phys., **A 813**, 96, (2008)

[20] S. Leupold and M.F.M. Lutz, Eur. Phys., **A 39**, 205, (2009)

[21] C. Terschlüsen, *Electromagnetic Transition Form Factors of Pseudoscalar and Vector Mesons*, Diploma Thesis, (2010)

[22] C. Terschlüsen, S. Leupold, e-Print: arxiv 1111.4907, (2011)

[23] C. Terschlüsen, S. Leupold and M.F.M Lutz e-Print: arxiv 1204.4125, (2012)

[24] C. Terschlüsen, S. Leupold, private communication, (2012)

[25] C. Terschlüsen and S. Leupold, Phys. Lett., **B 691**, 191, (2010)

[26] S. Ivashyn, e-Print: arxiv 1111.1291, (2011)

[27] S. Ivashyn, private communication, (2012)

[28] R.R. Akhmetshin et al., Phys. Lett., **B 501**, 191, (2001)

[29] P. Ciambore, A. Passeri, *The KLOE calorimeter front end electronics*, Frascati Physics Series, **Vol. XXI**, 161, (2000)

[30] M. Palutan, *The KLOE calorimeter trigger*, Frascati Physics Series, **Vol. XXI**, 169, (2000)

[31] J. Lee-Franzini and P. Franzini, e-Print: hep-ex/0702016v2, (2007)

[32] B. Di Micco, Ph. D. Thesis, Roma Tre University, (2004)

[33] M. Zobov et al., Phys. Part. Nucl. Lett., **5**, 560, (2008)

[34] M. Zobov, e-Print: arxiv:0709.3696, (2007)

[35] G. Morello, UNIVERSITA' DELLA CALABRIA, PhD thesis (2010)

[36] V. Lucherini et al., Nucl. Instr. & Meth. in Phys. Res., **A 496**, 315, (2003)

[37] M. Agnello et al., Nucl. Instr. & Meth. in Phys. Res., **A 570**, 205, (2007)

[38] D. Alesini et al., LNF-06/33 (IR), (2006)

[39] R. Beck et al., KLOE-2 Letter of Intent, (2006), http://www.lnf.infn.it/lnfadmin/direzione/roadmap/LoIKLOE.pdf

[40] M. Zobov et al., e-Print: arXiv1106.5329, (2012)

[41] D. Shatilov and M. Zobov, ICFA BDN 37, 99, (2005)

[42] D. Pestrikov, Nucl.Instrum.Meth., **A 336**, 427, (1993)

[43] M. Adinolfi et al., Nucl. Instr. & Meth. in Phys. Res., **A 482**, 364, (2002)

[44] M. Adinolfi et al., Nucl. Instr. & Meth., **A 488**, 51, (2002)

[45] F. Ambrosino et al., e-Print: physics/0404100v1, (2004)

[46] G. Amelino-Camelia et al., Eur. Phys. J, **C 68**, 619, (2010)

[47] I. Balwierz, Jagiellonian University, Diploma Thesis, (2011)

[48] S. Dell'Agnello, *The KLOE detector*, Frascati Physics Series, **Vol. XVI**, 381, (1999)

[49] KLOE experiment homepage, http://www.lnf.infn.it/kloe/

[50] F. Bossi, E. De Lucia, J. Lee-Franzini, S. Miscetti and M. Palutan, Riv. Nuovo Cim., **31**, 531, (2008)

[51] M. Adinolfi et al., Nucl. Instr. & Meth. in Phys. Res., **A 494**, 326, (2002)

[52] M. Antonelli, G. Barbiellini, S. Bertolucci, C. Bini, C. Bloise, R. Caloi, P. Campana and F. Cervelli et al., Nucl. Instrum. Meth., **A** 379, 511, (1996)

[53] M. Adinolfi et al., Nucl. Instr. & Meth. in Phys. Res., **A 483**, 649, (2002)

[54] A. De Santis, Laboratori Nazionali di Frascati, Phd thesis, (2008)

[55] M. Adinolfi et al., *The KLOE electromagnetic calorimeter* Nucl. Instrum. Meth., **A 482**, 364, (2002)

[56] W. Kim, *The Clustering Algorithm for the KLOE Calorimeter*, Laboratori Nazionali di Frascati, I-00044 Frascati, Italy, (1995)

[57] F. Nguyen, Dipartamento di Fisica, Universita Roma Tre and Sezione INFN, Italy, Phd thesis, (2004)

[58] G. Pirozzi, M. Incagli et al., *The Event Classification procedures*, Kloe Memo 225, (2000)

[59] S. Giovannella, *ETA3PITAG: event classification routine for* $\phi \to \eta l^+ l^-$ *with* $\eta \to \pi^0\pi^+\pi^-$ *events*, Kloe Memo K2ID-5, (2012)

[60] http://wwwasdoc.web.cern.ch/wwwasdoc/geantold/H2GEANTBASE001.html

[61] http://wasm.web.cern.ch/wasm/

[62] A. De Santis, R. Versaci, Kloe Memo 356, (2009)

[63] E. Barberio, B. van Eijk and Z. Was, Comput. Phys. Commun., **66**, 115, (1991)

[64] M. Adinolfi et al., e-Print: hep-ex/0006039, (2000)

[65] S. Giovannella, R. Versaci, Kloe Memo 350, (2008)

[66] http://www-meg.phys.cmu.edu/williams/ruby-minuit/minuit.pdf

[67] Ivano Sarra, Rome Tor Vergata University, Phd thesis, (2012)

[68] A. Faessler, C. Fuchs, M.I. Krivoruchenko, Phys. Rev., **C 61**, 035206, (2000)

[69] T. T. Chou, C. N. Yang, Phys. Rev., **170**, 1591, (1968)

[70] N. Isgur, Acta Physica Polonica, **B 8**, 12, (1977)

[71] R. Barlow, *Systematic errors: Facts and fictions*, hep-ex/arxiv:0207026, (2002)

[72] J. J. Sakurai, Ann. Phys., **11**, (1960)

[73] J. J. Sakurai, Phys. Rev. Lett., **22**, 981, (1969)

[74] J. J. Sakurai, *University of Chicago Press*, ISBN-10: 0226733831, Chicago, (1969)

[75] A. R. Erwin, R. March, W. D. Walker and E. West, Phys. Rev. Lett., **6**, 628, (1961)

[76] B. C. Maglic et al., Phys. Rev. Lett., **7**, 178, (1961)

[77] L. Bartenza et al., Phys. Rev. Lett., **9**, 180, (1962)

[78] D.H. Perkins, *Wstęp do Fizyki Wysokich Energii*, PWN, Warszawa, (1989)

[79] A. Pevsner and others, *Evidence for a three pion resonance near 550 MeV*, Phys. Rev. Lett., **7**, 421, (1961)

[80] D. Domenici et al., Frascati Physics Series, **XLVI**, (2008)

[81] R. Beck et al., A proposal for the roll-in of the KLOE-2 detector, INFN Frascati, (2007), http://www.lnf.infn.it/kloe/kloe2/roll/rollin_proposal.pdf

[82] http://www.lnf.infn.it/kloe2

[83] G. Venanozi, *The Physics case of DAFNE-2*, XXXI International Conference of Theoretical Physics „Matter To The Deepest", Ustron, Poland, (2007)

[84] E. Ambrosino et al., e-Print: hep-ex/0603056v2, (2007)

[85] A.D'Angelo, *Progress Report on the $\gamma\gamma$ tagger*, Laboratori Nazionali di Frascati - INFN, Frascati, Italy, (2007)

[86] F. Ambrosino et. al., e-Print: hep-ex/0603056v2, (2007)

[87] G. Bencivenni, D. Domenici *An ultra-light cylindrical GEM detector as inner tracker at KLOE-2*, Laboratori Nazionali di Frascati - INFN, Frascati, Italy, (2007)

[88] G. Bencivenni, D. Domenici, Nucl. Instr. & Meth., **A 581**, 221, (2007)

[89] G. Bencivenni et al., Nucl. Instr. & Meth., **A 572**, 168, (2007)

[90] G. Bencivenni et al., *The Full Scal Prototype of the Cylindrical-GEM Detector as Inner Tracker in KLOE2*, Laboratori Nazionali di Frascati - INFN Via Enrico Fermi 40, I-00044 Frascati, Italy, (2008)

[91] D. Domenici, *The upgrade of the KLOE detector: KLOE2*, Frascati Physics Series, **XLVI**, (2007)

List of acronyms

ADC - Analog to Digital Converter
BP - Beam Pipe
BR - Branching Ratio
BTF - Beam Test Facility
ChPT - Chiral Perturbation Theory
CM - Central Mass System
CMD - Cryogenic Magnetic Detector
CPU - Central Processing Unit
DAQ - Data Acquisition
DC - Drift Chamber
DCW - Drift Chamber Wall
$\boldsymbol{D_{e^+e^-}}$ - Distance between e^+e^- on the conversion surface
EMC - Electromagnetic Calorimeter
ECL - Event Classification Algorithms
FIBM - Cluster of IBM computers
FEE - Front End Electronics
FF - Form Factor
FILFO - FILtro di FOndo, background filter in italian language
FSR - Final State Radiation
GEM - Gas Electron Multiplier
HET - High Energy Tagger
IP - Interaction Point
ISR - Initial State Radiation
$\boldsymbol{M_{e^+e^-}}$ - Invariant Mass of e^+e^- pair
LET - Low Energy Tagger
LNF - Laboratori Nazionali di Frascati
MC - Monte Carlo
MIP - Minimum Ionizing Particle
SND - Spherical Neutral Detector
TDC - Time to Digital Converter
TOF - Time of Flight
UFO - UnidentiFied Objects
VMD - Vector Meson Dominance

„The Little Prince”
Antoine de Saint-Exupéry (1900 - 1944)